Corrections to and Applications of the Antineutrino Spectrum Generated by Nuclear Reactors

Patrick John Jaffke

Dissertation submitted to the Faculty of the
Virginia Polytechnic Institute and State University
in partial fulfillment of the requirements for the degree of

Doctor of Philosophy
in
Physics

Patrick Huber, Chair
Jonathan M Link
Leo E Piilonen
Eric R Sharpe

November 16, 2015
Blacksburg, Virginia

Keywords: Neutrino Physics, Reactor Physics, Spent Nuclear Fuel Correction, Non-linear Correction, Antineutrino Safeguards, Nuclear Non-proliferation

Corrections to and Applications of the Antineutrino Spectrum Generated by Nuclear Reactors

Patrick John Jaffke

(ABSTRACT)

In this work, the antineutrino spectrum as specifically generated by nuclear reactors is studied. The topics covered include corrections and higher-order effects in reactor antineutrino experiments, one of which is covered in Ref. [1] and another contributes to Ref. [2]. In addition, a practical application, antineutrino safeguards for nuclear reactors, as summarized in Ref. [3, 4] and Ref. [5], is explored to determine its viability and limits. The work will focus heavily on theory, simulation, and statistical analyses to explain the corrections, their origins, and their sizes, as well as the applications of the antineutrino signal from nuclear reactors.

Chapter 1 serves as an introduction to neutrinos. Their origin is briefly covered, along with neutrino properties and some experimental highlights. The next chapter, Chapter 2, will specifically cover antineutrinos as generated in nuclear reactors. In this chapter, the production and detection methods of reactor neutrinos are introduced as well as a discussion of the theories behind determining the antineutrino spectrum. The mathematical formulation of neutrino oscillation will also be introduced and explained.

The first half of this work focuses on two corrections to the reactor antineutrino spectrum. These corrections are generated from two specific sources and are thus named the spent nuclear fuel contribution and the non-linear correction for their respective sources. Chapter 3 contains a discussion of the spent fuel contribution. This correction arises from spent nuclear fuel near the reactor site and involves a detailed application of spent fuel to current reactor antineutrino experiments. Chapter 4 will focus on the non-linear correction, which is caused by neutron-captures within the nuclear reactor environment. Its quantification and impact on future antineutrino experiments are discussed.

The research projects presented in the second half, Chapter 5, focus on neutrino applications, specifically reactor monitoring. Chapter 5 is a comprehensive examination of the use of antineutrinos as a reactor safeguards mechanism. This chapter will include the theory behind safeguards, the statistical derivation of power and plutonium measurements, the details of reactor simulations, and the future outlook for non-proliferation through antineutrino monitoring.

Dedication

Dedicated to my uncle, who always supported
the education of my brothers and me:

Thomas A. Jaffke
November 12, 1946 - August 11, 2012

"You're an outfit."

Acknowledgments

I would first like to thank my advisor, Patrick Huber, who has always been ready and willing to teach and inspire despite his busy schedule. His insight and dedication to research has inspired me both as a scientist and an individual. It has been my great pleasure to learn all that I have from Dr. Huber.

Next, I thank my committee members, Professors Jon Link, Leo Piilonen, and Eric Sharpe, for their added guidance and discussions in reference to both my courses and my research.

A very special thanks must be issued to the administrative and support staff of the physics department. I was fortunate enough to work in an environment with incredibly supportive and generous people, especially Chris Thomas, the former graduate program coordinator, and Betty Wilkins, the current coordinator. In addition, my travel and conference attendance was made infinitely easier with help from Erin Rust and Sharon Proffitt. I must also extend a huge thank you to Roger Link and Travis Heath for their computational assistance, from familiarizing me with Linux to providing me with the knowledge to conduct research via the cluster. In addition, the cleanliness of my office is solely due to diligent work of Sue Connor.

Now, I would like to thank the large number of students (both graduate and undergraduate) I have met while at Virginia Tech these many years. These students have become my treasured friends, colleagues, and support system. There have been many, but I will name a few: Nick Gray, Ben Intoy, Carter Chamberlain, Mike Meeker, Zhuo Chen, Dan Osborne, Shadi Esmaeili, Hadi Parsian, Curtis Ogle, Ali Charkhesht, Phil Hochendoner, Hiba Assi, Eric Christensen, Chen Sun, He Feng, Rachel Elliot, Madhimura Nath, Ahmadreza Azizi, Mi Yan, Matthew Raum, Harshwardhan Chaturvedi, Parviz Seifpanahi, Zach Yokely, Tristan Wright, and many many others.

One person that has shown tremendous patience and support for me through the stressful days and nights of writing and research is Emily. To say I am grateful for your calming presence is a gross understatement of my love and appreciation.

Finally, I cannot thank my wonderful parents, Fred and Kathy, and my encouraging brothers, Andrew and Matthew, enough for their loving support, unending wisdom, and constant motivation for me throughout my graduate career, and, more importantly, my life. I am not the person I am today without the love of my family.

Contents

Chapter 1

Neutrino Introduction

This chapter provides a summary of the history of the neutrino. It covers the motivation for the inception of the neutrino by Pauli, as well as the early uses of neutrinos and, specifically, beta-decay to determine important aspects of the weak interaction and the Standard Model as a quantum field theory. Experiments behind neutrino oscillation are introduced, from Ray Davis and John Bahcall's Homestake experiment to SNO and SuperK. A brief description of the fascinating supernova surprise and the current status of neutrino oscillation is also addressed. Finally, the unanswered questions in neutrino physics as well as the appearance of three anomalies are discussed.

1.1 The Neutrino

The historical introduction of the neutrino is centered around the radioactive decay process of beta-decay. Early measurements of beta-decay, then considered a two-particle decay process, indicated that the beta particle had a continuous energy spectrum, contrary to energy conservation in two-body decays. Furthermore, angular momentum was not conserved with the two-particle decay process as another half unit of spin was missing. Wolfgang Pauli was the first to postulate the third particle in beta-decay, now named the neutrino, in his famous letter [6] resulting in the following decay process:

$$\mathrm{n} \rightarrow \mathrm{p} + e^{-} + \bar{\nu}_e \tag{1.1}$$

This new particle was then incorporated into Fermi's theory of beta-decay [7]. The neutrino would need to be a spin-1/2 particle, with zero net electric charge, and an extremely small mass based on the shape of the beta spectrum first measured by Chadwick [8]. In addition, the interaction cross-section of the neutrino with ordinary matter would need to be incredibly small to explain the lack of detection of such a particle. The ν cross-section on various nuclei was first estimated by Bethe and Peierls as being $< 10^{-44}\,\mathrm{cm}^2$ [9], prompting Bethe and

Peierls to declare that there is "no practically possible way of observing neutrinos." This tiny cross-section was also calculated later by Bahcall [10,11] as being between $\mathcal{O}(10^{-46})$ and $\mathcal{O}(10^{-42})\,\mathrm{cm}^2$, cementing the neutrino as an extraordinarily non-interacting particle.

Over twenty-five years later, the detection of the free neutrino was first reported by Cowan and Reines [12] utilizing electron antineutrinos from a nuclear reactor, thus becoming the first reactor antineutrino experiment. Neutrinos would become instrumental in determining the properties of the weak interaction and its eventual violation of parity (P). Lee and Yang [13] theorized parity-violation, first inspired by the so-called $\theta - \tau$ puzzle from K meson decays. The next year would provide experimental evidence of maximal parity violation in beta-decays via the experiment of Wu [14]. Parity violation, and the assumed charge conjugate (C) violation, meant that the weak interaction needed to be restructured into a vector minus axial (V-A) theory [15–17] in order to couple with left-handed particles and right-handed antiparticles. This preference, and the measurements of neutrino helicity, observed to be 100% left-handed by Goldhaber [18], solidified the absence of right-handed neutrinos and left-handed antineutrinos. Eventually, these observations would motivate experimental searches for the Majorana-Dirac nature of neutrinos [19, 20], a notably older theoretical concept [21].

As the Standard Model began taking its roots as a theory mediated by gauge symmetries, Quantum Electrodynamics (QED) from a U(1) group; widely attributed to Weyl [22], the weak interaction via a SU(2) group [23], and Quantum Chromodynamics (QCD) with a SU(3) group [24], neutrinos were found to fit nicely into the framework. Furthermore, QED and the weak interaction would be unified by Glashow [25], Weinberg [26], and Salam [27] solidified by evidence of the neutral current interactions from neutrino scattering in the bubble chamber experiment Gargamelle [28]. Neutrinos were represented in the Standard Model as massless particles in accordance with the lack of any evidence of a nonzero neutrino mass from experiment, especially the beta-endpoints observed by Chadwick [8]. However, neutrinos would soon provide overwhelming evidence that the Standard Model would need to be modified in order to remain accurate.

1.2 Oscillation

As early as 1960, neutrino oscillation, the change in neutrino flavor during flight, was postulated through the insight that electron neutrinos ν_e and muon neutrinos ν_μ may be different particles and, thus, produced in different processes [29]. It should be noted that oscillations between neutrinos and antineutrinos [30] predated the exploration of flavor oscillations. Confirmation that ν_e and ν_μ were different particles was observed later in the pion decays $\pi^\pm \to \mu^\pm + (\nu/\bar{\nu})$ [31]. Neutrino oscillation, in its two-flavor framework, was first properly introduced by Maki, Nakagawa, and Sakata [32]. Experimental evidence for oscillation would begin to slowly accumulate, beginning with the solar neutrino experiment, by Davis [10] and Bahcall, which was proposed to test the fusion model for the Sun in the late 1960s. The

results in the 1970s would be the first indicator of neutrino oscillation in the form of the solar neutrino problem, represented as a deficit of detected neutrinos in Davis' experiment as compared to the calculations by Bahcall. This extremely large discrepancy, manifesting as an observed to expected ratio of $1:3$, stood for more than 30 years.

In the 1980s the unexpected observation of a nearby supernova would provide a new sector to test neutrino physics. Currently, there are over 500 papers[1] analyzing the neutrinos observed from a type II supernova, SN 1987A. Three experiments, originally designed for the detection of nucleon decay, would detect neutrinos from SN 1987A [33–35]. Subsequent analyses of these mere 24 events would prove to yield quite extensive bounds on neutrino physics and beyond, covered nicely in Ref. [36]. Furthermore, one of the experiments, Kamiokande, would be transformed into a neutrino observatory where it would show the first evidence of neutrino oscillations [37]. SuperKamiokande (or SuperK), as it was named, was designed to observe neutrinos produced in the subsequent decays of pions and muons as generated in the atmosphere through cosmic ray collisions with nucleons. SuperK observed a nearly 6σ deficit of high energy 'upward-travelling' ν_μ neutrinos [37], providing the first concrete evidence for neutrino oscillations, a feat awarding it a share of the 2015 Nobel prize. This result would propel neutrino physics into the realm of beyond the Standard Model physics, as oscillation required nonzero neutrino masses.

Nonzero neutrino masses prompted a necessary change in the current Standard Model of particle physics, which describes neutrinos as massless Weyl fermions, with no right-handed neutrino component. Over the next two decades evidence for neutrino oscillation would pour in from several experiments. The solar neutrino problem, first uncovered by the Homestake experiment, would finally be solved by the Sudbury Neutrino Observatory (SNO) experiment [38]. SNO used data from neutral current interactions, sensitive to all three neutrino flavors. This use of neutral current events provided direct evidence for flavor transformation of solar neutrinos. For this, SNO was awarded the second half of the 2015 Nobel prize. Quickly following the SNO results was the first evidence of oscillation from antineutrinos as produced by nuclear reactors by the Kamioka Liquid-scintillator Anti-Neutrino Detector (KamLAND) experiment. KamLAND used a long baseline to observe a deficit of electron antineutrinos at the 99.95% confidence level [39] and confirmed the large mixing angle (LMA) solution to neutrino oscillation.

A long-baseline accelerator driven neutrino experiment, KEK to Kamiokande (K2K) [40], would also add its preference for $\nu_\mu \to \nu_\tau$ oscillations over the Standard Model picture of massless neutrinos. Data would soon be available from the Main Injector Neutrino Oscillation Search (MINOS) [41] experiment, utilizing a long-baseline accelerator design, and it was also found to support the finds of K2K. Together, this data, along with the SuperK and KamLAND results, would further solidify the neutrino oscillation framework with one large mass splitting of $\mathcal{O}(10^{-3})\,\mathrm{eV}^2$ between the neutrino mass eigenstates and one small splitting of $\mathcal{O}(10^{-5})\,\mathrm{eV}^2$.

[1] According to hep-Inspire as of Oct. 31, 2015

Around the same time, experimental results from various solar neutrino experiments, including the Soviet-American Gallium Experiment (SAGE) [42] and the Gallium Experiment (GALLEX) [43], would further solidify neutrino oscillation as well as provide a test for the so-called Standard Solar Model (SSM). These experiments utilized neutrinos from the pp solar cycle, which required a decrease in the neutrino interaction threshold for a robust study of the total thermonuclear fuel cycle. The SAGE and GALLEX results were also impactful as they provided evidence for oscillations within the Sun differing from those in vacuum. This matter effect, and the so-called MSW resonance, after its developers Mikheyev, Smirnov [44], and Wolfenstein [45], would proceed to influence supernova collapse models [36].

As of the early 2000s it appeared that three-neutrino oscillation could explain the neutrino disappearance in accelerator, atmospheric, solar, and reactor experiments. Two of the mass splittings, defined as $\Delta m^2_{ij} = m^2_j - m^2_i$, and mixing angles θ_{ij} were well explored, but only upper bounds were available on the third mixing angle θ_{13}. The accelerator-based experiment, Tokai to Kamioka (T2K), would be the first to provide strong evidence of non-zero values for θ_{13} [46] pioneering the idea of off-axis neutrino beams to select neutrinos in a certain energy window. Precision measurements would be rapidly released in the next few years. A small, but definitely non-zero value of θ_{13}, would be accurately measured with the Daya Bay reactor experiment [2], which utilized six reactors and 3 different baselines. Previous reactor experiments like Chooz had been able to provide θ_{13} limits [47]. Later, RENO [48] (Reactor Experiment for Neutrino Oscillation), and the upgraded Double Chooz [49] would echo the findings of Daya Bay. Precision measurements from the Borexino experiment would identify the rarer ^{7}Be-produced neutrinos [50] as well as add its constraint to the overall solar mixing parameters Δm^2_{12} and θ_{12}. With these results, neutrino physics would begin to enter the age of precision measurements. The mixing angle θ_{12} and the small splitting Δm^2_{12} are currently best constrained by a combination of KamLAND, solar, short-baseline, and accelerator experiments [51]. The mixing angle θ_{23} and the large splitting Δm^2_{23} are now best constrained by the accelerator experiment T2K [52]. Finally, the mixing angle θ_{13} is best constrained by the reactor oscillation experiment Daya Bay [53].

Currently, the neutrino oscillation parameters are established as the values in Tab. 1.1 according to the 2014 edition of the Particle Data Group (PDG) review [54], where the

	$\sin^2(2\theta_{12})$	$\sin^2(2\theta_{23})$	$\sin^2(2\theta_{13})$ $[\times 10^{-2}]$	Δm^2_{12} $[\times 10^{-5}\,\mathrm{eV}^2]$	$\lvert\Delta m^2_{23}\rvert$ $[\times 10^{-3}\,\mathrm{eV}^2]$
NH	$0.846^{+0.021}_{-0.021}$	$0.999^{+0.001}_{-0.018}$	9.3 ± 0.8	7.53 ± 0.18	2.44 ± 0.07
IH	$0.846^{+0.021}_{-0.021}$	$1.000^{+0.000}_{-0.017}$	9.3 ± 0.8	7.53 ± 0.18	2.52 ± 0.07

Table 1.1: Best fit neutrino oscillation parameters according to the PDG review from 2014 [54] for both normal hierarchy (NH) and inverted hierarchy (IH) with their 1σ errors.

Dirac CP-violating phase δ_{CP} has been excluded as its determination is not well-constrained now. For an excellent review of the agreement and tensions between neutrino experiments

and the determination methods for these best fits and tensions, Ref. [55] is highly recommended. In addition to determining the oscillation parameters, the quest to answer questions concerning astrophysical properties have motivated additional neutrino experiments, such as the IceCube observatory [56, 57]. Experiments have also been planned to answer the hierarchy question, such as the NuMI Off-axis ν_e Appearance (NOνA) search [58] and the Jiangmen Underground Neutrino Observatory (JUNO) [59]. A long-baseline neutrino experiment from Fermilab to the Homestake mine, the Deep Underground Neutrino Experiment (DUNE) [60] is also planned to determine the hierarchy, CP-violation, and answer other outstanding neutrino questions. Determination of the CP-violation phase δ has also been proposed via several baseline experimentsm such as the Decay-At-rest Experiment for δ_{CP} studies At the Laboratory for Underground Studies (DAEδALUS) [61], or by comparing $\nu_\mu \to \nu_e$ data with $\bar{\nu}_\mu \to \bar{\nu}_e$ [62].

Investigations on whether the neutrino is Majorana or Dirac in nature with neutrino-less double beta-decay ($0\nu\beta\beta$) is another avenue of past and future research. These experiments utilize the extremely rare double beta-decay channels of specific nuclei and attempt to observe the sharp endpoint peak signaling a $0\nu\beta\beta$ transition. The past and future experiments have studied numerous nuclides, such as ^{76}Ge, ^{100}Mo, ^{128,130}Te, and ^{136}Xe to name the most common choices. An excellent review on the theory and experimental requirements was conducted in Ref. [63]. The impact of a positive $0\nu\beta\beta$ observation has been explored in Ref. [64].

Attempts at measuring the absolute mass scale of the neutrino have also seen a recent resurgence. The original concept of observing the beta-decay endpoint with high precision by Fermi [7] is typically conducted on the beta-decay of tritium. This decay mode is commonly used as it is super-allowed meaning the nuclear transition matrix is easily determined, the energy endpoint is low allowing for good energy resolution, and the halflife is relatively long at $\sim 12.3\,\mathrm{y}$. The theoretical derivation of the neutrino mass and experimental difficulties of tritium beta-decay, along with other mass limits from cosmology and SN1987A are provided in Ref. [65]

There has also been a recent surge in applied neutrino experiments and projects. One such avenue is the use of antineutrinos as a monitor for nuclear reactors, first indicated in the late 1970s by Mikaelyan [66]. This concept will be covered thoroughly as both the theoretical limits [3, 5] and experimental efforts, past [67–70] and future [71–73], are introduced in the research sections of this thesis. Another avenue is the analysis of geoneutrinos, neutrinos produced in the decay chains of a select few long-lived isotope chains, including the natural thorium and uranium in the Earth, which can probe properties of the mantle and crust models [74]. These examples only represent a few of the concepts for neutrino applications, which can range from the supernova early warning system (SNEWS) [75] to a communication mechanism with submarines [76].

1.3 Anomalies

In addition to some more 'common' questions (labeled common as they do not necessarily refute extended Standard Model predictions) in neutrino physics, such as the Dirac-Majorana nature, mass hierarchy, and CP violation, recent experiments have uncovered several anomalies that remain unanswered. For example, the Liquid Scintillator Neutrino Detector (LSND) [77] and Booster Neutrino Experiment (BooNE) prototype MiniBooNE [78] experiments reported hints of excess in the $\bar{\nu}_\mu \to \bar{\nu}_e$ oscillation channel. A possible solution to this excess, the so-called LSND anomaly, is a new short-baseline oscillation, which corresponds to a new neutrino mass splitting of $\mathcal{O}(1\,\mathrm{eV}^2)$. This new light neutrino would have to be non-interacting with the weak interaction as the width of the Z^0 boson is limited by Ref. [79] and, thus, is dubbed a sterile neutrino. In addition, adjustments to the neutron lifetime [80], along with a re-analysis of the reactor antineutrino flux [81, 82] and the incorporation of non-equilibrium nuclides [83] amounted to an upward shift of the expected antineutrino rate by about $\sim 3\%$ on top of the already-observed 2.4% shortage at reactor experiments. This observed deficit of $\sim 5\%$ in all reactor experiments, the so-called reactor anomaly, has also been explored as a result of short oscillations from a sterile neutrino in agreement with the LSND and MiniBooNE results [81]. In addition, data from neutrino capture sources in the early Gallium-based solar neutrino experiments of SAGE [84] and GALLEX [85] indicated a deficit of neutrinos as well, now known as the Gallium anomaly. The Gallium anomaly has been analyzed to be significant at $\sim 3\sigma$ [86] and has also been explored as a possible hint of a sterile neutrino in the same region of mass splitting and mixing as the other two anomalies.

1.4 Scope of this Work

As we approach another era of great discovery for neutrinos, it has become immensely clear that high precision measurements will be needed to answer the questions of neutrino mass hierarchy, absolute mass scale, CP-violation in the lepton sector, Majorana or Dirac nature, or any of the anomalies. For this reason, quantifying and examining background signals and perturbations to the first-order neutrino signal becomes critical to the future of neutrino physics. Adjustments, such as the non-equilibrium correction, have already shown that these effects can have a significant result. For this work, the reactor antineutrino source is selected and the origin and significance of some corrections are explored. These corrections are derived and quantified in Chp. 3 and Chp. 4. In addition, an application of antineutrinos as a non-proliferation method in order to provide a civilian use for neutrinos, is described in Chp. 5.

The next chapter will provide a specific and detailed introduction to reactor antineutrinos. The parameterization of the propagation of neutrinos, including oscillation and matter effects

is outlined first. This is followed by a description of the reactor physics that impacts the antineutrino source. Finally, the detection methods for reactor antineutrinos, with a specific focus on inverse beta-decay (IBD) in a liquid scintillator detector is described as it will be used frequently to derive event rates. Along the way some important reactor neutrino experiments are highlighted, including the conversion of a beta spectrum to an antineutrino spectrum and the pioneering work by Cowan and Reines.

Chapter 2

Reactor Neutrinos Introduction

This chapter serves as a mathematical and physics-based introduction to the neutrino, with a focus on reactor antineutrinos. The concept of neutrino oscillations is derived and formulated, beginning with two-neutrino oscillation in vacuum. Next, the plane-wave approximation is introduced, along with its assumptions, and the corresponding oscillation probabilities are calculated. For completeness, the matter-effect and the corresponding MSW resonance are presented in the two-neutrino framework as well. Finally, extrapolation to three-neutrino oscillation is presented and a summarization of the current state of the neutrino mixing matrix is given. After this description of neutrino oscillation, the focus shifts to the production of antineutrinos in a nuclear reactor, specifically in the beta-decay of fission fragments. The Institute Laue Langevin (ILL) measurements, critical to the determination of the reactor antineutrino flux, are discussed, along with a summarization of the beta-conversion techniques and corrections. An alternative method of determining the antineutrino flux of specific reactor nuclides is also covered, via an analytical solution of a series of differential equations known as the Bateman equations. Finally, the detection methods for reactor antineutrino experiments is discussed. The description will focus on the inverse beta-decay (IBD) reaction and the corresponding signals in a scintillating material as it is the most common detection mechanism for reactor antineutrinos. Major reactor experiments are presented during this chapter in the context of mixing parameter determination, reactor source determination, and detection methods.

2.1 Neutrino Oscillations

First, the description of neutrino propagation is covered, which mainly focuses on the bizarre phenomenon of neutrino oscillation. Neutrino oscillation is a quantum mechanical effect that occurs in the lepton sector of particle physics. This concept was first explored by Pontecorvo [30] for $\nu \leftrightarrow \bar{\nu}$ oscillations and finally expressed in the leptonic flavor framework

by Maki, Nakagawa, and Sakata [32] and also Pontecorvo [87] again. The phenomenon arises because the flavor eigenstates and mass eigenstates of neutrinos are not equivalent. Neutrinos are produced and detected in the flavor eigenstate, where we define ν_e as the neutrino producing an e in a $W^{\pm}$ exchanging, or charged-current (CC), process, ν_μ as the neutrino producing a μ in a CC process, and ν_τ as the neutrino producing a τ in a CC process, collectively labeled ν_α where $\alpha = e, \mu, \tau$. However, the propagation of neutrinos occurs in the mass eigenstates, commonly denoted as ν_i where $i = 1, 2, 3$. The claim that the flavor and mass eigenstates are not equivalent means that $\nu_\alpha \neq \nu_i$ for any combination of $\alpha = e, \mu, \tau$ or $i = 1, 2, 3$, which identifies ν_α and ν_i as different bases. The simplest oscillation derivation is covered next, vacuum oscillation.

2.1.1 Vacuum Oscillations

The simplest framework for neutrino oscillation is given by the plane wave quantum mechanical approximation for two neutrinos in vacuum. It must be noted that in order to reach this simplified expression some assumptions are made, which are mentioned along with the calculation. Let $|\nu_i\rangle$ denote a time-independent eigenstate of the propagation Hamiltonian, where propagation occurs with the mass eigenstate ν_i. Then, the time-evolution of this stationary state can be written as

$$|\nu_i(t)\rangle = e^{-iE_i t} |\nu_i\rangle \tag{2.1}$$

with some neutrino energy $E_i = \sqrt{p_i^2 + m_i^2}$, with $c = 1$. One can rewrite the time evolution of a mass eigenstate $|\nu_i\rangle$, given by Eq. 2.1 where each eigenstate has a different m_i, in terms of the flavor eigenstates as well. As neutrinos are detected in the flavor state it is convenient to write appearance or disappearance probabilities in terms of these flavor states $|\nu_\alpha\rangle$. This requires an expression for $|\nu_\alpha\rangle$ in terms of $|\nu_i\rangle$, which is given by a unitary transformation matrix between the flavor and mass eigenstates:

$$|\nu_\alpha\rangle = \sum_i U^*_{\alpha i} |\nu_i\rangle \tag{2.2}$$

where the matrix $U^*_{\alpha i}$ is the complex conjugate of a unitary matrix that rotates between the flavor and mass bases. It should be noted that the unitarity of the neutrino mixing matrix is technically assumed here and measurements of unitarity via the so-called unitarity triangles, such as in the quark mixing [88], could support this. Using Eq. 2.2, the expression for the oscillation probability from one known initial flavor ν_α to a different flavor ν_β after some time t is given by

$$\mathcal{P}_{\nu_\alpha \to \nu_\beta} = |\langle \nu_\beta | \nu_\alpha(t) \rangle|^2 = \sum_{i,j} \left| \langle \nu_j | e^{-iE_i t} U_{\beta j} U^*_{\alpha i} |\nu_i\rangle \right|^2 \to \sum_{i,j} \left| \langle \nu_j | e^{-i(p_i + m_i^2/(2E))t} U_{\beta j} U^*_{\alpha i} |\nu_i\rangle \right|^2 \tag{2.3}$$

where the neutrinos are treated as relativistic, such that $E_i = \sqrt{p_i^2 + m_i^2} \rightarrow (p_i + m_i^2/(2E))$. Here, the first assumption is required. A quick examination of Eq. 2.3 shows a dependence on the neutrino momentum p_i and energy E. For a given detection scheme, the total neutrino energy may be obtained, but the individual momentum of the propagating mass state p_i is unobtainable. The reason behind this is that neutrinos are detected in the flavor basis, but the individual momenta of each mass eigenstate is available only in the propagation basis. With the equal momentum assumption all neutrino mass states are assumed to have the same momentum $p_i = p$ and the resulting factor of e^{-ipt} in Eq. 2.3 appears only as a phase, which cancels via the modulus squared. The final result is an oscillation probability with the form of Eq. 2.4.

$$\mathcal{P}_{\nu_\alpha \rightarrow \nu_\beta} = \sum_{i,j} |\, \langle \nu_j |\, e^{-i(m_i^2/(2E))t} U_{\beta j} U^*_{\alpha i}\, |\nu_i\rangle\, |^2 \tag{2.4}$$

This equal momentum assumption has been found to violate Lorentz invariance at the production source [89] unless a specific reference frame, with no physical significance, is chosen and, therefore, cannot be justified. A similar fate applies to the equal energy assumption [89]. Neutrino oscillation has been explored in many new frameworks to address the problems of the traditional plane-wave approximation. Some of these frameworks and their oscillation results are summarized in Ref. [90]. Corrections have been found to the traditional derivation, say in relativistic quantum mechanics [91], or the wave-packet model [92–94], or even in quantum field theory approaches [95], but all have the same underlying oscillation probability structure of Eq. 2.4 with respect to reasonable experimental designs. Essentially, as the other frameworks of neutrino oscillations produce only negligible corrections to the plane-wave approximation, with respect to practical neutrino experiments, one can simply continue with the plane-wave approximation and leave the other frameworks to their respective references listed above. Thus, the simplification made in Eq. 2.3 is valid for our experimental cases.

Continuing with Eq. 2.4, the generic neutrino oscillation between two different flavor states α and β separated by a time t can be written as Eq. 2.5.

$$\mathcal{P}_{\nu_\alpha \rightarrow \nu_\beta} = |\, \langle \nu_\beta |\, e^{-iE_i t}\, |\nu_\alpha\rangle\, |^2 = \sum_{i,j} U_{\alpha j} U^*_{\beta j} U^*_{\alpha i} U_{\beta i} e^{-i\frac{\Delta m^2_{ij} L}{2E}} \tag{2.5}$$

where the equal-momentum assumption and the ultra-relativistic limit[1] are used, so that $t \approx L$, where L is the neutrino propagation distance and $\Delta m^2_{ij} = m_i^2 - m_j^2$, is the squared mass-splitting. For a simple two-state neutrino oscillation, with $|\nu_\alpha\rangle$ and $|\nu_\beta\rangle$ as the flavor eigenstates and m_1 and m_2 as the two mass eigenvalues, the unitary transformation matrix is given as the rotation between these two bases by a single angle θ. This rotation is given by:

$$U = \begin{pmatrix} \cos\theta & \sin\theta \\ -\sin\theta & \cos\theta \end{pmatrix} \tag{2.6}$$

[1] with $c = 1$

This rotation matrix is accurate up to a phase, which does not appear in the oscillation probabilities, so this expression can be arbitrarily selected with no loss of generality. Applying the U given in Eq. 2.6 to the oscillation probability in Eq. 2.5 yields the two common types of experimental evidence for oscillation, appearance and disappearance channels. The appearance channel is the search for the appearance of a flavor β from an (ideally) pure α-neutrino source. This probability is given by:

$$\mathcal{P}_{\nu_\alpha \to \nu_\beta} = \sin^2(2\theta) \sin^2 \left(\frac{\Delta m^2_{12} L}{4E} \right) \tag{2.7}$$

Neutrino experiments utilize different values for the baseline L and neutrino energy E in order to determine values of θ and Δm^2_{12}. Effectively, the amplitude of the oscillations will be determined by the value of $\sin^2 2\theta$ and the period of oscillation is given by Δm^2_{12} for an oscillating parameter of L/E. It should be noted that the mixing angle θ is a fundamental constant, as are the masses of the neutrino states and, thus, Δm^2_{12}. For reactor experiments the detected antineutrino energy falls within the range of $1.8\,\text{MeV} \lesssim E \lesssim 10\,\text{MeV}$, where the lower bound is typically restricted by the use of inverse beta-decay (IBD) as an antineutrino capture mode, but this will be covered in detail later.

The second neutrino channel is the disappearance channel, which looks for a deficit of flavor α neutrinos from a pure α-neutrino source. This disappearance probability can be solved for trivially via the unitarity condition and is given by:

$$\mathcal{P}_{\nu_\alpha \to \nu_\alpha} = 1 - \sin^2(2\theta) \sin^2 \left(\frac{\Delta m^2_{12} L}{4E} \right) \tag{2.8}$$

An important note is the relation of both oscillation probabilities to the mass splitting Δm^2_{12}. For equivalent mass eigenstates $m_1 = m_2$ as well as massless neutrinos $m_1 = m_2 = 0$, we see no oscillation at all. It must also be noted that the vacuum oscillation probabilities are completely insensitive to both the hierarchy (i.e. whether we have $m_1 > m_2$ or vice versa) and the absolute masses themselves. The former comment can be noted in that the oscillation probabilities are invariant under $\Delta m^2_{12} \to \Delta m^2_{21}$ due to the $\sin^2$ nature. Luckily, neutrino oscillations through matter have an additional effect, which provides a sensitivity to the hierarchy. The matter oscillations are covered next.

2.1.2 Oscillations in Matter

The results of the previous section for the oscillation probabilities in Eq. 2.7 and Eq. 2.8 require oscillations in vacuum, but most neutrino experiments involve some portion of oscillations occurring in matter. Here, neutrino oscillations in matter are presented, again for two flavor states, one of which is the electron neutrino ν_e. Mathematically, vacuum oscillation has a relatively simple propagation Hamiltonian depending solely on the neutrino masses and energy given by $M^\dagger M/(2E)$, where M is the neutrino mass matrix, which is

diagonal in the mass eigenstates. However, the inclusion of the matter effect involves an additional term that depends on the electron density of the material the neutrino travels through. The Schrödinger equation can be expressed with this matter addition resulting in a total Hamiltonian:

$$i\frac{d}{dt}\begin{pmatrix}\nu_\alpha\\ \nu_\beta\end{pmatrix} = \frac{1}{2E}\left[M^\dagger M + H_{\text{matter}}\right]\begin{pmatrix}\nu_\alpha\\ \nu_\beta\end{pmatrix} \tag{2.9}$$

where a matter Hamiltonian H_{matter} now contributes, which will affect the ν_e states, but leave the ν_α ($\alpha \neq e$) states unaffected as ordinary matter contains only electrons and neither muons nor taus.

The nonzero electron density in matter allows for CC interactions with the ν_e, which are disallowed with other neutrino flavor states ν_α where $\alpha \neq e$. It should be noted that NC interactions can occur between electrons and any flavor neutrino, but this does not lead to any hierarchy sensitivity as it affects all states equally. Effectively, the inclusion of matter allows for interactions such as those in Fig. 2.1 below, which are only present when there are electrons to interact with.

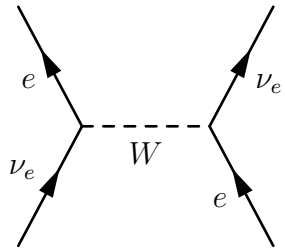

Figure 2.1: Charged-Current interactions with electron neutrinos ν_e in ordinary matter. Figure by author.

This added interaction affects the propagation of neutrinos in a concept known as the matter effect, first pioneered by Wolfenstein [45] and later applied to derive resonant effects by Mikheyev and Smirnov [44]. As the matter effect only affects the ν_e, H_{matter} will have only one entry in its 2×2 matrix, whereas the NC interactions would be proportional to the identity matrix. An interesting note is that collective neutrino oscillation, induced by self-interactions, will appear as off-diagonal terms in H, but these only occur in extreme environments [96]. Restructuring Eq. 2.9 with the mixing matrix and adding in a term A for the matter effect yields:

$$i\frac{d}{dt}\begin{pmatrix}\nu_\alpha\\ \nu_\beta\end{pmatrix} = \frac{1}{2E}\left[U\begin{pmatrix}m_1^2 & 0\\ 0 & m_2^2\end{pmatrix}U^\dagger + \begin{pmatrix}A & 0\\ 0 & 0\end{pmatrix}\right]\begin{pmatrix}\nu_\alpha\\ \nu_\beta\end{pmatrix} \tag{2.10}$$

where one can now acquire the new eigenvalues of the combined Hamiltonian to determine the mass eigenstates, splittings, and mixing angles in matter. Here, a time-independent matter effect is assumed for simplicity. In reality, the matter effect, which is a function

of the electron density, may change during propagation depending on the matter profile as originally discussed [44]. For the sake of simplicity, a simple uniform matter profile is used to derive these matter parameters. Upon diagonalization of the total propagation Hamiltonian in Eq. 2.10, one arrives at new energy eigenvalues $\tilde{m}_1$ and $\tilde{m}_2$, where the $\tilde{}$ indicates the effective neutrino parameter in matter. These are:

$$\tilde{m}^2_{1/2} = \frac{A + m_1^2 + m_2^2}{2} \mp \frac{1}{2}\sqrt{A^2 - \Delta m^2(2A\cos\theta - \Delta m^2)} \tag{2.11}$$

where the $-$ is for $\tilde{m}_1$ and the $+$ is for $\tilde{m}_2$. Eq. 2.11 can be used to solve for the effective mass splitting ($\Delta\tilde{m}^2 = \tilde{m}_2^2 - \tilde{m}_1^2$) in matter. In addition, a re-diagonalization allows one to write the mixing matrix U with the new effective mixing angle $\tilde{\theta}$ in matter. After simplification, the following matter neutrino parameters are given by:

$$\begin{aligned} \Delta\tilde{m}^2 =& \Delta m^2\sqrt{(A/\Delta m^2 - \cos 2\theta)^2 + \sin^2 2\theta} \\ \sin 2\tilde{\theta} =& \frac{\sin 2\theta}{\sqrt{(A/\Delta m^2 - \cos 2\theta)^2 + \sin^2 2\theta}} \end{aligned} \tag{2.12}$$

where, as expected, the case of no matter interaction, $A = 0$, returns the effective neutrino parameters to their vacuum values.

The expression for $\sin 2\tilde{\theta}$ in Eq. 2.12 leads to a very intriguing oscillation effect, first pointed out by Mikheyev, Smirnov [44], and Wolfenstein [97], so it is dubbed the MSW effect. Recalling that the oscillation amplitude is proportional to $\sin^2 2\theta$, there is an opportunity to maximize the neutrino mixing via $\sin 2\tilde{\theta} = 1$ when $A/\Delta m^2 = \cos 2\theta$. When a value is inserted for the matter parameter $A = \pm 2\sqrt{2}G_F n_e E$ one can identify how the sign of Δm^2 impacts the oscillation probabilities, where $A > 0$ is for neutrinos and $A < 0$ is for antineutrinos. Adding this expression for A into Eq. 2.12, the MSW resonance occurs for neutrinos ($A > 0$) when $\Delta m^2 > 0$, corresponding to normal hierarchy ($m_2 > m_1$) and for antieneutrinos ($A < 0$) when $\Delta m^2 < 0$, corresponding to inverted hierarchy ($m_1 > m_2$). Therefore, the sign of Δm^2 can be determined from MSW resonances using a neutrino and antineutrino source. Note that there is a fake CP violation as the matter effect is different for ν than $\bar{\nu}$, which can mask any evidence of actual CP violation [98]. The MSW resonance and matter effect have had applications beyond the mass hierarchy, from stellar collapse to amplified oscillations of electron neutrinos into some massive sterile neutrino ($\nu_e \to \nu_s$) [97, 99] and even an early attempt at explaining the solar neutrino puzzle [100].

Now that basic neutrino oscillation and the matter effect in a two-neutrino framework has been covered, three-neutrino oscillation will be derived.

2.1.3 Three Neutrino Oscillations

The previous two derivations of both the oscillation probabilities in Eq. 2.7 and Eq. 2.8 as well as the change of oscillation parameters by the introduction of matter effects in

Eq. 2.12 have assumed two neutrino flavors. This has made the calculations easier, but the data from the Large Electron Positron (LEP) collider indicates strong evidence for 3 neutrino generations that couple to the Z^0 boson with masses below half the Z^0 mass [101] in agreement with the recent Planck data [102]. Combining these results with the confirmation of ν_τ appearance [103] provides ample evidence for 3 neutrino flavors. Therefore, the full 3-generation neutrino mixing framework is presented next.

With three neutrinos, three complex rotations between the flavor and mass eigenstates are needed. This 3×3 matrix is given by 3 mixing angles θ_{ij} and 1(3) CP-violating phase(s) for Dirac (Majorana) neutrinos where the remaining parameters have been absorbed by unitarity, orthogonality, or a rephrasing of angles. One popular representation of the mixing matrix U, which highlights the different areas of neutrino research is as follows:

$$U = \begin{pmatrix} 1 & 0 & 0 \\ 0 & c_{23} & s_{23} \\ 0 & -s_{23} & c_{23} \end{pmatrix} \begin{pmatrix} c_{13} & 0 & s_{13}e^{-i\delta} \\ 0 & 1 & 0 \\ -s_{13}e^{i\delta} & 0 & c_{13} \end{pmatrix} \begin{pmatrix} c_{12} & s_{12} & 0 \\ -s_{12} & c_{12} & 0 \\ 0 & 0 & 1 \end{pmatrix} \begin{pmatrix} 1 & 0 & 0 \\ 0 & e^{i\phi_1/2} & 0 \\ 0 & 0 & e^{i\phi_2/2} \end{pmatrix} \quad (2.13)$$

where $c_{ij} = \cos\theta_{ij}$, $s_{ij} = \sin\theta_{ij}$, δ is the CP-violating phase, and the extra Majorana phases ϕ_i, which do not appear in oscillation probabilities [104], are included for completeness.

This formulation of U in Eq. 2.13 is designed to separate neutrino oscillations into an atmospheric mixing, governed by θ_{23} and mass splitting Δm^2_{23}, a reactor mixing, governed by θ_{13} and mass splitting Δm^2_{13}, which is often used with the approximation that $\Delta m^2_{13} \sim \Delta m^2_{23}$, and a solar mixing, governed by θ_{12} and mass splitting Δm^2_{12}. All neutrino mixing parameters here are fundamental constants, like the electron mass, and thus have been probed by numerous experiments to obtain accurate values. A recent (2013) analysis of the neutrino parameters, assuming 3 neutrino oscillation, has been given in Ref. [55], which summarizes the current best-fits and tensions of the mixing angles, mass splittings, and Dirac CP-violating phase.

A brief description of the major experiments behind the values associated with Tab. 1.1 is necessary. Some known and unknown properties of neutrino oscillation will also be provided. The mixing angle of θ_{23}, dubbed the atmospheric mixing due to its original estimate from analyses of $\nu_\mu \to \nu_e$ oscillation from cosmogenically produced neutrinos, has its strongest estimate, as does the atmospheric splitting Δm^2_{23} from long-baseline accelerator experiments such as T2K [52]. The reactor mixing angle θ_{13} was measured to high precision originally by the Daya Bay experiment [53] and now by Double Chooz [105] and RENO [48]. Finally, the solar mixing θ_{12} and splitting Δm^2_{12} have been accurately estimated from a combination of accelerator, short-baseline, and solar experiments with the KamLAND reactor data [51]. Note that, unlike the other mass splitting, the sign of Δm^2_{12} is known due to the matter effects evident in solar neutrino oscillation, as discussed in Chp. 2.1.2. With the knowledge that $m_2 > m_1$ from solar data, the neutrino mass hierarchy can be illustrated as in Fig. 2.2. The colored sections indicate the mixings of the different flavor neutrinos with the mass eigenstates, where the exact ratios are calculated from the mixing matrix U with the values in Tab. 1.1.

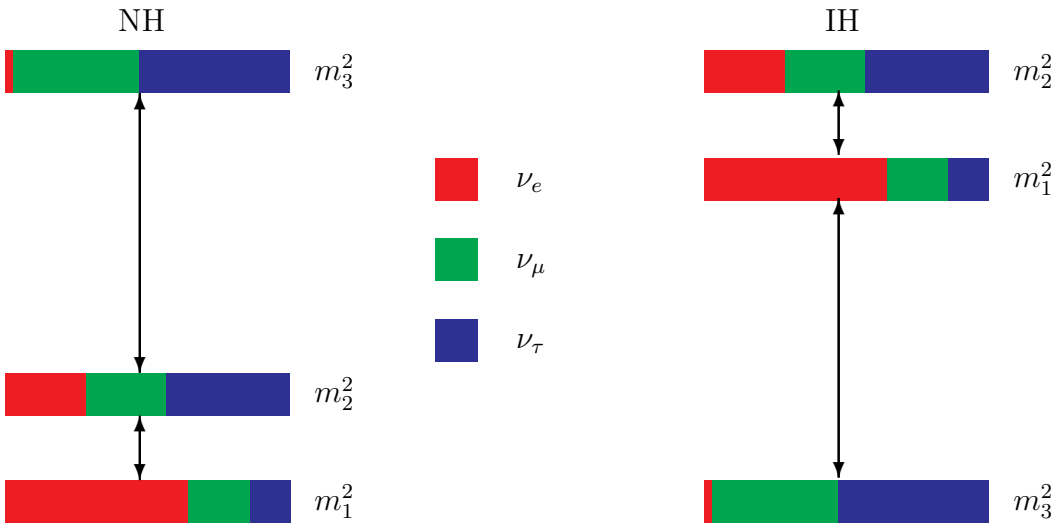

Figure 2.2: Illustration of the neutrino mass hierarchy and relative mixings for normal hierarchy (NH), where $m_3^2 > m_2^2 > m_1^2$, and inverted hierarchy (IH), where $m_2^2 > m_1^2 > m_3^2$. The values listed in Tab. 1.1 are used to determine the relative mixings of ν_e (red), ν_μ (green), and ν_τ (blue) via $|U_{\alpha i}|^2$ for a flavor eigenstate α and mass eigenstate i. Figure by author.

A key component missing in the neutrino sector is the absolute mass of the neutrinos. Recall that oscillation simply depends on the squared mass differences, as does the hierarchy. So far, we have given no indication for the mass of any individual eigenstate. The absolute neutrino mass can be measured via ultra-high energy resolution of the beta-decay endpoint, initially pointed out by Fermi [7]. The neutrino mass would reveal itself as a deviation from the endpoint energy. Searches of this type have been ongoing and typically use Tritium decay, due to the fact that energy resolution typically follows $E/\Delta E$ in β-spectroscopy and Tritium has a low endpoint energy of $\sim 18.6\,\text{keV}$ [106]. The latest upper limits of $m_{\nu_e} \lesssim 2\,\text{eV}$ at the 95% confidence level are given by the Mainz and Troitsk experiments [107,108]. Other limits on the total neutrino mass can come from Big Bang nucleosynthesis (BBN) or cosmic microwave background (CMB) data [109], but these limits can be model-dependent. In addition, neutrino time of flight information from supernova 1987A [110] can be used, but these limits are currently less stringent.

A second missing element is the value for the CP-violating Dirac phase δ, which appears in oscillation probabilities with a coefficient equal to a product of all mixing angles. Using the Cabibbo-Kobayashi-Maskawa (CKM) [111, 112] matrix for quark mixing as an analogy, one can derive the forms of CP-violation in the neutrino mixing matrix. These terms follow the structure of:

$$\mathcal{J} = s_{13}s_{12}s_{23}c_{13}^2c_{12}c_{23}\sin(\delta) \tag{2.14}$$

where the common form of $c_{ij} = \cos(\theta_{ij})$ and $s_{ij} = \sin(\theta_{ij})$ is adopted again. Therefore, the

CP-violating terms in vacuum oscillations are proportional to Eq. 2.14, the so-called Jarlskog invariant, following Ref. [113], which originally analyzed the CP-violation available in the CKM matrix, but is trivially applicable to neutrino oscillations [114]. The form of Eq. 2.14 is significant as it indicates that the effect of CP-violation can only be seen if all mixing angles are not integer nor half-integer multiples of π, the contrary resulting in $\mathcal{J} = 0$. It also indicates that the size of any CP-violation will be limited by the smallest mixing angle, θ_{13} in this case.

The final missing oscillation quantity is the Majorana phases, which will not affect appearance or disappearance studies, but can act as a consequence in specifically designed experiments. One such concept is the search for neutrino-less double beta-decay ($0\nu\beta\beta$) processes [115]. This type of decay utilizes the fact that Majorana particles are their own antiparticles, thus the neutrino and antineutrino could annihilate as a virtual neutrino shared between two W bosons. This type of decay would result in a lepton number violation of two units. In experimental terms, a 'smoking gun' for $0\nu\beta\beta$ would be a peak in the observed beta spectrum at the endpoint energy as all of the energy has been acquired by the electrons. Experiments searching for $0\nu\beta\beta$ decays use sources with immensely large half-lives as the decay mode is highly forbidden. Current limits on the half-life of these decays are $T_{1/2}^{0\nu\beta\beta} \gtrsim 2 \times 10^{25}\,\text{yr}$ from ^{136}Xe [116, 117] and ^{76}Ge [19] searches. Other than the highly disputed claims of the so-called Heidelberg-Moscow experiment [118], which are currently excluded at the $\sim 97\%$ confidence level by KamLAND-Zen [117], no detection of $0\nu\beta\beta$ decay has occurred. As the Majorana phases do not impact our work directly, they are ignored in future calculations.

Another side note concerns the possible existence of additional neutrinos to the standard 3 flavor families: ν_e, ν_μ, and ν_τ. New flavors can be trivially added to the mixing matrix U, but will complicate oscillations. These extra neutrinos, if they involve mass splittings of $\mathcal{O}(1\,\text{eV}^2)$, could not couple to the weak interaction as it is forbidden from the LEP data [101]. For this reason, these extra neutrinos are often dubbed as 'sterile' neutrinos and would only couple to the Standard Model via neutrino oscillations and the Higgs. Incorporation of sterile neutrinos into the current 3-neutrino oscillation framework has been tested for various models, such as the so-called $3+1$ (addition of one sterile with $\Delta m^2_{41} \sim 1\,\text{eV}^2$), $3+2$ (two steriles $\Delta m^2_{51} > \Delta m^2_{41} > 0$), and $1+3+1$ (two steriles $\Delta m^2_{51} > 0$ and $\Delta m^2_{41} < 0$) scenarios. Most analyses have found that the incorporation of more free parameters (steriles) allows for better fits to oscillation data, but this effect is mostly due to the increase in the degrees of freedom. In addition, it must be noted that the incorporation of more than 1 sterile neutrino begins to draw tension from Big Bang Nucleosynthesis [119] and Cosmic Microwave Background [102] data for the value of N_{eff}, the effective number of neutrinos. Currently, the choice of a $3+1$ model is highly suppressed due to the tension between appearance and disappearance data. The $3+2$ and $1+3+1$ models fit the global data better, but still show tension between appearance and disappearance results. An excellent review of these sterile models and their fits with oscillation experiments can be found in Ref. [120] and Ref. [121]. Further discussion of steriles is left to Chp. 3 and Chp. 4, where the spent fuel and non-linear

corrections are discussed, including their impact on the reactor antineutrino anomaly, one of the experimental observations driving the search for sterile neutrinos.

Neutrino oscillation has been introduced and derived in both the two and three-flavor scenarios. The large mixing-angle (LMA) solution is supported by data and allows for a de-coupling of the atmospheric and solar splittings for appropriate baseline experiments. Most reactor experiments involve baselines in the tens of meters to a few kilometers, allowing for the $3 \rightarrow 2$ oscillation simplification, derived in Eq. 2.7. Next, the treatment of the reactor source is considered.

2.2 Antineutrino Production in Nuclear Reactors

Nuclear reactors function as a source of electron antineutrinos through the beta-decay process of Eq. 1.1 of neutron-rich nuclides. For the scope of this work the production vertex need not be considered in the framework of the electro-weak interaction, but instead can be approached with the low-energy approximation of Fermi's theory [7]. Fermi's theory allows one to calculate the density of states for decay processes with knowledge of the initial and final phase spaces, mostly governed by the nuclear matrix elements. This density of states can then be used to determine the energy spectrum of beta-decay for both the betas and, as will be discussed in Chp. 2.2.1, the antineutrinos. Note that antineutrinos are not a direct result of the fission process itself. Fission is given, in the case of ^{235}U, by

$$n + ^{235}\mathrm{U} \rightarrow \eta n + F_1 + F_2 + \sum \gamma \tag{2.15}$$

where an incident neutron n on the fissile nuclide ^{235}U with atomic mass $A = 235$ and atomic number $Z = 92$ produces η prompt neutrons, some gamma rays γ, and fission fragments F_1 and F_2, where the vast majority of fissions result in two fragments. It is the beta-decays of these fragments, F_1 and F_2, and their subsequent daughters, that generate the antineutrinos from a nuclear reactor. Each fission will produce around 200 MeV [122], with the majority of this residing in the kinetic energy of the fragments. Two to three prompt neutrons [123] (the exact number depending on the fissile) are also produced, which can eventually incite further fissions via the reaction in Eq. 2.15. Some of the remaining energy is produced in the form of gamma rays, but these usually deposit their energy in the medium. Finally, the two fragments will beta-decay an average of 6 times to stability [124], so ~ 6 antineutrinos are produced per fission. A different distribution of fission fragments is produced based on the nuclide being fissioned and the initial neutron energy, but all fissions will generate the famous double-hump fragment distribution. This fragment distribution is illustrated in Fig. 2.3, which is based upon the Joint Evaluated Fission and Fusion File 3.1.1 (JEFF) thermal fission yields [125]. The trend among the fissiles is that the lower A hump shifts upward for higher A fissiles. Using higher incident neutron energies has the effect of 'filling in' the valley between the humps [126]. Similar fragment distribution data is available in the Evaluated Nuclear Data File (ENDF) report of Ref. [127] with only minor differences.

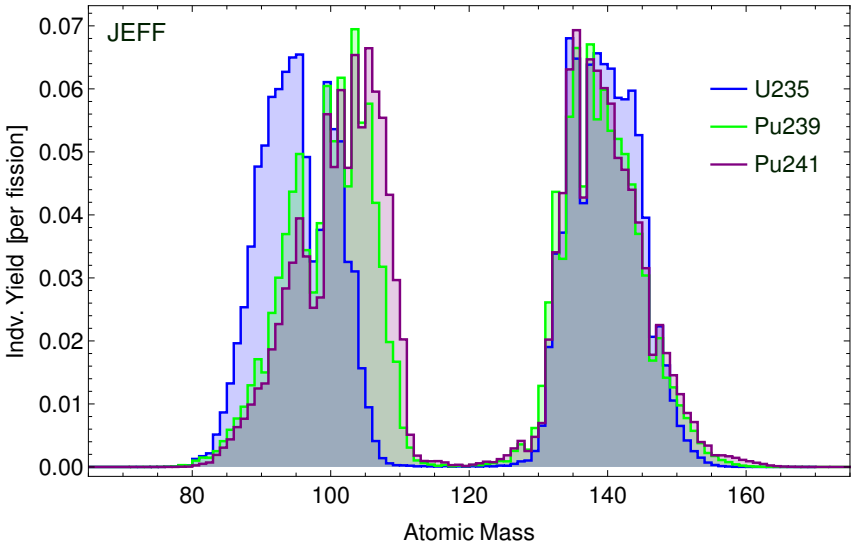

Figure 2.3: Distribution of fission fragments for thermal fission of ^{235}U, ^{239}Pu, and ^{241}Pu based upon the JEFF thermal yields [125]. Figure by author.

The inaccuracy of the various nuclear databases has prompted the calculation of the antineutrino spectrum from individual fissiles to be conducted via virtual beta-branches [128] less sensitive to the majority of errors or absent data in these databases. Efforts to fill in missing or replace inaccurate nuclear data in order to calculate the antineutrino spectrum from the individual beta branches [83, 129], the so-called *ab initio* approach, have shown progress in correcting these databases. For example, a detection bias that overestimated the high energy component of beta-decays, the so-called "pandemonium effect" [130], was found to seriously effect several ^{239}Pu fragments [131]. In any case, it has become quite clear that the *ab initio* approach will require a careful selection of accurate nuclear data from the databases and measurements of inaccurate or missing data by improved methods, such as the total absorption gamma-ray spectroscopy (TAS) method [131, 132].

As different nuclides undergoing beta-decay will produce a different beta and, therefore, different antineutrino spectrum, one can conclude that the fission of each fissile produces a unique antineutrino spectrum. This leads us to consider what the antineutrino spectrum will be for any given fission of a particular fissile. Next, we summarize the attempts to determine the fissile antineutrino yields beginning with the beta-conversion technique pioneered by the ILL measurements.

2.2.1 Extraction of the fissile antineutrino yields

As the fragment nuclide production is primarily governed by the fission rate of the fissiles so, too, is the antineutrino production. This realization lead to the first inception of reactor monitoring with antineutrinos by Borovoi and Mikaelyan [66] in the late 1970s; a 'practical'

use of neutrinos discussed in Chp 5. These notions meant that if one could determine the antineutrino yield produced from a single fission of each individual fissile $N_\nu^f(E)$, the total reactor spectrum can be calculated by weighting the individual fissile spectra with the fission rates:

$$R_T(E) = \sum_{f=1}^{N_f} \mathcal{F}_f N_\nu^f(E) \tag{2.16}$$

where we sum over N_f fissiles, weighting each energy-dependent fissile antineutrino yield $N_\nu^f(E)$ with the fission rates $\mathcal{F}_f$. The notation of Eq. 2.16 hides the complication of the beta-conversion process. Experimentally, what is observed is the beta-spectrum from all fragment decays from fission. Furthermore, the individual fragments may have a variety of possible beta-decays to different excited daughter states. Two methods for determining $N_\nu^f(E)$ have been used to generate antineutrino yields. The first uses the nuclear databases and the fragment distributions of Fig. 2.3 to calculate the total antineutrino yields; this is the *ab initio* approach. The second utilizes the beta-spectra measured from fissions of individual fissiles and converts this into an antineutrino spectrum; this is the beta conversion technique. We summarize the latter, next.

The experimental determination of the beta spectrum, and the subsequent conversion, became known as the ILL measurements for the location of the nuclear reactor used. For most reactors, over 99% of all fissions are caused by four main fissiles, so the ILL measurements focused on ^{235}U [133], ^{239}Pu, and ^{241}Pu [134] with the addition of the Garching measurement of the beta spectra from fissionable ^{238}U [135]. The ILL conversion method, covered in Ref. [136], utilizes energy conservation of the available energy in beta-decay, the endpoint energy E_0. This endpoint energy is shared between the beta particle and the antineutrino. As mentioned, the observed spectrum from the ILL and Garching measurements is the total beta spectrum, composed of a sum of individual beta spectra. Adopting the notation of Ref. [137], an individual beta-spectrum for an allowed decay is given by Fermi's theory [7]:

$$N_\beta(W) = CF(Z,W)p^2(W_0 - W)^2 \tag{2.17}$$

where the electron energy W is given in units of $W = E/(m_e c^2) + 1$ and W_0 is simply W evaluated at the the total energy difference between the two nuclear states E_0. Then, p is the electron momentum in units of $m_e c$, Z is the parent nuclear charge, C is a normalization constant, and the Fermi function $F(Z,W)$ corrects for the interaction between the outgoing electron (or positron in the case of β^+-decay) and the electric field of the nucleus. Explicitly, the Fermi function is given by:

$$F(Z,W) = 2(\gamma+1)(2pR)^{2(\gamma-1)} e^{\pi\alpha ZW/p} \frac{|\Gamma(\gamma + i\alpha ZW/p)|^2}{\Gamma(2\gamma+1)^2} \quad \text{with} \quad \gamma = \sqrt{1-(\alpha Z)^2} \tag{2.18}$$

where R is the nuclear radius and α is the fine-structure constant. Note that R will have an implied dependence on the number of nucleons A. Ignoring the recoil of the nucleus will create the requirement of $W_0 = W + W_\nu$ and allows a beta spectrum to be converted to an antineutrino spectrum by the replacement $W \to W_\nu$, where $W_\nu = W_0 - W$ in Eq. 2.17.

Equation 2.17 along with Eq. 2.18 allows one to determine the beta-spectrum given a particular decay of some parent nuclide to a daughter nuclide. It should be noted that there are additional corrections to the beta-spectrum, on top of Fermi's correction, such as the finite size of the nucleus, the screening effect of the nuclear charge, the radiative effect of virtual photons, and the weak magnetism from induced currents. These are explicitly addressed in Ref [128]. The experimental case of the ILL measurements involved the summed spectra of many beta-decay branches, such that the value measured was actually $N_{T,\beta}(W) = \sum_i N^i_\beta(W, W^i_0)$ where individual beta-spectra $N^i_\beta(W, W^i_0)$ are summed over, each with its own endpoint energy W^i_0, to form the total beta-spectrum.

Using this total beta spectrum and energy conservation for each individual spectrum results in the total antineutrino spectrum

$$N_\nu(W_\nu) = \sum_i N^i_\beta(W^i_0 - W, W^i_0) \tag{2.19}$$

where the total antineutrino spectra is a summation over the i^{th} beta branches N^i_β. Unfortunately, the ILL measurements cannot provide information about which beta-decays occurred for any given fission, meaning this conversion process becomes an inversion or unfolding problem. To solve this, one can form a set of virtual beta branches, where 'virtual' indicates the fact that we do not know the exact decay branch any given beta followed, to reproduce the total measured spectrum. The application of virtual beta branches is as follows:

1. Begin at the highest energy data point E_N in the full beta spectrum $N_{T,\beta}(W)$
2. Take the beta spectrum in some energy slice S from E_{N-1} to E_N where $E_{N-1} < E_N$
3. Fit an allowed virtual beta spectrum $A_1 N^1_\beta(W, W^1_0)$ with a free endpoint W^1_0 and amplitude A_1 to the data within E_{N-1} to E_N
4. Continue the spectrum of $A_1 N^1_\beta(W, E_1)$ below E_{N-1} and subtract it from the total spectrum $N_{T,\beta}(W)$
5. Repeat steps 2-4 until all data points within the slice E_{N-1} to E_N have been fitted with a spectrum $A_i N^i_\beta(W, W^i_0)$
6. Move to the next slice S-1 from E_{N-2} to E_{N-1} and repeat steps 2-5 until all slices have been fitted

This sequence will produce a series of $A_i N^i_\beta(W, W^i_0)$ virtual beta spectra, which can be converted to the total antineutrino spectra via Eq. 2.19.

The original reconstruction of the antineutrino spectrum in Ref. [136] used 25 virtual branches based on Eq. 2.19, with the Fermi function correction, and a generalized calculation of the parent nuclear charge Z for the decaying nuclide. Additional corrections to Eq. 2.17, as well

as a more sophisticated calculation of an effective nuclear charge $\bar{Z}$ were combined to produce extremely accurate antineutrino spectra [128]. The *ab initio* approach has also yielded subsequent antineutrino spectra [83] via virtual beta branches, which are normalized to the ILL beta-spectrum measurements.

One issue that has yet to be examined in this treatment so far is the type of beta-decay transition that occurs. Transitions between nuclear states with different $\Delta J = |J_i - J_f|$, the change in spin, and $\pi = \pi_i \cdot \pi_f$, the change in parity, will have different spectral shapes [128]. Previous calculations have only considered allowed transitions, where $\Delta J \leq 1$ and $\pi = +1$, but a large fraction ($\sim 25\%$) of fragment nuclide decays in a reactor are forbidden and there is evidence that the adjustment from an all-allowed calculation to a partial-allowed and partial-forbidden calculation would be needed to acquire a more accurate spectrum [138]. Additional analysis and insight is being conducted on the reactor spectrum to improve its accuracy currently, but we proceed using the adjusted fissile yields for ^{235}U, ^{239}Pu, and ^{241}Pu according to Ref. [128] and keep the original ILL measurement for ^{238}U [135]. This data is reproduced in Tabs. A.1 - A.4 in the Appendix A.

Once a set of fissile antineutrino yields has been selected, one can calculate the total reactor spectrum via Eq. 2.16 where the fission rates are dependent on the reactor data, such as the power, fuel content, and design. Fission rates of the four major fissiles[2] can be summarized via the fission vector, $\vec{\mathcal{F}} = \{\mathcal{F}_{\mathrm{U235}}, \mathcal{F}_{\mathrm{U238}}, \mathcal{F}_{\mathrm{Pu239}}, \mathcal{F}_{\mathrm{Pu241}}\}$, which will depend on the initial fuel loading of the reactor, the moderator type, the presence of a reflector, and the power history of the reactor. The moderator is the medium that is responsible for shifting the neutron energy of the prompt neutrons from fission. These prompt neutrons, which form the neutron flux, $\phi(E)$, within a reactor, have a mean energy of $\sim 2.0\,\mathrm{MeV}$ [139] after they are emitted from fission reactions. To maintain fission, some of them must be captured by other fissiles to continue the reaction. This concept is tied to the variable known as the effective multiplicity, k_{eff}, a ratio of the number of neutrons captured in the n^{th} fission generation to the number captured in the $(n-1)^{th}$ generation. Then, a $k_{eff} > 1$ indicates an increasing number of fissions with each subsequent fission generation, $k_{eff} < 1$ indicates a decrease, and $k_{eff} = 1$ indicates a constant fission rate. Put another way, for power increases $k_{eff} > 1$, for power decreases $k_{eff} < 1$, and for steady power $k_{eff} = 1$.

Neutrons of any energy can induce fission, but most fissiles have a much larger fission cross-section for lower neutron energies, with the notable exception being fissionable ^{238}U, which only fissions with fast neutrons. This means that shifting the neutron flux from fast neutrons to thermal neutrons, as done with a moderator, will increase the feasibility and efficiency of the reactor in addition to changing $\vec{\mathcal{F}}$. Moderators are chosen based on the desired energy of $\phi(E)$ and the fuel, where water is an excellent thermal moderator as it has nearly maximal energy transfer between it and neutrons due to the similar masses of neutrons and protons.

The reflector in a reactor is a neutron-reflecting medium that elastically scatters neutrons. Reflectors are commonly placed at the edge of a reactor core volume to send stray neutrons

[2]Technically, ^{238}U is categorized as fissionable, **not** fissile

back into the core instead of allowing these neutrons to be lost, which would lower the k_{eff}. Including a reflector has the effect of flattening out $\phi(E)$ with respect to the radial distance from the core center and can also increase the efficiency of a reactor and lower its critical volume. Typically, $\phi(E)$ peaks at the center of the core where the most fissions occur and follows a Bessel function of the first kind radially outward, but the presence of a reflector radially flattens out this Bessel-distribution, making the fission density of the core more uniform.

Reactors are initially loaded with fissile (fissioning) and fertile (generating fissiles) material. For the standard uranium fuel cycle, most commercial reactors operate using low-enriched uranium (LEU), but some utilize mixed-oxide (MOX) fuels containing both uranium and plutonium isotopes. Typically, these MOX fuel assemblies are constructed with recycled uranium and low-enriched plutonium. In addition, specialized reactors can run with natural uranium (NU), which contains 0.711% ^{235}U by weight, but these usually require specific core designs and rarer moderators. Finally, research and naval reactors are often fueled with highly-enriched uranium (HEU). As the reactor burns through the fuel, the composition changes in a process known as burnup. Fissile nuclides deplete over irradiation time, but can also be produced via fertile nuclides such as the common plutonium production method:

$$^{238}\mathrm{U} + n \rightarrow {}^{239}\mathrm{U} \xrightarrow{\beta} {}^{239}\mathrm{Np} \xrightarrow{\beta} {}^{239}\mathrm{Pu} \tag{2.20}$$

where ^{238}U, the fertile nuclide, captures a neutron producing ^{239}U, which has a beta-decay chain with a collective halflife of $\sim 2\,\mathrm{d}$ to ^{239}Pu, a fissile nuclide. This results in a shift in $\vec{\mathcal{F}}$ for LEU and HEU cores from uranium to plutonium-dominated over the irradiation time of the reactor. As the antineutrino yields differ for each fissile, see Fig. 5.1, this shift in $\vec{\mathcal{F}}$ produces a corresponding shift in the reactor antineutrino spectrum over the course of a reactor irradiation cycle. This shift has been seen in preliminary data [67, 68, 140] and reproduced with reactor simulations [141], with Eq. 2.20 being just one example of fuel evolution. Additionally, most reactors will shut down to refuel, typically replacing about one third of the fuel with fresh fuel, which also changes $\vec{\mathcal{F}}$.

With the ILL and Garching measurements and the analyses incorporating the corrections to the Fermi theory we can determine the antineutrino yields for a single fission of each major fissile $N_\nu^f(E)$. Then, with a knowledge of the fission vector $\vec{\mathcal{F}}$, one can determine the total reactor antineutrino spectrum via Eq. 2.16. This process represents the first and primary method of determining a reactor antineutrino spectrum. In reality, there are additional reactor-based corrections that need to be considered to produce the true reactor antineutrino spectrum. For example, the use of the ILL fissile yields will not account for any long-lived accumulation of nuclides, rather it assumes that all neutrinos are emitted at the time of fission. Corrections must then be made for these long-lived nuclides as in Ref. [83]. The spent fuel from reactors, which is typically located near the core, provides an additional antineutrino signal that must be accounted for as we describe in Chp. 3. Additionally, the short irradiation times of the ILL measurements will not account for some nuclide accumulation due to neutron captures, covered in Chp. 4. The neutron capture, or non-linear,

correction can be solved for in a nuclide-by-nuclide manner using decay equations in the complex reactor environment, described next. The spent fuel correction will be derived from reactor simulations, which utilize a similar, but computational, method, discussed in Chp. 3.

2.2.2 Calculations using nuclear decay equations

Nuclear decay equations involve the relatively simple linear differential equations that govern beta-decay. The solution to the linear set of nuclides will yield the abundances of these nuclides in an analytical fashion, which can then be turned into a decay rate and corresponding antineutrino spectrum. This concept was first explored by Bateman [142] and are, thus, named the Bateman equations. The set of linear differential equations assumes that each nuclide in a decay chain of length m is fed only through its parent. There is a master parent for the entire chain N_1, which only decays, and a final stable daughter N_m, which is only fed by N_{m-1}. These assumptions form a useful introduction for the nuclear reactor environment, but certainly require adjustments to account for the yields of the fission fragments per fission as given in Fig. 2.3 as well as the neutron-captures from neighboring isotopes. The general form of the simplified Bateman equations is given by the set of differential equations along a beta-decay chain:

$$\begin{aligned} \frac{dN_1}{dt} =& -\lambda_1 N_1 \\ \frac{dN_i}{dt} =& \lambda_{i-1} N_{i-1} - \lambda_i N_i \\ \frac{dN_m}{dt} =& \lambda_{m-1} N_{m-1} \end{aligned} \tag{2.21}$$

where λ_i is the decay constant of the i^{th} nuclide, the nuclide abundances have an inherent time-dependence t, and N_i represents the abundance of the i^{th} nuclide in a decay chain, where the chain runs numerically from $i = 1, ..., m$. The general solution to Eq. 2.21 is the following, originally derived by Bateman [142]:

$$\begin{aligned} N_n(t) =& \frac{N_1(0)}{\lambda_n} \sum_{i=1}^{n} \lambda_i \alpha_i e^{-\lambda_i t} \\ \alpha_i =& \prod_{j=1, j\neq i}^{n} \frac{\lambda_j}{\lambda_j - \lambda_i} \end{aligned} \tag{2.22}$$

where the only nuclide with a non-zero initial condition (IC) is the chain parent and Eq. 2.22 assumes no decay constants are equivalent, that is $\lambda_i \neq \lambda_j$ for $i \neq j$.

An issue arises when the decay constants are close in value, which leads to infinities in the α_i parameter. This resonance issue was resolved by adjusting the decay constants by an infinitesimal shift and performing a Taylor expansion [143]. Additional methods of solving the Bateman equations include the use of a matrix exponential [144], where the set of differential equations is linked via a correlation matrix $\mathbf{A}$ that connects the various nuclides

together via the decay constants. Then, the set of differential equations is given by:

$$\begin{pmatrix} N_1'(t) \\ N_2'(t) \\ \vdots \\ N_m'(t) \end{pmatrix} = \begin{pmatrix} -\lambda_1 & 0 & 0 & \dots & 0 & 0 \\ \lambda_1 & -\lambda_2 & 0 & \dots & 0 & 0 \\ \dots & \dots & \dots & \dots & \dots & \dots \\ 0 & 0 & 0 & \dots & \lambda_{m-1} & -\lambda_m \end{pmatrix} \begin{pmatrix} N_1(t) \\ N_2(t) \\ \vdots \\ N_m(t) \end{pmatrix} \tag{2.23}$$

where the first vector of length m, $\mathbf{N}'(t)$, is the first time-derivative of the nuclide abundances, $\mathbf{A}$ is the $m \times m$ correlation matrix, and the nuclide abundances are given by $\mathbf{N}(t)$, also of length m. The solution to Eq. 2.23 reproduces that of Eq. 2.22 and is algebraically computed using the eigenvalues and eigenvectors of $\mathbf{A}$ for an infinitesimal variation in time. This method has the benefit of allowing for nonzero IC for all nuclides in the chain and can be computed relatively quickly.

Both methods are incredibly useful and more complicated versions of the matrix exponential calculation are used in many reactor simulation software packages, including the Standardized Computer Analyses for Licensing Evaluation (SCALE) [145] suite, developed by Oak Ridge National Laboratory and described in App. B. To derive the analytical expression for the non-linear correction in Chp. 4, the neutron-capture and fission yield components will be required. This modification of the Bateman equation results in a slightly more intricate differential equation:

$$\frac{dN_{\alpha,i}}{dt} = \vec{Y}_{\alpha,i} \cdot \vec{\mathcal{F}} - (\lambda_{\alpha,i} + \phi_t \sigma_{\alpha,i}) N_{\alpha,i} + \lambda_{\alpha,i-1} N_{\alpha,i-1} + \phi_t \sigma_{\alpha-1,j} N_{\alpha-1,j} \tag{2.24}$$

where two indices are now applied for each nuclide, indicating the beta-decay chain by α and the daughter in the chain by i. To better illustrate this notation, two adjacent beta-decay chains in a reactor calculation are given in Fig. 2.4, where α corresponds to A or B, depending on the parent in the chain and i and j list the daughter in each respective chain from $i = 1, ..., m$ and $j = 1, ..., p$ where the chains do not need to be of equal length, but this case is presented as an introduction.

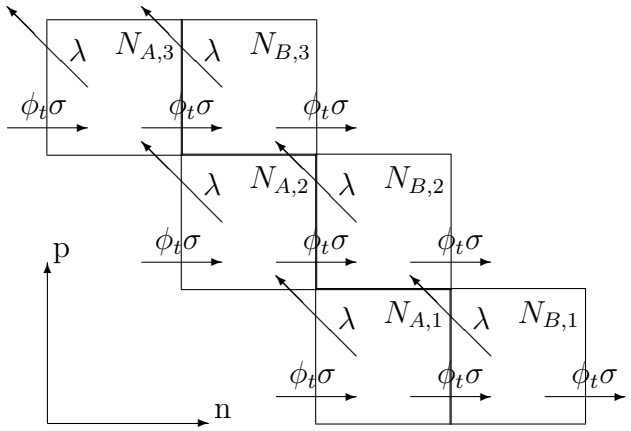

Figure 2.4: Example of two adjacent beta-decay chains separated by a single neutron-capture, both consisting of $m = p = 3$ nuclides in each chain. Displayed are the decay paths, denoted with λ, and the neutron-capture paths, denoted with $\phi_t\sigma$. Figure by author.

The generalized Bateman equation now involves the destruction of nuclide $N_{\alpha,i}$ via decays and neutron captures given by $(\lambda_{\alpha,i} + \phi_t\sigma_{\alpha,i})$, where ϕ_t is the thermal neutron flux and $\sigma_{\alpha,i}$ is the thermal neutron capture cross-section for $N_{\alpha,i}$. This can be further generalized to a multi-group equation, which bins the neutron energies and cross-sections, but is left simply as a thermal group expression for simplicity. The nuclide $N_{\alpha,i}$ can also be produced by decays of its beta-chain parent $\lambda_{\alpha,i-1}N_{\alpha,i-1}$ and via neutron captures from its isotope neighbor given by $\phi_t\sigma_{\alpha-1,j}N_{\alpha-1,j}$. Finally, a nuclide can be produced through fission, given by the dot-product of the fission yields vector $\vec{Y}_{\alpha,i}$ and the fission vector $\vec{\mathcal{F}}$, which we take to be a constant term. This assumption applies for steady-state nuclear reactors and adiabatic transitions. The steady-state reactor condition will lead to equilibrium values of each of the nuclides, which depends on the decay and neutron-capture rates. Most nuclides, due to their short half-lives, are in equilibrium within 10 d of irradiation.

What is expressed in Eq. 2.24 is effectively an additional dimension to the matrix exponential method, outlined by Eq. 2.23, where the neutron captures would represent a third dimension in matrix-space. This additional correlation makes the simplifications in Ref. [143] and Ref. [144] invalid and so more generalized solutions are required. At first glance this seems impossible. The expression for $N_{\beta,j}$ will undoubtedly depend on the solution for $N_{\beta-1,k}$ and this will depend on $N_{\beta-2,m}$ and so on for all $N_{\alpha,i}$ where $\alpha < \beta$. This recursive nature is handled naturally by the properties of the various nuclides produced in the fission fragment distribution. For example, suppose that nuclide $N_{A,1}$ decays rapidly such that $\lambda_{A,1} \gg \phi_t\sigma_{A,1}$, meaning that nuclide $N_{A,1}$ decays much more often than it captures a neutron. Then, the parent nuclide $N_{B,1}$ can be absolutely determined as its abundance only depends on the fission yields, see Eq. 2.24, as $\lambda_{B,0} = 0$, by defining $N_{B,1}$ as the parent, and $\sigma_{A,1} = 0$ via $\lambda_{A,1} \gg \phi_t\sigma_{A,1}$. It is with these types of nuclear parameter observations that one can make meaningful estimations using our generalized Bateman equation.

For now, the simplifying assumption is not necessary and one can solve the parent differential equation given by Eq. 2.24, noting that $\lambda_{\alpha,i-1} = 0$ as the parent does not receive any decays. To solve this differential equation a form for $N_{\alpha-1,j}$ must be assumed, which is taken to be

$$N_{\gamma,j} = \sum_{n=1}^{j} A_{\gamma,n} e^{-\tilde{\lambda}_{\gamma,n} t} + B_{\gamma,j} \tag{2.25}$$

accounting for the fact that the parent nuclides of each beta-decay chain do not need to be isotope neighbors, that is $i \neq j$. This assumed form of Eq. 2.25 is valid for **all** nuclides in a nuclear reactor that capture neutrons or decay, the combined effect being given by $\tilde{\lambda} = \lambda + \phi_t \sigma$, or what we call the effective decay constant. For stable nuclides, the well-known linear growth is acquired via a Taylor expansion. The coefficients $A_{\gamma,n}$ are composed of the fission yields, effective decay constants, and any initial nuclide concentrations. The constant term $B_{\gamma,j}$ represents the equilibrium term, so that as the irradiation time t approaches infinity the abundance of $N_{\gamma,j} \to B_{\gamma,j}$, where B_γ also depends on the effective decay constants, fission yields, and initial conditions.

In Eq. 2.25 all parents of $N_{\gamma,j}$ are accounted for with the summation of exponential decays $\exp[-\tilde{\lambda}_{\gamma,n} t]$, for a total of j effective decay constants. Using Eqn. 2.25 in the expression for the parent nuclide of Eq. 2.24 a solution for the nuclide abundance for any given parent can be derived through the method of undetermined coefficients, using the substitution of $\gamma \to \alpha - 1$. The derivation is explicitly given in App. C.

$$\begin{aligned} N_{\alpha,1}(t) = \left[N_{\alpha,1_0}\right] e^{-\tilde{\lambda}_{\alpha,1} t} &+ \left[\frac{\phi_t \sigma_{\alpha-1,j} B_{\alpha-1,j} + \vec{Z}_{\alpha,1} \cdot \vec{\mathcal{F}}}{\tilde{\lambda}_{\alpha,1}}\right] \left(1 - e^{-\tilde{\lambda}_{\alpha,1} t}\right) \\ &+ \left[\sum_{n=1}^{j} \frac{\phi_t \sigma_{\alpha-1,j} A_{\alpha-1,n}}{\tilde{\lambda}_{\alpha,1} - \tilde{\lambda}_{\alpha-1,n}} \left(e^{-\tilde{\lambda}_{\alpha-1,n} t} - e^{-\tilde{\lambda}_{\alpha,1} t}\right)\right] \end{aligned} \tag{2.26}$$

The end result now incorporates the initial nuclide abundance of $N_{\alpha,1}$, given by $N_{\alpha,1_0}$, and its cumulative fission yields $\vec{Z}_{\alpha,i}$ instead of the individual yields $\vec{Y}_{\alpha,i}$. The cumulative yields of a nuclide X are the sum of its individual yields and the individual yields of all beta-decay parents of X. Therefore, $\vec{Z}_{\alpha,i}$ represents the fission yields of $N_{\alpha,i}$ for 'infinite' irradiation time and is the sum of all individual yields that beta-decay to $N_{\alpha,i}$. It must be noted that the cumulative yields do not account for any neutron capture processes. A chain-parent can be constructed with the cumulative fission yields if all of its parents decay sufficiently quickly. For example, if all parents of X decay immediately, the beta-decay chain can simply begin with nuclide X accounting for any rapid decays to X via the use of cumulative instead of individual fission yields.

The two undetermined terms, $A_{\alpha-1,n}$ and $B_{\alpha,1}$ in Eq. 2.26, can be read from the solution of $N_{\alpha-1,j}$. In the case of $\lambda_{\alpha-1,j} \gg \phi_t \sigma_{\alpha-1,j}$, then $\sigma_{\alpha-1,j}/\lambda_{\alpha,1} \to 0$ and Eq. 2.26 can be determined without the knowledge of any other nuclide abundance. This will lead to the

simplification:

$$N_{\alpha,1}(t) = \left[N_{\alpha,1_0}\right]e^{-\tilde{\lambda}_{\alpha,1}t} + \left[\frac{\vec{Z}_{\alpha,1}\cdot\vec{\mathcal{F}}}{\tilde{\lambda}_{\alpha,1}}\right]\left(1 - e^{-\tilde{\lambda}_{\alpha,1}t}\right) \tag{2.27}$$

The full derivation of Eq. 2.26 is given in App. C, and the full justification for this simplification is given in Chp. 4.1.1.

Next, one can derive the solution to any subsequent daughter nuclide $N_{\alpha,i}$ of the parent $N_{\alpha,1}$. This is given by the differential equation in Eq. 2.24, but now no suppression of $\lambda_{\alpha,i-1}$ nor $\sigma_{\alpha-1,i}$ can be assumed. Taking Eq. 2.25 for the form of both the beta-decay parent $N_{\alpha,i-1}$ and the neutron capture parent $N_{\alpha-1,j}$ leads to the following solution:

$$\begin{aligned} N_{\alpha,i}(t) =& \left[N_{\alpha,i_0}\right]e^{-\tilde{\lambda}_{\alpha,i}t} + \left[\frac{\phi_t\sigma_{\alpha-1,j}B_{\alpha-1,j} + \lambda_{\alpha,i-1}D_{\alpha,i-1} + \vec{Y}_{\alpha,i}\cdot\vec{\mathcal{F}}}{\tilde{\lambda}_{\alpha,i}}\right]\left(1 - e^{-\tilde{\lambda}_{\alpha,i}t}\right) \\ &+ \left[\sum_{n=1}^{j}\frac{\phi_t\sigma_{\alpha-1,j}A_{\alpha-1,n}}{\tilde{\lambda}_{\alpha,i} - \tilde{\lambda}_{\alpha-1,n}}\left(e^{-\tilde{\lambda}_{\alpha-1,n}t} - e^{-\tilde{\lambda}_{\alpha,i}t}\right)\right] + \left[\sum_{n=1}^{i-1}\frac{\lambda_{\alpha,i-1}C_{\alpha,n}}{\tilde{\lambda}_{\alpha,i} - \tilde{\lambda}_{\alpha,n}}\left(e^{-\tilde{\lambda}_{\alpha,n}t} - e^{-\tilde{\lambda}_{\alpha,i}t}\right)\right] \end{aligned} \tag{2.28}$$

where there are now two sets of undetermined coefficients: one for the neutron capture parent, $A_{\alpha-1,n}$ and $B_{\alpha-1,j}$, and one for the beta-decay parent, $C_{\alpha,n}$ and $D_{\alpha,i-1}$, which can both be read off from the equations for $N_{\alpha-1,j}$ and $N_{\alpha,i-1}$ when expressed in the form of Eq. 2.25. The expression for any subsequent daughter reveals a new equilibrium term (the 2$^{\text{nd}}$ term), with an added dependence on the parent effective decay constant, and a new production term from the neutron-capture parent (the 3$^{\text{rd}}$ term) and beta-decay parent (the 4$^{\text{th}}$ term). Again, note that Eq. 2.28 has a dependence on the individual fission yields $\vec{Y}_{\alpha,i}$ instead of the cumulative yields, which can only be used in the parent form.

Finally, a solution can be found for the stable daughter nuclide at the end of a beta-decay chain $N_{\alpha,N}$ by solving Eq. 2.24 with the assumption that $\lambda_{\alpha,N} = 0$. Note that we still allow for the option of neutron captures on $N_{\alpha,N}$, making the 'stable' daughter only pseudo-stable at high thermal fluxes. This solution is given by:

$$\begin{aligned} N_{\alpha,N}(t) =& \left[N_{\alpha,N_0}\right]e^{-\phi_t\sigma_{\alpha,N}t} + \left[\frac{\phi_t\sigma_{\alpha-1,j}B_{\alpha-1,j} + \lambda_{\alpha,N-1}D_{\alpha,N-1} + \vec{Y}_{\alpha,N}\cdot\vec{\mathcal{F}}}{\phi_t\sigma_{\alpha,N}}\right]\left(1 - e^{-\phi_t\sigma_{\alpha,N}t}\right) \\ &+ \left[\sum_{n=1}^{j}\frac{\phi_t\sigma_{\alpha-1,j}A_{\alpha-1,n}}{\phi_t\sigma_{\alpha,N} - \tilde{\lambda}_{\alpha-1,n}}\left(e^{-\tilde{\lambda}_{\alpha-1,n}t} - e^{-\phi_t\sigma_{\alpha,N}t}\right)\right] + \left[\sum_{n=1}^{N-1}\frac{\lambda_{\alpha,N-1}C_{\alpha,n}}{\phi_t\sigma_{\alpha,N} - \tilde{\lambda}_{\alpha,j}}\left(e^{-\tilde{\lambda}_{\alpha,n}t} - e^{-\phi_t\sigma_{\alpha,N}t}\right)\right] \end{aligned} \tag{2.29}$$

where this expression can be solved for trivially by setting $\tilde{\lambda}_{\alpha,i} = \phi_t\sigma_{\alpha,i}$ and $i = N$ in Eq. 2.28 as there are no decays from the nuclide $N_{\alpha,N}$, meaning $\lambda_{\alpha,N} = 0$. Again, the method of undetermined coefficients is used, with $A_{\alpha-1,n}$ and $B_{\alpha-1,j}$ for the neutron capture parent and $C_{\alpha,n}$ and $D_{\alpha,N-1}$ for the beta-decay parent. A Taylor expansion of $\exp[-\phi_t\sigma_{\alpha,N}t]$ will

yield the expected linear relation between $N_{\alpha,N}$ and t in the second term when $\phi_t \sigma_{\alpha,N} t \ll 1$, as is often the case for true irradiation scenarios and typical nuclides.

The combination of Eqs. 2.26 - 2.29 will yield expressions for any given beta-decay chain and neutron capture chain. As mentioned before, with arbitrary choices for $\sigma_{\alpha,i}$, ϕ_t, $\vec{Y}_{\alpha,i}$, $\vec{Z}_{\alpha,i}$, and $\lambda_{\alpha,i}$ it seems impossible to know all undetermined coefficients and, thus, solve the decay equations. For this formulation to have any mathematical power, beta-decay chains must be chosen wisely, such that proper simplifications can be made. For this reason, it is necessary to check the cross-sections, decay constants, and fission yields that are found in the Evaluated Nuclear Structure Data File (ENSDF) [146], ENDF [127], and JEFF [125] (to name a few) libraries. Once an analytical expression is available for the nuclide abundances given by Eqs. 2.26 - 2.29, it can be trivially manipulated to determine the nuclide activity $\alpha(t)$ through $\alpha_{\alpha,i}(t) = \lambda_{\alpha,i} N_{\alpha,i}(t)$. Once an activity is determined, it can be multiplied to an antineutrino spectrum normalized to one decay. The normalized antineutrino spectra are found by converting beta spectrum according to Chp. 2.2.1, as done in Ref. [128]. This process and these expressions will be used explicitly to derive the non-linear effect, as described in Chp. 4. The spent fuel contribution and antineutrino monitoring limits will use the SCALE simulation suite, which applies a complex matrix exponential solution, beyond the simplification found in Ref. [144].

The antineutrino source has now been described extensively, as both a summation of weighted individual fissile antineutrino yields (the ILL measurements combined with a knowledge of the fission vector $\vec{\mathcal{F}}$ in Chp. 2.2.1) as well as the specific nuclide-by-nuclide formulation of decay equations (solving the generalized Bateman equations in Chp. 2.2.2). Once the antineutrino flux of the reactor source is known, it can be propagated via the oscillation probabilities of Chp. 2.1 to a detector location. The detection mechanism is described next.

2.3 Neutrino Detection

Detection of neutrinos was an enormous experimental task, evidenced by the great efforts Cowan and Reines took to first measure the particle [12]. A combination of effects results in this fact, but notable reasons are the extremely small interaction cross-section of $\mathcal{O}(10^{-42})\,\mathrm{cm}^2$, the need to reduce background signals, and the distance from the source. For this work, the focus is on reactor antineutrinos, thus limiting the neutrinos to the energy region of $0 \leq E_\nu \lesssim 10\,\mathrm{MeV}$, as the majority of beta-decays from the fission fragments discussed in Chp. 2.2 have endpoints below 10 MeV. In addition, reactor experiments have the benefit of a precise knowledge of the source location, allowing one to place a detector at the desired distance (except in the case of extremely short baseline experiments, where the reactor containment vessel provides a boundary). The original method of detection used by Cowan and Reines is still utilized by most reactor antineutrino experiments. This process is inverse beta-decay (IBD) and will be the primary detection mechanism studied. This

interaction is given by:

$$\bar{\nu}_e + \mathrm{p} \rightarrow \mathrm{n} + e^+ \tag{2.30}$$

where an electron antineutrino ($\bar{\nu}_e$) incident on a free proton (p) produces a neutron (n) and a positron (e^+). This reaction of Eq. 2.30 requires a minimum energy of $E_{\text{thresh}} = 1.8\,\text{MeV}$ to occur. This threshold energy can be easily derived from the difference in rest energy between the neutron positron pair and the proton ($E_{\text{thresh}} = E_n + E_{e^+} - E_p$). Therefore, our true energy region of interest is $\sim 1.8\,\text{MeV} \leq E_\nu \leq 10\,\text{MeV}$, where the cross-section for the IBD reaction varies between $0 \leq \sigma_{\nu p} \lesssim 7 \times 10^{-42}\,\text{cm}^2$ [147] for these neutrino energies.

There are indeed alternative methods to detect neutrinos besides IBD, which can be summarized into two concepts: light collection from neutrino interactions (which IBD falls under) and radioactive counting from neutrino interactions. Light collection methods include the IBD capture of Eq. 2.30, but also the collection of Cherenkov light from ionizing particles. When high energy neutrinos interact in a detector via electron scattering ($e\nu \rightarrow e\nu$), either through CC or NC interactions, highly relativistic electrons can result. Cherenkov light is produced when the relativistic electron travels in a medium where the particle velocity exceeds that of light in said medium [148, 149]. When this occurs, a charged particle will emit photons in a conical wave following the relation $\cos\theta = 1/(\beta n)$, where θ is the opening angle of the light cone, $\beta = v_p/c$ is the particle velocity relative to that of light, and n is the refractive index of the medium. Through this expression, one can derive particle velocities from opening angles in Cherenkov rings, as done in the Super-Kamiokande detector [37]. Additional experiments, such as IceCube [150], SNO [151], and IMB (Irvine-Michigan-Brookhaven) [152] have all utilized water (or heavy water in the case of SNO) Cherenkov detectors.

Radioactive counting methods involve the exposure of a detector material to a neutrino flux for a known amount of time. Neutrinos can capture on a nuclei present in the detector volume, via $\nu + X \rightarrow Y + e^-$, where Y is a long-lived nuclide. The detector material is then chemically separated to count the number of radioisotopes Y that have been produced. This technique has the benefit of lowering the interaction threshold significantly, depending on the capture nucleus. The famous Homestake experiment [10] used radiochemical separation of Argon from a Chlorine-based detector. Solar neutrinos incident could react via $\nu_e + {}^{37}\text{Cl} \rightarrow e^- + {}^{37}\text{Ar}$, thus providing a measure of the solar neutrino flux based on the exposure time and amount of ${}^{37}\text{Ar}$ extracted. There are other radioactive counting detectors in use today, such as the GALLEX [153] and SAGE [42] experiments using the $\nu_e + {}^{71}\text{Ga} \rightarrow e^- + {}^{71}\text{Ge}$ reaction. However, radioactive counting methods have the distinct disadvantage that neutrinos are not detected in real time, and without energy information, unlike light collection methods. Therefore, light collection, specifically scintillation light, will be the detection method of choice, but it is recognized that radioactive counting methods are still used today.

The second method of light collection is via scintillator, which predominantly uses the IBD reaction and the critical prompt-delayed coincidence. The production of two particles in IBD allows for a large amount of background rejection, shown next. The primary particle,

the positron, will almost immediately find a corresponding electron in the detector mass and annihilate, producing two 0.511 MeV gammas in opposite directions, the prompt signal. The secondary particle, the neutron, will undergo several collisions with the detector matter until it thermalizes and captures on some nucleus. The efficiency of neutron capture will depend on the capture agent in the detector. A capture agent is typically chosen for its high cross-section and a signature emission energy, which is released often in the form of gamma rays as the excited neutron capture state transitions to its ground state (i.e. $n + {}^{A}X \rightarrow {}^{A+1}X^{*} \rightarrow {}^{A+1}X + \gamma$), the delayed signal. This entire two-part detection can be set up in a scintillating medium to maximize the light output eventually read by photomultiplier (PMT) tubes or some other light gathering device. In the example of the Cowan and Reines experiment, Cadmium was used as the capture agent undergoing $\mathrm{n} + {}^{108}\mathrm{Cd} \rightarrow {}^{109}\mathrm{Cd}^{*} \rightarrow {}^{109}\mathrm{Cd} + \gamma$ with a delayed coincidence window of $\sim 5\,\mu$s after the initial prompt positron annihilation.

In the following section the capture mechanism for IBD in a doped scintillator is discussed in detail, illustrating the delayed coincidence signal and discussing the background sources for reactor experiments as well as methods for reducing these backgrounds. Prompt-delayed coincidence will play an integral role in this reduction.

2.3.1 Prompt-Delayed Coincidence

The crux of neutrino detection falls upon the use of the prompt-delayed coincidence timing between the positron and neutron tags. In the presence of a scintillating material, the neutrino energy can be extracted from the prompt energy seen by the positron deceleration and annihilation. The visible energy detected (E_{vis}) is given by the kinetic energy of the positron (E_e) and the two annihilation gammas, $E_{\mathrm{vis}} = E_e + 2 \times 0.511\,\mathrm{MeV}$, where $c = 1$ and the visible and positron energy are given in MeV. The neutrino energy can be expressed in terms of the positron energy via energy conservation of Eq. 2.30, resulting in $E_\nu = E_p + 1.8\,\mathrm{MeV}$, where 1.8 MeV is used as E_{thresh}. Together, this forms a relation between the visible energy in the detector and the neutrino energy:

$$E_\nu = E_{\mathrm{vis}} + 0.78\,\mathrm{MeV} \tag{2.31}$$

The recoil energy of the neutron can also be incorporated, but this factor is incredibly small by comparison and typically quoted at $\sim 10\,\mathrm{keV}$ [53]. Through the relation of Eq. 2.31, the prompt positron acts as the portion of the signal that is sensitive to the neutrino energy.

While the use of scintillator in a detection mass boosts the efficiency of extracting the full neutrino energy, it will also give rise to additional background signals as any ionizing source can produce scintillation light within the detector. These background sources, which will be covered next, can mimic the energy deposition of a single positron quite easily. Therefore, it is necessary to utilize the secondary particle, the neutron, with a timing and/or spatial coincidence. The secondary particle signal typically comes in the form of a neutron capture on an agent mixed with or in close proximity to the scintillator material. A timing and

spatial coincidence can be solved for by determining the mean free path for neutrons in the detector medium, $\lambda = 1/\Sigma$, where Σ is the macroscopic cross-section ($\Sigma = \sigma N$ with σ the microscopic cross-section and N the particle density) of the material the neutron is traveling through. The value of λ represents an average distance between collisions. Knowing the fractional energy loss of a neutron with each collision allows one to set a limit on the distance the neutron can travel and, thus, the time it will take a neutron to thermalize and capture. Typical coincidence windows depend on the medium, but are $\sim 200\mu$s for Hydrogen-dominated media and $\sim 30\mu$s for the common capture agent Gadolinium [154]. Known gamma energy depositions are $\sim 8\,\text{MeV}$ for neutron captures on Gd and $\sim 2.2\,\text{MeV}$ for neutron captures on H [155]. Precise windows must be calculated based on both the detector design and the expected background rates.

The entire prompt-delayed coincidence for a typical IBD event in an organic scintillator minimally doped with some neutron capture agent will appear as follows. A prompt positron deposits its energy via scintillation and e^+e^- annihilation releasing E_{vis} energy. Then, within a specific timing window, the neutron captures on the agent to an excited state, which releases gammas with a known total energy. The combination of these signals within the timing window signals a neutrino IBD interaction. Energy windows can also be applied as the antineutrino energies from reactors are $\lesssim 10\,\text{MeV}$, thus limiting the prompt positron energy, and the gamma release from the neutron capture agent will have a known total energy. Signal pairs not satisfying the timing and energy windows can then be removed from the data.

2.3.2 Possible Backgrounds

The prompt-delayed signal discussed previously is used to remove possible backgrounds from a dataset. The use of a scintillator indicates that any ionizing particle traveling through the medium will stimulate some scintillation light, potentially mimicking the positron signal. The ionizing particle could be the result of a cosmic particle interaction in the atmosphere or detector material, a radioactive decay in some detector material, gammas from neutron capture nuclides, or positrons from IBD, to name the most common sources.

Cosmic sources of backgrounds are typically lowered by supplying detectors with large overburdens of material to attenuate high energy particles. Muons are the most prevalent of these cosmic sources, providing neutrons via spallation, as suggested by Li and Beacom [156], mimicking the delayed signal or by creating radioactive nuclides, such as ^{9}Li or ^{8}He. These radionuclides can decay via β-n emission, which will emulate the entire prompt-delayed signal for detectors without electron-positron differentiation. For this reason, muon rate estimates are of particular interest to neutrino experiments [157]. Neutrons can also be produced via nearby calibration sources such as ^{252}Cf or ^{241}Am.

Radioactive decay backgrounds can be limited by using materials with low radioactivity levels. Common radioactivity sources are the glass in the PMTs, uranium and thorium

in metals used in the PMT fixtures and the detector itself, as well as natural radioactive backgrounds from the surrounding rock, also via uranium and thorium. Another method of reducing this background rate is the use of an optically separated detector region or water buffer. Then, an inner fiducial detector volume can be established with additional water shielding protecting it from external gammas. Most major liquid scintillator detectors at reactor sites have utilized this buffer region technique [47, 158, 159].

Gamma production from neutron capture sources can provide both the delayed signal as well as backgrounds. These non-IBD gamma sources can be shielded in the same manner that radioactive backgrounds are, via a buffer region. Specific neutron captures can be isolated via the timing window discussed previously, as the mean free paths will be different for different materials, or via the different energy produced in the de-excitation. A specific example of this analysis is the separation of Gd captures and H captures in an organic doped liquid scintillator at Daya Bay [160]. Stray neutrons without correlated positrons can be produced via spallation and, thus, must be estimated via muon rates as well.

Together, these sources of backgrounds can produce high event rates. If two background events randomly satisfy both the energy and timing criteria, it is categorized as an accidental background. Accidentals comprise a large percentage of the total background rate, but can be estimated via knowledge of the singles rates that imitate the prompt and delayed signals in a relatively straightforward manner (e.g. Ref. [161]). Apart from recent experimental efforts at surface-deployed neutrino detectors [71,162,163], most previous neutrino experiments have lowered cosmic-induced backgrounds through the use of deep underground deployment.

An additional method of background reduction is accomplished through pulse shape discrimination. This concept utilizes the different rise and decay-times as well as the pulse widths attributed to different ionizing particles in a scintillator; an example being that pulse integrations can be analyzed to separate long-tail pulses (neutron-like) from rapidly-decaying ones (gammas) with their different differential energy depositions dE/dx. This was first demonstrated to separate gammas and neutrons [164], but pulse shape discrimination has been applied to the solar neutrino experiment Borexino [165] and has exhibited promising results in reducing the backgrounds of neutrino experiments even at the surface [166]. In addition, electronic and neutronic-based recoil separation in liquid Argon has been demonstrated with high efficiency [167].

By placing timing and energy cuts on a dataset, one will naturally remove actual IBD events through these background criteria. This concept is reflected in the overall efficiency of a detector, which is commonly separated into its constituents to identify the specific cuts being utilized. For now, the complex analysis of data and the use of timing and energy cuts for a prompt-delayed sequence of IBD in a doped liquid scintillator is simplified as an overall detector efficiency ϵ_d.

2.3.3 Rate Calculation

Once the efficiency of a detector, given by ϵ_d, has been experimentally determined, the expected number of antineutrino events in a detector mass can be solved for. Nuclear reactors are an isotropic source of antineutrinos with a given flux $\Psi(E)$, which falls off with the $1/r^2$-law governed by the solid angle subtended by the detector. Thus, the antineutrino flux incident on a detector at a distance L from the source is given by $\Psi(E)/(4\pi L^2)$. Assuming an organic scintillator, meaning that the antineutrino interactions occur on free protons given by the νp cross-section $\sigma(E)$, we can express the antineutrino interaction rate simply as $\Psi(E)N_T\sigma(E)/(4\pi L^2)$, for N_T target protons. We note that both the antineutrino flux and the νp cross-section have an energy dependence. Then, the product of the reaction rate $\Psi(E)N_T\sigma(E)/(4\pi L^2)$ with the oscillation probability $P(E, L)$ and detection efficiency ϵ_d must be multiplied and integrated over in order to obtain the total event rate in any given energy range. The oscillation, as discussed in Chp. 2.1, has an explicit dependence on the neutrino energy and baseline between the source and detector. In total, the event rate is given by

$$R_i = \int_{E_i-\Delta E}^{E_i+\Delta E} \left[\frac{\Psi(E)\sigma(E)N_T P(E, L)}{4\pi L^2} \epsilon_d \right] dE \tag{2.32}$$

Combining the knowledge of this chapter results in the event rate R_i in an energy bin with central energy E_i and bin width ΔE. This is expressed in terms of the antineutrino flux $\Psi(E)$ according to source described in Chp. 2.2, the νp cross-section according to Ref. [147], the number of targets N_T or protons in the detector, the energy and baseline-dependent oscillation probability $\mathcal{P}(E, L)$ according to Chp. 2.1, the baseline itself L, and the detection efficiency ϵ_d outlined in Chp. 2.3. A total integration over all energy bins will yield the rate of νp events from a given source and an analysis of the events in each energy bin can be used determine the spectral shape of the antineutrino flux.

For time-dependent signals, a time integration can be incorporated into Eq. 2.32 as well, but for now it is simply assumed that the reactor antineutrino source is stable. This assumption applies nicely to most reactors in power equilibrium and thus, Eq. 2.32 can be simply written as $N_i = \int_{t_0}^{t_f} R_i dt$ for the total even rate over a detection time $t_f - t_0$. Equation 2.32 will be applied in a time-dependent and time-independent manner in order to estimate the corrections stemming from spent nuclear fuel in Chp. 3 and the non-linear nuclides in Chp. 4.

Chapter 3

Spent Fuel Correction

This chapter focuses on the correction to the antineutrino spectrum from nuclear reactors that originates from the spent nuclear waste near the corresponding reactor. In this chapter the origin of the spent nuclear fuel (SNF) signal in reactor experiments is introduced. After discussing its origins, the impact of the spent nuclear fuel signal on the total reactor spectrum, as observed by some reactor antineutrino experiment, is identified and quantified. Our method of determining some characteristics and properties of the SNF neutrinos are detailed, followed by a calculation of the sensitivity of antineutrino experiments to detect the corrective signal. A first-time measurement would aid in the effort to lower uncertainties for future short-baseline experiments. Our calculations will rely heavily on the Standardized Computer Analyses for Licensing Evaluation (SCALE) suite [145], a software package developed by Oak Ridge National Lab in an effort to simulate burnup and depletion calculations for new and existing reactor designs. A brief summary of the SCALE simulation is given in App. B.

The preliminary results of this research was used to estimate the spent nuclear fuel contribution in Tab.III of Ref. [2]. The preliminary analysis is scaled up to a full experimental setup, namely the Daya Bay oscillation experiment.

3.1 Spent Nuclear Fuel Introduction

Spent nuclear fuel (SNF) results from the refuelings that all nuclear reactors experience. While the time-scales of the irradiation cycle length may vary heavily with the specific reactor, the fact that it will replace some of its fuel source is constant and necessary for both functionality and efficiency. This is because irradiation will slowly replace the fission source with the fragments, reducing k_{eff}. In addition, the burnup process, as described in Chp. 2.2.1, will alter the fuel composition where uranium isotopes are burned and transmuted

into plutonium isotopes. Burnup, the unit defined loosely as average specific reactor power[1] multiplied by irradiation time ($BU = \langle \mathcal{P} \rangle T$) indicates the age of the fuel. For fuel with a large enough burnup, the reactivity will be too low to maintain fission, as the uranium and plutonium nuclides have been replaced with fission fragments. To reestablish the original core productivity, fresh fuel must be substituted for high BU irradiated fuel. Reactor fuel is segmented into fuel assemblies, most commercial power reactors containing ~ 150 assemblies. Each fuel assembly holds control rods, to regulate k_{eff}, and fuel pins, which contain the actual fissile material.

A refueling will often involve the shuffling of fuel assemblies inside a reactor in order to counter unevenly fissioned fuel due to the inhomogeneous neutron flux in the core. To maintain a more homogeneous fission density and decrease the number of lost neutrons, fuel assemblies are moved around in the core and replenished such that higher burnup fuel assemblies are centrally located and lower burnup fuel assemblies are closer to the edge. A combination of shuffling and refueling of fuel allows reactors to burn the same fuel to larger burnup values yielding a more efficient use of the uranium and plutonium.

Reactors are often run as multi-batch cores, which increases the available burnup of the fuel and decreases the reactivity swing for a cycle, one cycle being the time in between refuelings. Reactivity is a measure of the departure from criticality and is defined as $\rho(t) = (k(t) - 1)/k(t)$, using the time-dependent multiplicities $k(t)$, meaning that for a cycle of length T, the reactivity swing is $\Delta\rho = |\rho(T) - \rho(0)|$; larger $\Delta\rho/T$ indicating a less-adiabatic core. Increasing the maximum BU allows for longer irradiation cycles, which produces less reactor-off time. Decreasing the reactivity swing produces a more stable core. For an N-batch core, the core is divided into N segments, where each refueling will replace $1/N^{\text{th}}$ of the total fuel. This indicates that a $2N$-batch core will have to refuel twice as frequent as an N-batch core for the same BU. As refueling shutdowns will often shuffle all fuel assemblies, the off-time for a reactor shutdown is relatively independent of the batch size, so large N does not necessarily indicate short shutdowns. Calculation and reactor experience has shown that a 3(4)-batch core maximizes BU for the fuel, while minimizing the shutdown time for pressurized(boiling) water reactors. These concepts: refueling procedure, multi-batch cores, and reactivity can all be found in common Nuclear Engineering textbooks [123, 168].

The specific SNF example studied here will focus on pressurized water reactors (PWRs), so we will proceed with the 3-batch core assumption. With each shutdown, approximately one-third of the core is replaced with fresh fuel. The third that is removed is said to be at its end of cycle (EOC). This EOC batch is still thermally and radioactively hot due to long-lived radionuclide decays. This 'decay heat', as it is named, continues even at cooling times approaching 1 yr [169]. A SNF batch will then need to be stored in a nearby location after unloading from the core as it is too hot for transit. These onsite storage pools are typically located within 40 m of the reactor. The SNF will be stored in the spent fuel ponds anywhere from $3 - 10$ years as it cools, thermally and radioactively. After this time period,

[1] "Specific" indicates power divided by core mass

the spent fuel can be safely transferred into dry cask storage, usually offsite.

3.1.1 Spent Nuclear Fuel Composition

With time-scales of several years, only a few radioactive fission fragment nuclides from irradiation will be left in the SNF. For the typical use of IBD in reactor antineutrino experiments, see Chp. 2.3, only long-lived fragments that have a β-decay endpoint above $\sim 1.8\,\mathrm{MeV}$ will appear in the detectors; these are ^{90}Sr, ^{106}Ru, and ^{144}Ce each with a halflife of $\sim 28\,\mathrm{yr}$, 371 d, and 284 d, respectively. Note that neither ^{90}Sr, ^{106}Ru, nor ^{144}Ce satisfy this endpoint requirement, but their short-lived daughters, ^{90}Y, ^{106}Rh, and ^{144}Pr, all do. Thus, the SNF neutrino signal is comprised of these so-called 'roadblock' nuclide chains. Roadblock chains are formed when a long-lived nuclide decays into a short-lived one. The result is a non-negligible neutrino source with the endpoint of a short-lived nuclide and the decay time of a long-lived one.

The roadblock chains of ^{90}Sr, ^{106}Ru, and ^{144}Ce present in SNF provide a long-lasting neutrino source through the beta decays of their respective daughters. The strength of this signal will be proportional to the amount of SNF, typically by the number of batches, or loads, removed. This is generally proprietary information known by the power plant and regulatory commissions. Therefore, one must assume that the number of SNF loads in any given spent fuel pond is a free parameter. In addition, as the spent fuel ponds are near the reactor core itself, the baselines for SNF oscillation will be comparable to those from the actual reactor. Finally, this type of background is a true antineutrino signal, in that it will appear in an antineutrino detector as an IBD event and not as any of the backgrounds discussed in Chp. 2.3.2 making it impossible to remove these events without some removal of the true reactor signal. This scenario leads to the conclusion that the SNF signal must be quantified or else it remains an unknown, pure antineutrino background for all reactor antineutrino experiments. This background is critical to sterile neutrino searches at reactors, both current [170] and proposed [71, 73, 171], the significance of the reactor antineutrino anomaly [81], and geoneutrino searches via reactor subtraction [172, 173]. The following method is used to calculate the SNF correction.

3.1.2 Spent Nuclear Fuel Antineutrino Calculation

Using the Standardized Computer Analyses for Licensing Evaluation (SCALE) suite [145] one can compute the depletion composition of reactor fuel with a given reactor design, irradiation history, and fuel data. A brief description of SCALE is provided in App. B. We use the Origen-S subroutine of SCALE, which is a deterministic depletion calculation that simplifies the complex reactor environment as a zero-dimensional object using appropriately weighted cross-section libraries. Some of these libraries come pre-packaged with the SCALE suite, including libraries for most commercial power reactor designs, both PWR and BWR.

With Origen-S and publicly accessible reactor data, the composition of the SNF at a typical PWR is estimated. Combining the composition calculation via SCALE with the neutrino spectra of Ref. [128] a total SNF antineutrino signal is determined, which is then compared with a running reactor PWR signal.

Origen-S is capable of producing a variety of outputs for the user, but the irradiation and decay-period nuclide abundance output, which prints the amount of each nuclide in the simulation at all time steps provided, is the crux of this analysis. For this type of output, reactor design specifications are needed, such as the fuel assembly array (geometrical and material layout of the fuel), irradiation history (power and length), shutdown history (length), the initial fuel composition (nuclides and abundances), and the moderator density. For the PWRs in question, we refer to the Operating Experience in Member States (OPEX) [174] reports issued by the International Atomic Energy Agency (IAEA) [175] every year. The OPEX reports list technical data on all commercial reactors subject to IAEA safeguards and the power history for that calendar year. Six specific PWRs are isolated for the SNF calculation. They are located in the Guangdong province in China and are known as the Daya Bay and Ling Ao reactors. These six reactors comprise the experimental backbone of the Daya Bay neutrino oscillation experiment [161]. All six reactors are based on the French Framatome (now Areva) M310 three-cooling loop reactors; the Daya Bay and Ling Ao I cores are the CPY designs and the Ling Ao II cores are inspired by the new CPR-1000 design. All use a square 17×17 AFA 3G fuel assembly design, which is similar in structure and performance to the Westinghouse 17×17 array below:

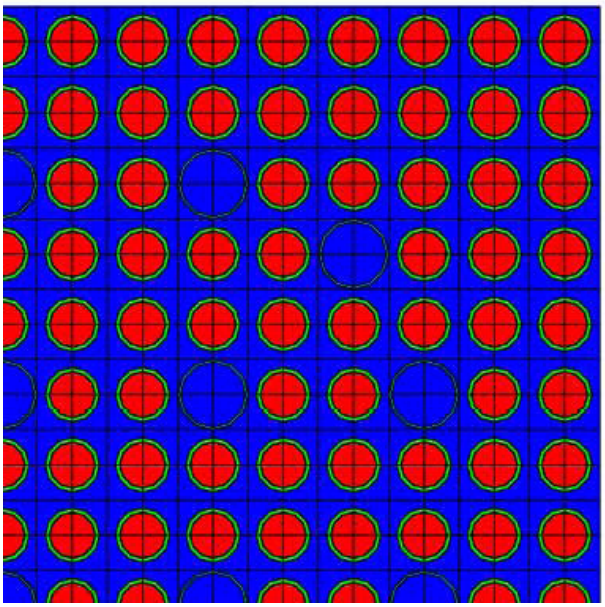

Figure 3.1: One quarter of a Westinghouse 17×17 fuel assembly (FA). The fuel rods (red) have a 1.26 cm pitch, or distance between rods, and are surrounded by an air gap (yellow) and Zircaloy-4 cladding (green). The moderator is H_2O (blue) and several guide tubes can be seen (cyan). The guide tubes are used to hold the FA and insert control rods to change the reactivity. Simulation often utilizes FA and reactor symmetry to speed up computation. Figure courtesy of SCALE [145].

Origen-S allows the user to define the specific composition of the fuel in Fig. 3.1 as well as the moderator density. For the Westinghouse 17×17 array, SCALE contains a pre-calculated cross-section library, which we use in place of the exact Daya Bay assembly, as the difference is negligible. From the OPEX sheets, the enrichment (weight percentage of ^{235}U in the uranium fuel) used by the Daya Bay cores is 3.7% and the Ling Ao I cores is 4.45%. As of the 2013 OPEX publication, the Ling Ao II cores do not list their enrichments, so the assumption is made that they will be similar to their Ling Ao I predecessors. All six reactors have the same fuel capacity of 72.4 metric tonnes of uranium (MTU). The moderator densities are assumed to be $0.723\,\mathrm{g/cm^3}$, as given by the Westinghouse FA.

Now that the reactor specifications, including the fuel and moderator compositions, are known the last input needed is the irradiation history. OPEX sheets provide this information in the following style: where the second, third, and fifth columns are provided in the OPEX sheets and the fourth and sixth columns are the calculated parameters to be used as input for Origen-S. To convert from the net power generated and operation factor, we use:

$$\mathcal{P}_t = \frac{1000 P_e^{net}}{O \cdot T_m \cdot L} \cdot \frac{1}{\epsilon} \tag{3.1}$$

where the net electrical power generation P_e^{net} for each month (in Gigawatt hours) is con-

Month	GW(e).h	OF%	Monthly Power [MW]	History	MW(t)/MTU
Jan.	706.80	100.00	950.000	(I-42.15d)	121.913
Feb.	243.50	39.90	908.148	(D-19.7d)	116.542
Mar.	580.60	90.90	858.500		110.171
Apr.	685.50	100.00	952.083		122.180
May	691.70	100.00	929.704		119.308
Jun.	680.10	100.00	944.583		121.218
Jul.	698.40	100.00	938.710		120.464
Aug.	695.70	100.00	935.081	(I-328.325d)	119.998
Sep.	663.10	100.00	920.792		118.188
Oct.	684.70	100.00	920.295		118.101
Nov.	681.90	100.00	947.083		121.538
Dec.	702.70	100.00	944.489		121.205

Table 3.1: Ling Ao I OPEX spreadsheet information for the 2010 calendar year [174]. Each month, the net power generated in electric Gigawatt hours (GW(e).h) is given with the operation factor (OF), the ratio of on-line hours to reference period hours. The OPEX sheet also provides a comments section listing outage durations and dates. The monthly thermal power (in MW) and specific thermal power (MW(t)/MTU) can be easily calculated from the net power and operation factor (see text).

verted to a monthly power by multiplying by a factor of 1000 and dividing by the hours of operation $O \cdot T_m$ (operator factor multiplied by hours in each month). The monthly power is converted from electric power to thermal power by considering the thermal efficiency ϵ of the reactor, a ratio of net design reactor capacity to the thermal capacity. This information is available via the Power Reactor Information System (PRIS) [176] provided by the IAEA. Typical efficiencies for PWRs are $\sim 30\%$; for the reactors used in Daya Bay they are 32.3%, 32.5%, and 34.4% for the Daya Bay, Ling Ao I, and Ling Ao II cores, respectively. Finally, the specific thermal monthly power, the input for Origen-S, is calculated by dividing the monthly thermal power by the fuel load (L): 72.4 MTU for all cores.

During the time of the SNF analysis, much of the information on Ling Ao II was unavailable, so Ling Ao I and Ling Ao II cores were assumed to be functionally identical. In reality, the efficiency is slightly better for the Ling Ao II cores, thus the thermal powers will be slightly larger. The irradiation cycles are equivalent, however, which means the burnup at EOC is still very similar between Ling Ao I and Ling Ao II cores. As the final burnup at EOC is the dominating factor in the SNF composition, the overall effect of treating Ling Ao II as an identical copy of Ling Ao I is very minimal.

All the information necessary for an Origen-S calculation is now available: the reactor specifications and the irradiation specific thermal powers and times all coming from the publicly

accessible OPEX sheets. Origen-S divides the computation into irradiation and decay calculations, which can be stitched together to form a set of reactor cycles. There are only a few occasions when the commented outage time disagrees with the reported operation factor; in these instances the listed outage time was retained instead of attempting to match the annual offtime. The exact time of a shutdown is often not listed, so the decay periods used can vary by as much as 48 hr. For situations when a SCRAM, an unexpected shutdown, is listed and there is no accompanying date, the total offtime listed was used to determine the length of the SCRAM. The location of the SCRAM during the month was placed so that the adjacent irradiation periods would split the remainder of the month the SCRAM was issued for.

Using the two rightmost columns of Tab. 3.1 and the OPEX sheets for the other 3 reactors (Daya Bay I and II and Ling Ao II), which span from 2005-2013 (data from 2005-2011 was used), the typical power histories of the Daya Bay and Ling Ao (both I and II) cores can be computed. Graphically, these are given as Fig. 3.2 below:

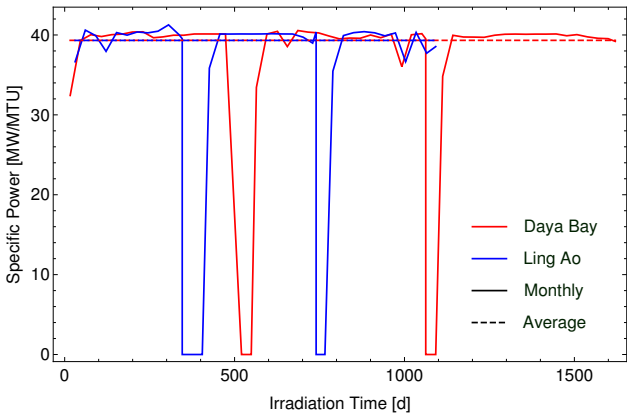

Figure 3.2: Nominal power for the Daya Bay and Ling Ao (I and II) cores. Typical irradiation histories were analyzed from the 2005-2011 OPEX sheets [174] for these cores and we selected the most 'regular' history. A 'regular' history was defined to have no SCRAMs and no elongated shutdown periods. Figure by author.

From the nominal power history of the reactors, one can see that the average power is $\sim 2.85\,\mathrm{GW_t}$, in accordance with PRIS [176] and the OPEX sheets [174]. The Daya Bay cores run on 18 month cycles, while the Ling Ao cores run on 12 month cycles. Both experience shutdowns with lengths in the $30 - 60\,\mathrm{d}$ range, a typical value for PWRs.

Origen-S will take the power history supplied from Fig. 3.2, the Westinghouse 17×17 FA cross-section library, the fuel description, 72.4 MTU of 3.7%(4.45%) enriched UO_2 for the Daya Bay(Ling Ao) cores, and compute the reactor composition using a depletion method. This depletion method utilizes the matrix exponential solution, similar to Ref. [177] and described in App. B. The Origen-S output lists the nuclide abundance (in grams) at any given simulation time. These abundances can then be converted into an activity, by $\alpha_i = \lambda_i N_i$,

where λ_i is the decay constant of nuclide N_i. The activity is then used to determine the antineutrino spectrum via Ref. [128]. The spectrum produced at EOC represents the average SNF extracted during each refueling period. This spectrum can then be trivially extended to further decay times τ_d after the SNF has been removed and is cooling in the pools by exponentially decaying the SNF nuclides with their corresponding decay constants. An examination of this spectral decay reveals the appearance of the ^{90}Sr, ^{106}Ru, and ^{144}Ce decay chains.

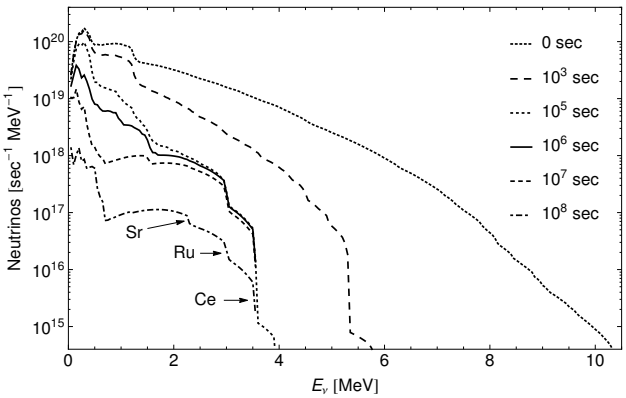

Figure 3.3: SNF generated by Origen-S neutrino signal at various decay times for a nominal irradiation cycle of a Daya Bay reactor. The long-lived nuclides of ^{90}Sr, ^{106}Ru, and ^{144}Ce begin to form sharp shoulders in the spectra even at early decay times $\sim 1\,\mathrm{d}$. Figure by author.

Figure 3.3 plots the decay of the SNF spectrum for a nominal Daya Bay core in the range of $\tau_d = 0 - 10^8\,\mathrm{sec}$. The shoulders of the ^{144}Ce and ^{106}Ru chains, which directly match the endpoint energies of ^{144}Pr and ^{106}Rh, appear as early as $10^5\,\mathrm{sec}$, or about $1.2\,\mathrm{d}$ after core shutdown. As the short-lived nuclides decay away, the high-energy antineutrino spectrum vanishes rapidly leaving only the long-lived nuclides after $\sim 1\,\mathrm{d}$. This indicates that for $\tau_d > 1\,\mathrm{d}$, the assumption that SNF is only composed of the ^{90}Sr, ^{106}Ru, and ^{144}Ce decay chains is valid, especially above IBD. Note that the antineutrino flux for the running reactor (i.e. at $\tau_d = 0$) reproduces the expected $\mathcal{O}(10^{20}\,\nu/\mathrm{sec})$ per $1\,\mathrm{GW_t}$ of reactor power.

One can simplify the time-dependence of the SNF signal by computing a time-averaged antineutrino rate. This is accomplished by an interpolation of antineutrino spectrum as a function of the exponential decay times and the antineutrino energy. This 2-variable interpolation is defined as $\phi^c_\nu(E, \tau_d)$, where the antineutrino flux has a core c dependence and $c = D(L)$ for the Daya Bay(Ling Ao) reactors. After binning $\phi^c_\nu(E, \tau_d)$ into energy bins, so that the i^{th} bin is given by $\hat{\phi}^c_i(\tau)$, one can calculate the time-averaged antineutrino rate in each bin. Next, a similar binning for the $\bar{\nu}p$ cross-section is performed, resulting in $\hat{\sigma}_i$. Solving for the time-averaged decay time that satisfies event conservation, given by Eq. 3.2

below allows for the removal of the time-dependence.

$$\int_0^{t_d} \sum_i^{N_b} \hat{\phi}_i^c(\tau_d)\hat{\sigma}_i d\tau_d = t_d \sum_i^{N_b} \hat{\phi}_i^c(\langle\tau_d\rangle)\hat{\sigma}_i \text{where} \qquad \hat{\phi}_i^c(\tau_d) = \int_{E_i}^{E_{i+1}} \phi_\nu^c(\tau_d, E) dE \quad (3.2)$$

The time-averaged decay time that satisfies the left-hand expression of Eq. 3.2, $\langle\tau_d\rangle$, will depend on the amount of data-taking time t_d. For the example of $t_d = 375\,\text{d}$, $\langle\tau_d\rangle \simeq 141\,\text{d}$ for both cores, meaning that a time-dependent SNF antineutrino signal observed for 375 d after shutdown can be simplified as a time-independent static SNF antineutrino signal decayed to $\sim 141\,\text{d}$ without event rate losses. This concept, with the choice of $t_d = 375\,\text{d}$, will be used to compute the sensitivity of Daya Bay to its SNF signal in Chp. 3.2.

A major trend to take from Fig. 3.3 is that about 100 d (10^7 sec) after the SNF is removed, the neutrino contribution above IBD is $\sim 1\%$ of the running reactor. A similar calculation has been conducted by Zhou *et al.* [178] in early 2012. The calculation assumed a 1 GW reactor with all conclusions made relative to a full 1-batch core irradiated for 330 d. This scenario resembles the Ling Ao reactor calculation, with 950 MW net capacity and an irradiation cycle of 12 months. By tracking nuclides with beta-decay endpoints above IBD, Zhou *et al.* was able to compute a direct solution of the Bateman equations using single-group cross-sections for the relevant nuclides. The spent fuel contribution was then compared with a running reactor and a ratio was computed in all energy bins at various decay times as in the left-hand diagram of Fig. 3.4 below: A similar ratio was then computed using the power

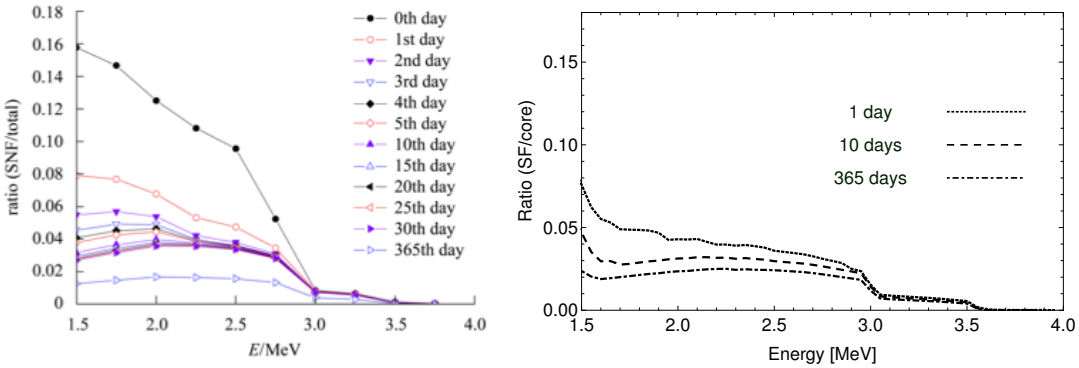

Figure 3.4: Comparison of the SNF contribution relative to a running 1 GW reactor at various decay times as a function of neutrino energy. On the left, Zhou *et al.* computed the contribution via Bateman equations [178] and on the right we have our Origen-S calculation of the SNF contribution for nearly identical reactor circumstances. Left figure courtesy of Ref. [178] and right figure by author.

history supplied in Fig. 3.2 and simulating the reactor with Origen-S.

From the comparison in Fig. 3.4, the Origen-S calculation matches the result of solving the Bateman equations quite nicely. The spectral shapes are slightly different at 1 d, which may

be attributed to specific nuclides considered by Zhou *et al.*. The endpoints and 'shoulder' locations at 3.0 and 3.5 MeV match extremely well and both methods return a $1-3\%$ contribution of SNF to the total reactor signal at decay times corresponding to reactor-on data (recall that shutdowns last $30-50$ d, so only SNF with $\tau_d > 30-50$ d will affect reactor data)[2]. Considering the possible variation of input parameters and different calculation details, the SNF contribution similarities are quite striking. The advantages of using Origen-S and SCALE are that real reactor parameters can be input (such as the design, enrichment, exact power history, shutdowns, and 3-batch characteristics) and all nuclide concentrations will be provided, ensuring no loss of critical information.

The last parameter that must be determined is the effect of additional SNF loads on the contribution. Our calculation from Fig. 3.4 only considers one SNF load, but the true number contained in the onsite pool is unknown. Therefore, an analysis must be conducted to study the effect of adding extra SNF loads. The total SNF neutrino spectrum will be a summation of multiple loads separated by one cycle time τ_c because each batch is removed τ_c days after the previous refueling. This concept is given as Eq. 3.3 below:

$$S_N(\tau_d, E) = \sum_{n=0}^{N-1} \phi^c(\tau_d + n\tau_c, E) \tag{3.3}$$

where the N^{th} freshest SNF loads are summed, each separated by τ_c decay time, for a core c. 'Freshest' indicates the most recently removed load from the reactor and τ_d decay time is added after the most recent shutdown. For our reactor analysis, we use $\tau_c = 521(326)$ d for the Daya Bay(Ling Ao) cores, as these are the average full cycle lengths from 6 years of OPEX data.

Examining the effect of adding subsequent SNF loads can be accomplished by the signal impact ratio, given by

$$R^c_{nm}(\tau_d, E) = \frac{S_m(\tau_d, E) - S_n(\tau_d, E)}{S_n(\tau_d, E)} \times 100 \tag{3.4}$$

where the relative effect of a SNF signal with m loads as compared to one with n loads is considered.

Figure 3.5 illustrates the comparison between 1 and 2 loads (blue), or $R^D_{12}(\tau_d, E)$, between 2 and 3 loads (gold), or $R^D_{23}(\tau_d, E)$, and between 3 and 4 loads (red), or $R^D_{34}(\tau_d, E)$ for the Daya Bay reactor. The relative difference is plotted along with vary neutrino energy E_ν at several decay times τ_d since the last shutdown. Above ~ 3.55 MeV, the relative difference is always zero as the older spent fuel signals (recall $\tau_c \gtrsim 1$ yr) will have no antineutrinos above the ^{106}Rh β-decay endpoint (~ 3.54 MeV). In addition, for lower values of τ_d the effect of adding more SNF is small. This is because the freshest load (with small τ_d) severely outshines the older loads in terms of the total antineutrino flux.

[2]This, of course, is only true for a single reactor, SNF source

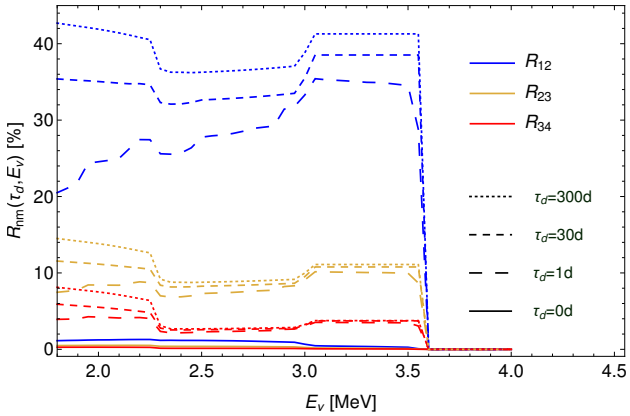

Figure 3.5: Analysis of the impact of adding older SNF loads to the total spent fuel neutrino contribution. We calculate the relative difference between 1 and 2 SNF loads (blue), 2 and 3 SNF loads (gold), and 3 and 4 SNF loads (red). We plot the relative difference of Eq. 3.4 at various decay times τ_d after last reactor shutdown and neutrino energy E_ν. Figure by author.

There is a clearly diminishing effect as more SNF loads are included, meaning that $R^c_{nm}(\tau_d, E)$ will decrease as n and m become very large. This result is encouraging and indicates that there is a finite number of spent nuclear fuel loads that should be considered. The SNF signal in Fig. 3.5 shows 3 distinct regions, the lowest energy region $E \lesssim 2.4\,\text{MeV}$ dominated by the ^{90}Sr chain, a middle energy region $2.4 \leq E \leq 3.0\,\text{MeV}$ shared by the ^{106}Ru and ^{144}Ce chains, and a high energy region $E \geq 3.0\,\text{MeV}$ dominated by the ^{106}Ru chain. In the regions dominated by the shorter lived chains of ^{106}Rh and ^{144}Ce the significance of adding more SNF loads is smaller (2-4% for R^D_{34}) than the ^{90}Sr-dominated region ($6-8\%$ for R^D_{34}). This is a direct result of the large half-life of ^{90}Sr, which means that the SNF impact is larger. Overall, choosing 3 SNF loads corresponds to a relative error of $\sim 8\%$ for $E_\nu \leq 2.4\,\text{MeV}$ and $4-6\%$ for $2.4 \leq E_\nu \leq 3.55\,\text{MeV}$. Therefore, 3 SNF loads is sufficiently accurate for our analysis and we proceed with $N = 3$ for both the Daya Bay and Ling Ao reactors.

A method for calculating the SNF signal via the reactor simulation suite SCALE, using publicly-accessible input data, has been identified and tested. Verification of SCALE with other methods [178] have been established deeming the method accurate. A time-averaging technique and the optimal number of spent fuel loads have been determined, meaning that a calculation of the Daya Bay sensitivity to spent nuclear fuel is possible. This sensitivity analysis will use the published Daya Bay event rates, backgrounds, and baselines in order to accurately represent the experiment with no need for additional data.

3.2 Spent Nuclear Fuel Sensitivity at Daya Bay

For the sensitivity calculation at Daya Bay, the entire neutrino experiment, including systematic errors and backgrounds, will need to be modeled. A simulation code designed to handle a variety of neutrino experiment designs is the Generalized Long Baseline Experiment Simulator (GLoBES) [179–181]. GLoBES has the ability to model a wide expanse of oscillation experiments, regardless of the neutrino source, and incorporates matter effects into a full sensitivity calculation with a user-defined set of uncertainties, energy resolutions, and more. The average reactor fission rates from the Origen-S calculations and the event rates provided by Daya Bay 8AD data [182] and later analyzed in Ref. [183] will normalize our GLoBES simulation to the observed reactor source. The SNF signals will then be added and a χ^2 computed for the reactor (Rx) + spent nuclear fuel (SNF) case compared with the only Rx case.

3.2.1 Daya Bay Application

First, the Daya Bay neutrino experiment will be outlined, as well as the normalization to its data. It is important to recreate the event rates from Daya Bay, so that the SNF sensitivity calculation will resemble what would actually occur in experiment. The Daya Bay neutrino oscillation experiment searches for the disappearance of reactor antineutrinos near the oscillation minimum. This location can be easily determined using the oscillation probability, following Chp. 2.1

$$P_{\bar{\nu}_e \to \bar{\nu}_e} = 1 - \sin^2 2\theta_{13} \sin^2 \left(\frac{\Delta m^2_{13} L}{4E} \right) - \cos^4 \theta_{13} \sin^2 2\theta_{12} \sin^2 \left(\frac{\Delta m^2_{12} L}{4E} \right) \tag{3.5}$$

for a baseline L and neutrino energy E. Using the PDG values from Tab. 1.1 for the oscillation parameters and the fact that the average reactor antineutrino energy is $\sim 4\,\mathrm{MeV}$ one can determine that the first minimum lies near 2 km. We will also see that Eq. 3.5 simplifies to the first two terms as $\Delta m^2_{12} \ll \Delta m^2_{13}$.

Daya Bay has designed its experiment such that the first oscillation is near one of the antineutrino detector (AD) sites, the far site. There is an accompanying near AD site for each reactor cluster. These AD sites, or experimental halls (EH), are given the designation EH1, EH2, and EH3, which correspond to the Daya Bay near site, the Ling Ao near site, and the joint far site, respectively. There are two ADs at EH1 and EH2 and four ADs at EH3. Each detector contains approximately 20 t of Gadolinium-loaded liquid scintillator in the innermost volume, assumed to be 20 t of CH_2 to simplify the calculation of the number of target protons. With a dual-baseline setup and functionally identical detectors, Daya Bay can normalize the events seen in the far detector with those in the near, effectively removing most of the detector-related systematic errors.

Data from the 8AD period (approximately 375 d data-taking) has been selected for this analysis. The following analysis includes the three main backgrounds (accidentals, fast neutrons, and cosmogenically produced ^{9}Li) from Ref. [182], where the background shapes are taken from Fig. 3.11 of Ref. [184]. The systematic errors and baselines used have been provided in Ref. [161]. The reactor event rates that are used in the normalization of the reactor signal are from Ref. [182] and the spent nuclear fuel ponds are assumed to be at most 30 m from the reactor sites. For the most conservative estimate, the spent nuclear fuel baselines were calculated by adding 30 m to all reactor baselines, even though this is geometrically impossible. This information is used to derive the normalization factor γ_{Rx} for our GLoBES simulation of the reactor signal to the actual events observed by Daya Bay. The SNF signal derived through SCALE will be used to determine a similar normalization factor γ_{SNF} for the spent fuel neutrinos.

Next, the input for the GLoBES simulation is explicitly described. A general note is that the energy binning structure used mimics that of Fig. 1 from Ref. [183], which has a larger first bin range of $1.55\,\text{MeV} \leq E_\nu \leq 1.80\,\text{MeV}$, then subsequent bins with width $\Delta E = 0.2\,\text{MeV}$ to 8.8 MeV. This binning structure is used in all input files, including the reactor antineutrino flux, the SNF flux, the $\bar{\nu}p$ cross-section, and the background signals. The reactor antineutrino flux is split into the four main fissiles and all of these inputs are calculated in the $1.55\,\text{MeV} \leq E_\nu \leq 8.8\,\text{MeV}$ range, with the obvious acknowledgement that most of the lowest energy bin is ignored due to the IBD threshold[3].

Each GLoBES input template references a particular flux file depending on the purpose. For example, the reactor templates for each of the experimental halls will reference the antineutrino flux files for the four main fissiles responsible for reactor fissions. The antineutrino yields per fission for ^{235}U, ^{239}Pu, and ^{241}Pu used are fit based on an exponential of a fifth order polynomial, following Ref. [128]. The ^{238}U is a similar exponential fit to Tab. III of Ref. [83]. These four fissile antineutrino yields have been compared with a naïve *ab initio* calculation, which couples the antineutrino spectra of each fission fragment, determined from Ref. [128], to the cumulative fission yields from two major libraries. This naïve approach agrees within $\sim 5\%$ in our region of interest for the spent nuclear fuel, roughly $1.8\,\text{MeV} \leq E \leq 3.55\,\text{MeV}$. This test was performed for the JEFF-3.1.1 data set [125] and the yields compiled by T.R. England and B.F. Rider [185]. The disagreement is primarily caused by the ^{238}U fission yields and the other three fissiles match within 2%.

The reactor templates will also contain reactor information and the detector qualities. Each GLoBES template reads in the flux files outlined previously, attaches a power ($2.9\,\text{GW}_\text{th}$) to each core, as well as an energy resolution distribution given by

$$\sigma(E_\text{vis}) = \begin{cases} \alpha(\sqrt{10})^{-6}\sqrt{E_\nu - 0.8} & , E_\nu > 1.8\,\text{MeV} \\ \alpha(10)^{-3} & , E_\nu \leq 1.8\,\text{MeV} \end{cases} \tag{3.6}$$

where $\alpha = 0.12$ for the Daya Bay experiment. This format takes into account the IBD

[3]The entire bin cannot be ignored due to the energy resolution of the detectors.

threshold and the shift from antineutrino energy to visible energy, which is where the actual energy resolution is applied. In addition, the reactor templates will read in the cross-section library. For our analysis we have used the $\bar{\nu}p$ cross-section from Ref. [147], including up to the $\mathcal{O}(1/M)$ in nucleon mass expansion. The flux template also contains the normalization factor γ, which we will elaborate on later. Finally, the individual fissile antineutrino fluxes are weighted by an appropriate power fraction. The power fraction ρ_f is a measure of the percentage of the reactor power generated by each fissile nuclide. This allows the option of providing the correct fission fractions for each reactor individually as we have two separate designs, Daya Bay and Ling Ao. Power fractions are defined by

$$\rho_f = \frac{\epsilon_f F_f}{\sum_f \epsilon_f F_f} \tag{3.7}$$

where ϵ_f are the energy yields (in MeV) per fission of a fissile 'f' as given by Ref. [122] and F_f are the fission fractions for each fissile. The values used for ρ_f are summarized in Tab. 3.2 and have been generated from reactor simulations of the nominal irradiation history for Daya Bay and Ling Ao-like reactors, assuming a 3-batch core loading scheme. The power fractions change with fuel burnup, thus an irradiation-averaged value of ρ_f at the midpoint of a fuel cycle is selected. Lastly, a flat Earth matter density profile of $2.7\,\mathrm{g/cm^3}$ is incorporated, but

	^{235}U	^{238}U	^{239}Pu	^{241}Pu
Daya Bay	0.494	0.076	0.350	0.080
Ling Ao	0.567	0.073	0.308	0.052

Table 3.2: Power fractions ρ_f used in the spent fuel sensitivity analysis of Daya Bay experiment. The power fractions differ for the Daya Bay and Ling Ao reactors as they operate on different enrichments and fuel cycle lengths.

this will not factor into the sensitivity analysis as the baselines are far too short. Combining all of this information: the flux files, the energy resolution, the reactor powers and power fractions, the $\bar{\nu}p$ cross-sections, and the Earth density profile one can reproduce the reactor template files.

For completeness, the normalization technique used is described next. First, three separate background signals are incorporated into our analysis. These are the backgrounds generated by accidental events, fast neutrons, and the β-n decay of cosmogenically produced ^{9}Li. Each of these backgrounds has the capability of imitating the true IBD signal, see Chp 2.3.2. Accidental signals involve two uncorrelated events accidentally satisfying the energy windows and prompt-delayed timing of a true signal. Fast neutrons can be produced by cosmic muons in the surrounding rock or the detector volume and then mimic the true signal by recoiling off of a proton and then thermalizing until it captures on Gd. Lastly, ^{9}Li has a significant β-n decay branch, which mimics the true signal as particle-antiparticle distinction for the electron

and positron is not possible in Daya Bay. The spectral shapes of these backgrounds are given in Fig. 3.6 below. The background shapes are derived as such: accidentals follow a $1/E$

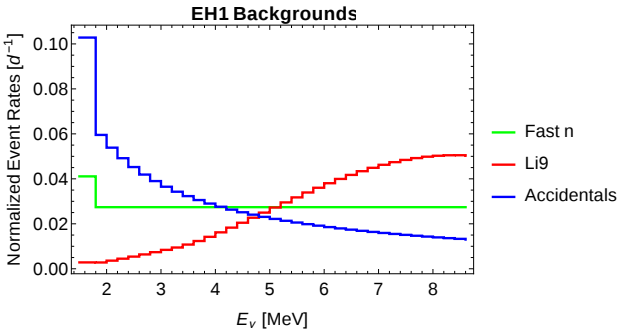

Figure 3.6: Normalized background rate (1 per day) of the accidentals (blue), fast neutrons (green), and ^{9}Li in the Daya Bay binning structure. Figure by author.

distribution, fast neutrons are given by a flat distribution, and the ^{9}Li decay follows its beta-decay spectrum. Each background shape is assumed to be identical for all three experimental halls. The absolute rate is adjusted based on the normalization scheme illustrated next.

The normalization technique utilizes the quoted event and background rates from the recent 8AD Daya Bay data given in Tab. 3.3 from Ref. [182]. We use the daily rates for the 8AD data taking period to set the daily events produced by our GLoBES simulation. The three

	IBD/day	Accidentals/day	Fast n/day	^{9}Li/day
AD1	659.58±2.12	8.62±0.09	0.78±0.12	2.8±1.5
AD2	674.36±2.14	8.76±0.09	0.78±0.12	2.8±1.5
AD3	601.77±1.67	6.43±0.07	0.54±0.19	1.7±0.9
AD8	590.81±1.66	6.86±0.07	0.54±0.19	1.7±0.9
AD4	74.33±0.48	1.07±0.01	0.05±0.01	0.27±0.14
AD5	75.40±0.49	0.94±0.01	0.05±0.01	0.27±0.14
AD6	74.44±0.48	0.94±0.01	0.05±0.01	0.27±0.14
AD7	75.15±0.49	1.26±0.01	0.05±0.01	0.27±0.14

Table 3.3: Events from the Daya Bay 8AD data taking period. This data is taken from Ref. [182]. Listed are the daily IBD event rates and background rates in each antineutrino detector.

background spectra are multiplied by a different normalization factor, keeping the shape constant, so that the total number of events produced across the 36 bins are equivalent to the reported rates of Tab. 3.3. A similar process is used for the reactor antineutrino rate, where the normalization constant within the GLoBES framework is adjusted until the IBD rates are equivalent to the those reported by Daya Bay for each AD. Therefore, with the proper value of the normalization factors, the exact 8AD experimental setup can be

reproduced as in Tab. 3.3. The normalization factor is a function of the detector mass, baseline, and the power fraction so different normalization factors are used for the different fission sources and experimental halls. To simplify, the fissile and experimental hall-averaged baselines are used so that γ_{Rx} is calculated separately for the four main fissiles (f) and the three experimental halls (e).

To summarize the normalization method, the values of γ_{Rx} in Tab. 3.4 are provided. This specific choice of γ_{Rx} results in simulated Daya Bay event rates that match those in Tab. 3.3, with only minor differences. We will discuss the incorporation of the errors in our spent fuel analysis later. The ADs have been grouped by experimental hall, so normalization factors used in the analysis are provided separately for each fissile and experimental hall. Equivalent

γ_{Rx}	EH1	EH2	EH3
^{235}U	6.18062	6.09218	6.12924
^{238}U	6.08638	5.99929	6.03579
^{239}Pu	6.04557	5.95906	5.99532
^{241}Pu	5.93901	5.85402	5.88964

Table 3.4: Normalization constants used in the GLoBES simulation to match Daya Bay 8AD event rates. The normalizations vary for experimental hall and fissile as they depend on the energy produced per fission and baseline.

normalization constants are used for each AD in the same experimental hall and for each core in a reactor unit. This is because the average baseline for each source and experimental hall has been used. The fissile dependence comes from the incorporation of the Kopeikin fission energy yields [122] into the power fraction. The difference in reactor styles is accounted for by multiplying the individual fissile antineutrino spectra by the power fractions, see Tab. 3.2. Together, with the power fractions for the two reactor types and the normalization factors for each experimental hall, the Daya Bay experimental rates are excellently matched. Next, the SNF background will be incorporated. To match the Daya Bay data we have used specific oscillation parameters, those found in Tab. 1.1, where we have chosen the best-fit value from the Daya Bay collaboration for $\sin^2(2\theta_{13})$ and included no CP-violation.

Applying the time-averaging decay technique for 3 nominal SNF loads to the Origen-S antineutrino spent fuel signal produces the SNF flux files to be used in GLoBES. The time-averaged decay of $\langle \tau_d \rangle = 141\,\mathrm{d}$ is used as the 8AD data corresponds to 375 d of data-taking, which satisfies Eq. 3.2. As there are no Daya Bay rates to compare to, normalization of the GLoBES event rates are done by propagating the Origen-S antineutrino rates along the baselines to the three experimental halls. This normalization is done for a no-oscillation case in order simplify the procedure and remove any bias towards oscillation values. After the values of γ_{SNF} are produced, oscillation is turned back on. Recall that the previous flux files were normalized per fission, so the same is done to the SNF flux files as well. This normalization occurs over all fissions of each fissile, so γ_{SNF} will, in this case, depend on the

total number of fissions, the baselines, and the detector mass. As the Daya Bay and Ling Ao reactors reach different burnups (essentially number of fissions), our SNF normalization γ_{SNF}, will be different for the two reactor designs and the three experimental halls, which are presented in Tab. 3.5 below. Now that the reactor and spent fuel antineutrino flux files

γ_{SNF}	EH1	EH2	EH3
Daya Bay	10.3177	10.2955	10.3625
Ling Ao	10.3395	10.3172	10.3843

Table 3.5: Spent fuel normalization constants for use in the GLoBES simulation to match the decay time-averaged events of the SCALE-generated SNF neutrino spectra.

have been generated and the proper normalization constants derived, the full oscillation in GLoBES and comparison between the reactor antineutrino signal to the spent nuclear fuel antineutrino signal can be computed. The fully oscillated calculation is described next.

3.2.2 Daya Bay Sensitivity Calculation

The sensitivity calculation is performed using a χ^2 analysis within the GLoBES simulation. The simulation code sets up the Daya Bay experimental site, with the proper baselines, detector designs, cross-sections, and source files as outlined previously. The incorporated uncertainties are those from Ref. [161], summarized in Tab. 3.6 below. These errors are

Det. Norm.	Bkg. Norm.	Rx. Norm.	Burnup	σ_{binbin}
0.2%	50%	0.8%	0.6%	0.3%

Table 3.6: Uncorrelated systematic uncertainties used in the spent fuel sensitivity analysis for the detector, background, and reactor normalization. Also included are the uncorrelated burnup (fission fractions) uncertainty and the bin by bin energy uncertainty (σ_{binbin}) we have used.

applied to the fit antineutrino spectrum as generated from the reactor and background signals only. One of the burnup errors will be constrained, as the fission fractions for the four fissiles is required to sum to unity. The background error is taken to be the maximal value among all three backgrounds, which is the ^{9}Li decays. In addition, an overall free normalization parameter is allowed to vary in the fit.

Next, the true spectrum (T=Rx+Bkg+SNF) is produced, which now includes the spent fuel antineutrinos, and an attempt to fit this to the reactor-only spectrum (F=Rx+Bkg) is made. A χ^2 is computed between these two spectra over all 36 bins, where Gaussian statistics (i.e. $\sigma_i = \sqrt{N_i}$ where N = events in bin i) are used for the bin errors. In addition, the 'true'

neutrino mixing parameters are allowed to vary by their 1σ errors identified in Tab. 1.1. The χ^2 is given below.

$$\chi^2 = \sum_{i}^{36} \frac{(R_{T,i} - R_{F,i})^2}{\tilde{\sigma}_i} + \sum_{e}^{N_e} \left(\frac{\alpha_e}{\sigma_e}\right)^2 \tag{3.8}$$

where the fitted rates in bin i, with the normalization uncertainties α_e, are given by $R_{F,i}$. The true spectrum (including SNF) in bin i are given by $R_{T,i}$. The Gaussian errors must be slightly modified to account for the bin-by-bin uncertainty, so that $\tilde{\sigma}_i = R_{T,i}(1+R_{T,i}\times\sigma_{binbin})$. Finally, the errors are added to the χ^2 in the form of a sum of a squared ratio of the normalization constants α_e over the uncertainties σ_e for any given error e.

The χ^2 computation involves several normalization factors α_e for various error sources, which are identified here. First, the errors in the reactor antineutrino events detected $N^{s,f}_{R,i,d}$ in an energy bin i, at a detector d, from a single fission by a fissile f, and from a core source s are outlined. Each fissile has a burnup uncertainty normalization attached to it $\alpha_{s,f}$ that also depends on the source s. The fission events are summed into a total reactor signal, with an overall normalization constant for the source α_s. The events are detected in a given AD with a normalization factor of α_d. Thus, the event reconstruction process is given as Eq. 3.9 below

$$R_{R,i,d} = \alpha_d \sum_{s=1}^{N_s} \alpha_s \left[N^{s,1}_{R,i,d} + \sum_{f=2}^{4} \left(\alpha_{s,f} \cdot N^{s,f}_{R,i,d} \right) \right] \tag{3.9}$$

Note that one of the fissiles, $f = 1$ here, is constrained by $\sum_f^4 F_f = 1$ and so has no uncertainty associated with it. A similar process is computed for the 3 background sources. In this case, a uniform normalization factor across all backgrounds is assumed α_b, so that the total background events in an energy bin i and for a detector d is given by

$$R_{B,i,d} = \sum_{b=1}^{3} \alpha_b \cdot N^b_{B,i,d} \tag{3.10}$$

with the background events detected $N^b_{B,i,d}$ in an energy bin i, for a given detector d, and for a background source b. Summing Eq. 3.9 and Eq. 3.10 into a total fitted event spectrum with a free overall normalization factor α_o, is then written as

$$R_{F,i} = \sum_{d=1}^{8} \left[\alpha_o \cdot R_{R,i,d} + R_{B,i,d} \right] \tag{3.11}$$

where the background event normalization is fixed by the Daya Bay data, so normalization is necessary. In principle, the true spectrum is calculated in a similar way, except with all normalization constants set to unity, i.e. $\alpha_e = 1$. There is also the addition of the spent fuel antineutrinos manifesting itself as another event term so that the true rate is a modification of Eq. 3.11 to

$$R_{T,i} = \sum_{d=1}^{8} \left[R_{R,i,d} + R_{B,i,d} + R_{S,i,d} \right] \tag{3.12}$$

where the overall normalization has already been set to 1 and $R_{S,i,d} = \sum_{s=1}^{6} N^s_{S,i,d}$. Similarly, $N^s_{S,i,d}$ are the SNF events in an energy bin i, from a sources s, and for a detector d. Now, the true and fitted event rates per bin can be compared to acquire the χ^2 given in Eq. 3.8. The total number of errors and normalization constants is $N_e = 42$, including 6 reactor normalizations, 8 detector normalizations, $3 \cdot 6 = 18$ fission fraction normalizations ($4-1=3$ fissiles and 6 reactors), 1 overall normalization, and $3 \cdot 3 = 9$ background normalizations (3 types of backgrounds and 3 experimental halls).

In the χ^2 calculation the oscillation parameters as outlined in Tab. 1.1 have been used with no CP violation. Restricting our sensitivity analysis to the Daya Bay 1σ variance of $\sin^2 2\theta_{13}$ [183], results in Fig. 3.7 below. The χ^2 reported in Fig. 3.7 has not yet been reduced

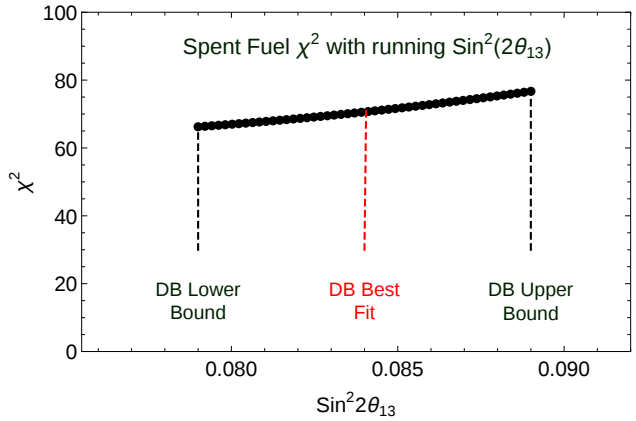

Figure 3.7: Running value of the χ^2 between the true rates (Rx+SNF+Bkg) and the fitted rates (Rx+Bkg) as we span the 1σ allowed space for $\sin^2 2\theta_{13}$ from the most recent Daya Bay publication of Ref. [183]. We have labeled the best fit value from Daya Bay with the red marker. Figure by author.

by the number of degrees of freedom, but the somewhat linear dependence of χ^2 on the choice of $\sin^2 2\theta_{13}$ is extremely clear. Spanning the allowable values for $\sin^2 2\theta_{13}$, the χ^2 varies from ~ 67 to ~ 80 from the lower Daya Bay bound to the higher one. This variation is explainable with Eq. 3.5, noting that the spent fuel antineutrinos will have a lower average energy than the reactor antineutrinos. This results in a higher sensitivity to the choice of $\sin^2 2\theta_{13}$ in the second term, because the value of $\sin^2(\Delta m^2_{13} L/4E)$ is larger. Thus, decreasing θ_{13} will have a more drastic effect to reduce the oscillation probability of spent fuel antineutrinos than to reduce the reactor antineutrinos.

The full sensitivity analysis is computed with the incorporation of each individual experimental hall. For each hall the impact of the SNF antineutrinos is analyzed. In the following plot, the shape of the spent fuel spectrum as well as its relative impact on the reactor spectrum is shown. The corresponding 1σ Gaussian errors associated with each energy bin are included for reference. This result is given as Fig. 3.8 below and represents the seminal result for the sensitivity of the Daya Bay antineutrino experiment to spent nuclear fuel. In Fig. 3.8

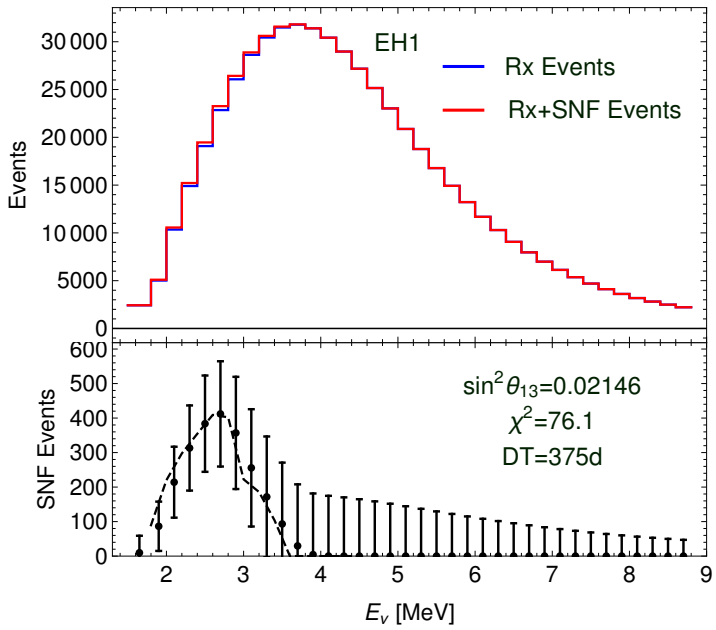

Figure 3.8: The top panel gives the detected neutrino events for 375 d from the reactor and background (blue) compared with the reactor, background, and spent fuel (red). The events are binned according to the Daya Bay binning structure. The lower panel shows the spent fuel events acquired by subtracting the blue from the red curve. The fitted shape of the spent fuel neutrino spectrum (dashed) shows the hard endpoint at ~ 3.55 MeV. The fitting process is described in the text. Also listed are the 1σ errors associated with the total events (reactor+background+spent fuel) in each bin. Figure by author.

the Daya Bay best fit value of $\sin^2 2\theta_{13} = 0.084$ is used and the resulting spent nuclear fuel deviation is observed in the near experimental hall (EH1) with 375 d of data taking. Using data from the two short-baseline experimental halls results in a $\sim 2.5\sigma$ deviation from the solution without spent fuel antineutrinos. This significance is aided by the fact that the spent fuel spectrum contains a discrete energy endpoint meaning that, even with energy resolution errors and a nonlinear detector response, the signal can be easily extracted in a selected number of energy bins. The sensitivity in the far hall is much lower, where the SNF signal is barely above bin errors and contributes ~ 13 units of χ^2. This calculation of the significance uses $N = 2 \times 14 - 1$ degrees of freedom and the total critical χ^2 value of 46.5 across EH1 and EH2; the χ^2 in Fig. 3.8 includes EH3 and all 36 bins. The selection of the 14 lowest energy bins leads to the high level of significance and is justified as the only bins containing SNF are below 3.6 MeV.

The dashed fit to the spent fuel spectrum uses the black data points and attempts to fit the SNF data to the combined antineutrino spectrum of the three main long-lived nuclide chains that comprise SNF: the ^{90}Sr, ^{106}Ru, and ^{144}Ce chains. After defining the fitting method, the

physics goals of fitting the SNF composition will be discussed along with its inaccuracies. The fit is given by an overall free normalization and the constraint that these three nuclide chains must comprise the entirety of the SNF signal. The fitting structure is given below

$$N_{SF}(E) = \delta_e[\alpha_e N_{^{90}\mathrm{Sr}}(E) + \beta_e N_{^{106}\mathrm{Ru}}(E) + \gamma_e N_{^{144}\mathrm{Ce}}(E)] \quad \text{where} \quad \alpha_e + \beta_e + \gamma_e = 1 \quad (3.13)$$

Note that the SNF contributions will have a strong dependence on the experimental hall. This arises after considering that EH1 will be closer to Daya Bay and, thus, should see a more Daya Bay-like SNF composition. The same applies for EH2 and the Ling Ao reactors. Finally, the far hall (EH3) will see a mixture of the Daya Bay and Ling Ao-like SNF compositions.

The determination of the spent fuel composition can lead to an indication of the age of the spent fuel. This concept utilizes the differences in half-lives of the three main long-lived nuclides. As the SNF ages, its composition will change following the exponential decay of the three nuclide chains. If a typical initial composition is known, information that can be generated via the reactor simulations as in Chp. 3.1.2, a determination of the nuclide percentages in the SNF will yield a measurement of the age of the spent fuel. This process becomes more complicated after considering multiple spent fuel loads, which will have a more ^{90}Sr-dominated neutrino spectrum and may hinder this analysis. What ultimately renders this concept unfeasible is the fact that the combination of cross-sections and the different antineutrino spectra break the equality between the number of antineutrinos emitted and those detected. Essentially, removing a ^{106}Rh antineutrino event will decrease the SNF event rate, but this signal decrease can be compensated by adding both a ^{90}Y and ^{144}Pr antineutrino event and altering the overall normalization. This results in a non-unique solution for the SNF composition.

To practically illustrate this, we give the parameters of Eq. 3.13 that have been used to fit the spent fuel spectrum seen in Fig. 3.8, but also present a completely different set of constants that also fit the detected SNF spectrum well. These constants are given in Tab. 3.7, where the first row represents the fit returned from Fig. 3.8 and the second row is a forced fit, where we have manually altered the values of α,β,γ, and δ to return a similar fit. It should be noted that the computationally derived SNF parameters are preferred, but the manual SNF parameters fit well within the error bars of each bin. As both of these selections yield

	α_1	β_1	γ_1	δ_1
Fitting Scheme	23.6%	36.2%	40.2%	50721
Manual Fit	15%	35%	50%	50000

Table 3.7: Spent fuel composition parameters for a fitting scheme (first row) defined by Eq. 3.13 and a manual fit (second row). We note that both fitting parameters match the SNF neutrino spectrum determined from GLoBES within the error bars listed in Fig. 3.8, but show very different compositions for SNF signal seen at the Daya Bay near hall.

acceptable fits for the SNF spectrum and they represent drastically different compositions,

the method of relating the spent fuel composition to its age cannot be pursued until a more suitable solution can be developed.

3.3 Spent Nuclear Fuel Conclusion

In this chapter the spent nuclear fuel was introduced as a possible background signal for reactor antineutrino experiments. The origin of the SNF signal was discussed and an accurate method of calculating the nuclide composition of the spent fuel via reactor simulations, mainly Origen-S, was determined. After applying an antineutrino spectrum to this signal, some interesting properties of the background were uncovered. First, the decaying nature of the SNF was illustrated, where the majority of antineutrinos for spent fuel older than $\sim 1\,\mathrm{d}$ are produced solely by the decays of the ^{90}Sr, ^{106}Ru, and ^{144}Ce chains. Second, reactor simulations determined that the 3 freshest SNF signals accurately represent the total SNF within 8%. Third, the problem was simplified drastically by making the SNF a time-independent signal via event conservation. Finally, comparisons with other methods showed similar ratios for the SNF signal to the reactor-on antineutrino rate. This determined that SNF contributes a $2-4\%$ effect in the low-energy bins.

This calculation of the SNF signal, using publicly accessible OPEX sheets [174] for the reactor simulations, was then applied to the Daya Bay neutrino experiment. Using real Daya Bay data [182] the experimental event rates were accurately reproduced, ensuring our model of the neutrino experiment was sound. Next, the reactor and SNF signals were incorporated into a GLoBES sensitivity calculation and found that the total signal (including spent fuel antineutrinos) manifests itself as a $\sim 2.5\sigma$ deviation from reactor antineutrinos alone with 375 d of data taking in the 8AD scenario. This result should be identifiable as a low energy excess (in the $1.8 \leq E_\nu \leq 3.55\,\mathrm{MeV}$ range) with a discrete endpoint at 3.55 MeV and the shape described in Fig. 3.8. With additional data-taking time, the excess will become more apparent and may surpass the large low-energy flux errors [83, 128] and the energy resolution errors [182]. The SNF excess measurement would be the first confirmation of a SNF neutrino source at a reactor neutrino experiment.

The event rates that are acquired from the GLoBES sensitivity analysis with the best fit value for $\sin^2 2\theta_{13}$ from Daya Bay [182] and the other oscillation parameters according to Tab. 1.1 are given in Tab. 3.8. All three main backgrounds are summed and an overall $1.5-2\%$ rate correction is found from spent nuclear fuel for the near experimental halls. The far hall is has a much lower sensitivity to the SNF. Currently, this excess is well within the Daya Bay low-energy errors.

A measurement of the SNF excess is of critical importance to move forward in the age of precision neutrino physics. When the SNF correction ($1-3\%$ in the low-energy bins) is framed next to the reactor antineutrino anomaly [81] ($4-6\%$ overall), which has provided impetus for sterile neutrino searches, we can see that the SNF contribution would provide a

	IBD/day	$\sum$Backgrounds/day	IBD/day from SNF
AD1	661	3.10	12.2
AD2	672	3.16	12.3
AD3	600	2.73	8.67
AD8	591	2.69	9.10
AD4	75.1	0.324	1.39
AD5	75.0	0.324	1.26
AD6	74.6	0.322	1.26
AD7	74.5	0.322	1.58

Table 3.8: Simulated events from the Daya Bay 8AD data taking period lasting $\sim 375\,\mathrm{d}$. This data is for the Daya Bay best-fit value of $\sin^2 2\theta_{13} = 0.084$ is used along with the other oscillation parameters of Tab. 1.1. The three backgrounds are summed and an overall excess of $1.5 - 2\%$ event rate is seen from spent nuclear fuel.

worsening effect in the low-energy region of this anomaly. Figure 3.9 illustrates a comparison of two such low-energy corrections: the non-equilibrium correction, applying Tab. VII from Mueller *et al.* [83] to PWR-like fission fractions and a time-averaged single SNF load. The non-equilibrium correction acts to shift the observed to expected ratio in long irradiation reactor neutrino experiments, but the SNF correction would also add to this shift as seen in Fig. 3.9. Furthermore, the shift is compounded in the low-energy region, currently the energy bins with some of the largest errors across all reactor neutrino experiments [48, 49, 182].

On the note of precision oscillation studies, the disappearance signal for $\mathcal{P}_{\bar{\nu}_e \to \bar{\nu}_e}$ is most drastically seen in the low-energy bins of the three main reactor oscillation studies [48,49,182]. If the SNF and NE contribution are not properly accounted for in the background estimates, the oscillation signal can be weakened, affecting the best-fit value for $\sin^2 2\theta 13$. For this reason, the use of multiple baselines is of critical importance. In addition, searches hoping to extract the geoneutrino signal from reactor subtraction heavily rely on accurate spectral modeling [172, 173]. To compound this problem, the geoneutrino signal would be located in the exact energy bins most affected by the NE and SNF corrections. Therefore, accurate knowledge of all backgrounds and corrections, including the SNF is required for anomaly quantification, precision neutrino studies, and geoneutrino searches.

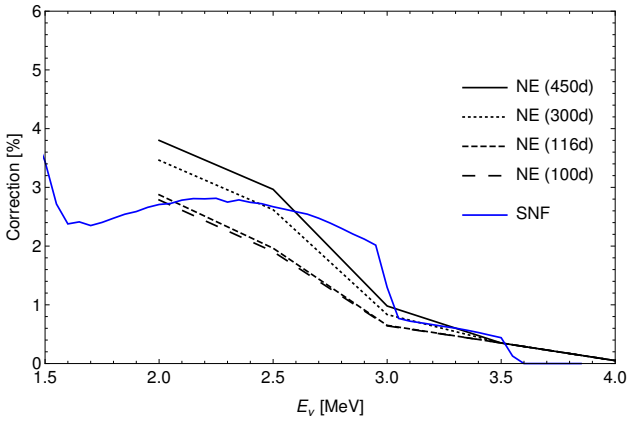

Figure 3.9: Comparison of the spent nuclear fuel (SNF) correction (blue) with the non-equilibrium correction calculated by Mueller *et al.* [83] for four different irradiation times with PWR-like fission fractions. We see that the SNF correction is of the same order of correction to the total reactor signal. This SNF signal is the time-averaged correction for the $\tau_d = [40, 365]$ d interval representing a single load experimentally measured for a typical irradiation cycle. Figure by author.

Chapter 4

Non-linear Correction

This chapter will introduce the non-linear correction to the antineutrino spectrum from nuclear reactors that is generated from specific neutron-capture nuclides. Thus, the decay rates of these nuclides, and their corresponding antineutrino rates, depend on both the thermal neutron flux as well as the irradiation period, instead of just the thermal flux as in linear nuclide decay rates. A description of the origin of this correction and an analytical solution are derived. This analytical solution is compared with reactor simulations, computed via SCALE [145] to verify its accuracy and ensure that the physics is well-understood. Full reactor simulations are used to estimate the non-linear correction to six different reactor designs, spanning nearly 3 orders of magnitude in thermal neutron flux. The simulation suite is described in App. B. The chapter ends with a brief discussion of the impact of the non-linear correction to neutrino experiments.

This research contributes to the results found in Ref. [1]. The full description and derivation of the non-linear correction, as well as the reactor simulation verification is described next.

4.1 Non-linear Nuclide Introduction

Non-linear nuclides are nuclides whose decay rate in a reactor environment is not solely determined by the neutron flux, but rather $\phi_t^2 T_{\text{irr}}$, the exact dependence will be calculated later. This is contrary to linear nuclides, which comprise the majority of reactor fragments. Most nuclides in a nuclear reactor environment will be in equilibrium within 10 d of irradiation. This equilibrium implies that their production and destruction rates are equivalent. The vast majority of fission fragments produced in a nuclear reactor are neutron-rich, rapidly decaying nuclides, which indicates that these nuclides are predominantly produced by fission and destroyed by decay. That is,

$$\frac{dN_L}{dt} = \vec{Y}_L \cdot \mathcal{F} - \lambda_L N_L \tag{4.1}$$

Eq. 4.1 is the rate of change for linear nuclides. In equilibrium, the fission rates $\vec{Y}_L \cdot \mathcal{F}$ will equal the decay rate $\lambda_L N_L$, such that $\vec{Y}_L \cdot \mathcal{F} = \lambda_L N_L$; note that $\lambda_L N_L = \alpha_L$ where α_L is the activity of N_L. Recalling that the fission vector can be written in terms of the thermal neutron flux ϕ_t and macroscopic fission cross-section Σ_{fiss} means that $\lambda_L N_L/dt \propto \phi_t$. Therefore, the ratio of non-linear to linear decay rates will result in an overall $\phi_t T_{\text{irr}}$ factor, the fluence.

The physics behind non-linear nuclides lie in the differential equation governing their abundance. A general equation for all nuclide abundances in a reactor environment is given by our generalized Bateman, see Eq. 2.24, which is reproduced here

$$\frac{dN_{\alpha,i}}{dt} = \vec{Y}_{\alpha,i} \cdot \vec{\mathcal{F}} - (\lambda_{\alpha,i} + \phi_t \sigma_{\alpha,i}) N_{\alpha,i} + \lambda_{\alpha,i-1} N_{\alpha,i-1} + \phi_t \sigma_{\alpha-1,j} N_{\alpha-1,j} \tag{4.2}$$

Recall that this equation describes the change in abundance of a nuclide $N_{\alpha,i}$, with irradiation time t. The index α here indicates which parent beta-decay chain $N_{\alpha,i}$ falls under. For example, if one were to select $\alpha = {}^{135}\text{Te}$, then the nuclides ${}^{135}\text{I}$, ${}^{135}\text{Xe}$, ${}^{135}\text{Cs}$, and ${}^{135}\text{Ba}$ would all fall under the α beta-decay chain as the chain is defined as:

$${}^{135}\text{Te} \xrightarrow{\beta} {}^{135}\text{I} \xrightarrow{\beta} {}^{135}\text{Xe} \xrightarrow{\beta} {}^{135}\text{Cs} \xrightarrow{\beta} {}^{135}\text{Ba} \tag{4.3}$$

where the chain ends at stable ${}^{135}\text{Ba}$. Effectively, α can be thought of as the atomic mass $A = N + P$. Equation 4.2 illustrates the different methods of production for $N_{\alpha,i}$ (positive terms) via fission yields $\vec{Y}_{\alpha,i} \cdot \vec{\mathcal{F}}$, neutron captures on an isotope $\phi_t \sigma_{\alpha-1,j} N_{\alpha-1,j}$, and decays from a parent isobar $\lambda_{\alpha,i-1} N_{\alpha,i-1}$. It also describes the ways that $N_{\alpha,i}$ can be destroyed, either through its own neutron captures $\phi_t \sigma_{\alpha,i} N_{\alpha,i}$ or its own decays $\lambda_{\alpha,i} N_{\alpha,i}$. We introduce the 'effective decay constant,' defined as $\tilde{\lambda}_{\alpha,i} = \lambda_{\alpha,i} + \phi_t \sigma_{\alpha,i}$ for simplification, where the effective decay constants now have a thermal neutron flux dependence.

The first task will be to identify what categorizes a fission fragment as 'linear' or 'non-linear.' The brief description above has already provided hints towards this. Linear nuclides will be those with decay rates dependent on the thermal neutron flux. Non-linear nuclides, specifically those due to neutron-captures, will be those with decay rates dependent on higher powers of ϕ_t. At first glance, this means that non-linear nuclides will have large $\phi_t \sigma_{\alpha-1,j} N_{\alpha-1,j}$ or $\phi_t \sigma_{\alpha,i} N_{\alpha,i}$ terms, as these explicitly have a flux dependence and so can reproduce the needed ϕ_t^2 dependence. This concept is derived next, which is then used, in conjuncture with reactor simulations, to determine the physics and impact of non-linear nuclides that produce antineutrinos on the total reactor antineutrino flux.

4.1.1 Constructing non-linear nuclides

First, the so-called 'linear' nuclides are discussed, named because their decay rate is primarily governed by the fission rate. The vast majority of reactor antineutrinos come from linear

nuclides. We begin with the abundance expression for the parent nuclides of any given chain α, denoted as $N_{\alpha,1}$, and given by Eq. 2.26, repeated here

$$\begin{aligned} N_{\alpha,1}(t) = \left[N_{\alpha,1_0}\right] e^{-\tilde{\lambda}_{\alpha,1}t} + \left[\frac{\phi_t \sigma_{\alpha-1,j} B_{\alpha-1,j} + \vec{Z}_{\alpha,1} \cdot \vec{\mathcal{F}}}{\tilde{\lambda}_{\alpha,1}}\right]\left(1 - e^{-\tilde{\lambda}_{\alpha,1}t}\right) \\ + \left[\sum_{n=1}^{j} \frac{\phi_t \sigma_{\alpha-1,j} A_{\alpha-1,n}}{\tilde{\lambda}_{\alpha,1} - \tilde{\lambda}_{\alpha-1,n}}\left(e^{-\tilde{\lambda}_{\alpha-1,n}t} - e^{-\tilde{\lambda}_{\alpha,1}t}\right)\right] \end{aligned} \tag{4.4}$$

where the corresponding descriptions of each term are given in Chp. 2.2.2, but we specifically reiterate that the undetermined coefficients $A_{\alpha-1,n}$ and $B_{\alpha-1,j}$ are given by the neutron capture parent of $N_{\alpha,1}$ written in the form:

$$N_{\gamma,j} = \sum_{n=1}^{j} A_{\gamma,n} e^{-\tilde{\lambda}_{\gamma,n}t} + B_{\gamma,j} \tag{4.5}$$

Again, the notion that all nuclides in a nuclear reactor can be written in the form of Eq. 4.5 and that this is not a special case is emphasized. Returning to the 'linear' claim, first investigate what occurs in Eq. 4.4 when $N_{\alpha,1}$ is a rapidly decaying nuclide, meaning that $\tilde{\lambda}_{\alpha,1} \sim \lambda_{\alpha,1}$. For this claim the following requirement is fulfilled, such that

$$\text{if} \quad \lambda_{\alpha,1} \gg \phi_t \sigma_{\alpha,1} \qquad \text{then} \quad \tilde{\lambda}_{\alpha,1} \to \lambda_{\alpha,1} \qquad \text{where} \quad \tilde{\lambda}_{\alpha,1} = \lambda_{\alpha,1} + \phi_t \sigma_{\alpha,1} \tag{4.6}$$

This leads one to ask when $\lambda_{\alpha,1} \gg \phi_t \sigma_{\alpha,1}$ is valid. Analyzing the independent yields found in the the JEFF [125] database for ^{235}U, ^{239}Pu, and ^{241}Pu will result in an answer to this question. There are ~ 900 unique nuclides in these three fission yields data sets. Of these, ~ 300 contain (n,γ) cross-section data in CINDER [186]. The remaining 2/3 are short-lived nuclides $\tau_{1/2} \leq 1000\,\text{sec}$, which make cross-section measurements extremely difficult. The reason for this experimental difficulty is that the source simply decays too rapidly for any sort of significant neutron bombardment, which is echoed in Eq. 4.6, where $\lambda_{\alpha,1}$ is simply too large for any reasonable ϕ_t to contribute to $\tilde{\lambda}_{\alpha,1}$.

Selecting these 300 nuclides, the critical thermal neutron flux ϕ_t^{crit} is calculated such that $\lambda_{\alpha,1} = \phi_t^{\text{crit}} \sigma_{\alpha,1}$, and a distribution of nuclides that **do not** satisfy Eq. 4.6 and, therefore, would have a non-negligible neutron-capture component is revealed. Limiting this distribution to nuclides with $\phi_t^{\text{crit}} \leq 10^{17}\,\text{n/cm}^2\text{/sec}$ (already 2 orders of magnitude higher than the current limit at the High Flux Isotope Reactor at Oak Ridge National Lab [187]), it becomes apparent that the only nuclides that provide comparable neutron-capture rates to beta-decay rates are far from the region of highest fission yields (red), as seen in Fig. 4.1. This is important as the highest yield region is also where the beta-chain parents reside. Specifically, the yields for ^{239}Pu are given below.

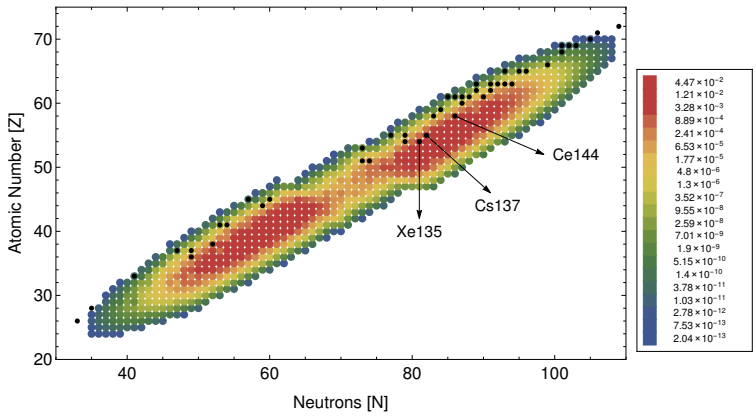

Figure 4.1: A plot of the fission yields for ^{239}Pu according to the JEFF independent yields dataset [125] against the number of neutrons (N) and protons (Z). Individual yields are plotted as the color axis (in atoms/fission). Also plotted are the nuclides from all fissile yields (^{235}U, ^{239}Pu, and ^{241}Pu) with $\phi_t^{\text{crit}} \leq 10^{17}\,\text{n/cm}^2\text{/sec}$ in black (see text for definition), with notable nuclides tagged. Figure by author.

Figure 4.1 illustrates this claim, where the black nuclides **do not** satisfy Eq. 4.6 for $\phi_t^{\text{crit}} \leq 10^{17}\,\text{n/cm}^2\text{/sec}$. These nuclides indicate that their neutron capture rates are comparable to their decay rates for a thermal neutron flux less than $10^{17}\,\text{n/cm}^2\text{/sec}$, within the conceivable fluxes of modern nuclear reactors. Some important nuclides with large capture rates are listed for comparison. One such nuclide is the infamous ^{135}Xe, a neutron poison within reactors and the nuclide responsible for the Chernobyl disaster [188]. The cross-section of ^{135}Xe is abnormally large at $\mathcal{O}(10^6\,\text{b}$, making it a heavy sink of thermal neutrons and greatly affecting the effective multiplicity k_{eff}. However, this also provides an intriguing measure for the thermal neutron flux of a reactor [189]. Also, listed are two long-lived nuclides ^{137}Cs and ^{144}Ce, the latter contributing to the SNF signal in Chp. 3.1.1. Examining the location of these nuclides with significant neutron-capture rates one can easily see that they all fall farther down the beta-decay chain and, thus, could not be considered parent nuclei by the previous definition of rapid decays and high fission yields. Similar results occur for ^{235}U and ^{241}Pu.

Continuing this argument leads to the conclusion that all parents of the beta-decay chains, which lie in the maxima region of the fission yields (red in Fig. 4.1), have sufficiently high decay rates such that $\tilde{\lambda}_{\alpha,1} = \lambda_{\alpha,1}$ for reasonable values of ϕ_t. If these beta-chain parents preferentially decay, then neighboring isotopes, also beta-chain parents, will have a negligible neutron capture rate. Thus, terms proportional to $\phi_t \sigma_{\alpha-1,j}/\lambda_{\alpha,1}$ will be small compared to $\vec{Z}_{\alpha,1} \cdot \vec{\mathcal{F}}/\lambda_{\alpha,1}$ in Eq. 4.4. Thus, the assumption of $\sigma_{\alpha-1,j} \to 0$ holds for beta-chain parents leading to Eq. 2.27, repeated here

$$N_{\alpha,1}(t) = \left[N_{\alpha,1_0}\right] e^{-\lambda_{\alpha,1} t} + \left[\frac{\vec{Z}_{\alpha,1} \cdot \vec{\mathcal{F}}}{\lambda_{\alpha,1}}\right]\left(1 - e^{-\lambda_{\alpha,1} t}\right) \tag{4.7}$$

Now, any beta-chain parent $N_{\alpha,1}$ can be absolutely determined from its cumulative fission yields $\vec{Z}_{\alpha,1}$, the reactor fission vector $\vec{\mathcal{F}}$, an initial abundance $N_{\alpha,1_0}$, and its decay constant $\lambda_{\alpha,1}$. Note that the additional simplification of $\tilde{\lambda}_{\alpha,1} = \lambda_{\alpha,1}$ has been made here as well. As a quick aside, Eq. 4.7 can be expressed in the general form of Eq. 4.5 with the assignments $A_{\alpha,1} = N_{\alpha,1_0} - \vec{Z}_{\alpha,1} \cdot \vec{\mathcal{F}}/\lambda_{\alpha,1}$ and $B_{\alpha,1} = \vec{Z}_{\alpha,1} \cdot \vec{\mathcal{F}}/\lambda_{\alpha,1}$.

Equation 4.7 provides both a starting point for the non-linear calculation as well as the first example of a linear nuclide. Recall that the fission vector has an implied ϕ_t dependence as $\vec{\mathcal{F}} = \phi_t \vec{\Sigma}_{fiss}$, where $\vec{\Sigma}_{fiss}$ is the macroscopic fission cross-section of the fissiles. Solving for the activity $\lambda_{\alpha,1} N_{\alpha,1}$ from Eq. 4.7, and noting that for equilibrium times $\lambda_{\alpha,1} t \gg 1$, results in the corresponding decay rate, which indeed shows a linear dependence in ϕ_t

$$\lambda_{\alpha,1} N_{\alpha,1}(t) \to \Gamma_{linear} = \phi_t \vec{Z}_{\alpha,1} \cdot \vec{\Sigma}_{fiss} \propto \phi_t \tag{4.8}$$

where we have dropped the initial condition term $N_{\alpha,1_0} = 0$ as most reactors begin irradiation with a fresh batch (i.e. no fragments). The final expression of Eq. 4.8 illustrates that Γ_{linear} is governed, to first order, by the fission rate, i.e. the flux. Therefore, the beta-chain parent $N_{\alpha,1}$ is a linear nuclide and its decay and neutrino rate will be well-determined by the fission rate.

Connecting this conclusion to Fig. 4.1 shows that the region featuring the majority of beta-decays in a nuclear reactor (high decay rate and high fission yield) is highly correlated with the region of linear nuclides, which supports our earlier claim that most reactor antineutrinos are produced from linear nuclides. This also provides legitimacy for the traditional approach of converting the beta spectra of a thermal fission into an antineutrino spectra, a concept dating back to the late 1950s [190, 191], and applying these spectra to the fission rates of the major fissiles in a reactor as performed originally by Vogel [192]. However, it is demonstrated next that this general method will ignore the non-linear nuclides which have a negligible contribution in the widely-used Schreckenbach data, proven in Chp. 4.1.4, but will appear much more significantly in the reactors utilized by oscillation experiments.

Following the conclusion from Fig. 4.1, mainly that the beta-chain parent nuclide decay rates are linear in flux and can be given by Eq. 4.7, one can postulate that non-linear nuclides must then be daughters in these chains. These daughter nuclides are closer to the line of stability and will have longer halflives, allowing for comparable decay and neutron-capture rates. Here, the solution of the abundance equation for the i^{th} daughter $N_{\alpha,i}$ of a linear beta-decay chain parent $N_{\alpha,1}$, is are given by the solution to the Bateman equation in Eq. 4.2. Using the method of undetermined coefficients with

$$N_{\alpha-1,j} = \sum_{n=1}^{j} A_{\alpha-1,n} \exp[-\tilde{\lambda}_{\alpha-1,n}] + B_{\alpha-1,j} \quad N_{\alpha,i-1} = \sum_{n=1}^{i-1} C_{\alpha,n} \exp[-\tilde{\lambda}_{\alpha,n}] + D_{\alpha,i-1} \tag{4.9}$$

the generic form of $N_{\alpha,i}$ can be derived. The full derivation can be found in App. C. Recall that for the beta-chain parent it was proven that $\lambda_{\alpha,1} \gg \phi_t \sigma_{\alpha,1}$, which rendered the terms

proportional to $\phi_t\sigma_{\alpha,1}$ negligible and made $N_{\alpha,1}$ linear. Using this experience the non-linear correction terms in Eq. 4.10 can be readily identified.

$$N_{\alpha,i}(t) = \left[N_{\alpha,i_0}\right]e^{-\tilde{\lambda}_{\alpha,i}t} + \left[\frac{\phi_t\sigma_{\alpha-1,j}B_{\alpha-1,j} + \lambda_{\alpha,i-1}D_{\alpha,i-1} + \vec{Y}_{\alpha,i}\cdot\vec{\mathcal{F}}}{\tilde{\lambda}_{\alpha,i}}\right]\left(1 - e^{-\tilde{\lambda}_{\alpha,i}t}\right) + \left[\sum_{n=1}^{j}\frac{\phi_t\sigma_{\alpha-1,j}A_{\alpha-1,n}}{\tilde{\lambda}_{\alpha,i} - \tilde{\lambda}_{\alpha-1,n}}\left(e^{-\tilde{\lambda}_{\alpha-1,n}t} - e^{-\tilde{\lambda}_{\alpha,i}t}\right)\right] + \left[\sum_{n=1}^{i-1}\frac{\lambda_{\alpha,i-1}C_{\alpha,n}}{\tilde{\lambda}_{\alpha,i} - \tilde{\lambda}_{\alpha,n}}\left(e^{-\tilde{\lambda}_{\alpha,n}t} - e^{-\tilde{\lambda}_{\alpha,i}t}\right)\right] \tag{4.10}$$

Terms depending on the thermal neutron flux ϕ_t will be non-linear in nature as the undetermined coefficients will have some implied $\vec{\mathcal{F}}$-dependence, see the assignments for Eq. 4.7. In addition, the forms of $N_{\alpha-i,j}$ and $N_{\alpha,i-1}$ will need to be investigated to determine the specific dependences C, or D on ϕ_t as these may be non-linear.

To summarize, linear terms and nuclides have a decay rate depending on just the flux ϕ_t to first order. Non-linear terms and nuclides will have an additional explicit dependence on ϕ_t. This extra ϕ_t factor means that the integrated antineutrino flux of a non-linear nuclide depends not only on the end burnup of a reactor, as was the case for linear nuclides, but also on the specific irradiation history itself. For example, a non-linear nuclide may produce more antineutrinos in high flux reactors than in low flux reactors for the same total number of fissions. Linear nuclide antineutrino production is merely determined by the endpoint burnup and is insensitive to the 'fission path' taken by the reactor. For this reason it becomes crucial to quantify the antineutrino spectra from these non-linear nuclides as they may not been included in the Schreckenbach measurements [133–135] and corresponding conversion [83, 128] to calculate the total reactor antineutrino flux.

4.1.2 Non-linear nuclides in a nuclear reactor

Analyzing the reactor nuclides and the generalized Bateman equation yielded a group of possible non-linear candidates, those satisfying $\lambda \sim \phi_t\sigma$ and given as the black dots in Fig. 4.1. For the reactor antineutrino application, the most interest is in non-linear nuclides that beta-decay providing an antineutrino contribution. Some additional qualitative restrictions for our non-linear candidates are, thus, required. These are:

1. A large cumulative fission yield of a capture precursor isotope N_P
2. A large neutron capture cross section for N_P σ_P^c
3. The non-linear nuclide N_N must decay sufficiently quickly, that is the decay constant λ must be large enough
4. The beta-decay of the non-linear nuclide has to have an endpoint above the inverse beta-decay threshold of 1.8 MeV

Restriction (1) maximizes the impact of the non-linear nuclide N_N by requiring that its precursor N_P is produced in sufficient quantities. Restriction (2) ensures that the capture process of $N_P(n,\gamma)N_N$ will occur with sufficient frequency by increasing the value of σ_P^c. Restriction (3) then requires that once N_N is produced, it decays rapidly forcing it into equilibrium with the capture process $N_P(n,\gamma)N_N$, again boosting the impact of N_N. Restriction (4) ensures that our beta-decaying non-linear nuclides N_N can contribute to the reactor antineutrino spectrum in the detectable region of IBD detectors.

The list of our definitions for non-linear nuclides is designed to isolate an antineutrino source that would not be present in the early measurements of the fissile antineutrino yields, what will be referred to as the ILL experiments [133–135], which includes the Garching ^{238}U result. This will be quantitatively proven later, but for now a qualitative statement is made that if the non-linear beta-decaying nuclide N_N is fission blocked and its individual yield is negligible, then its only production method is neutron captures from a precursor N_P. If an experiment has too low of a thermal neutron flux, or too short of an irradiation time, this production method will be negligible and, thus, no non-linear antineutrino producers will appear in this experiment.

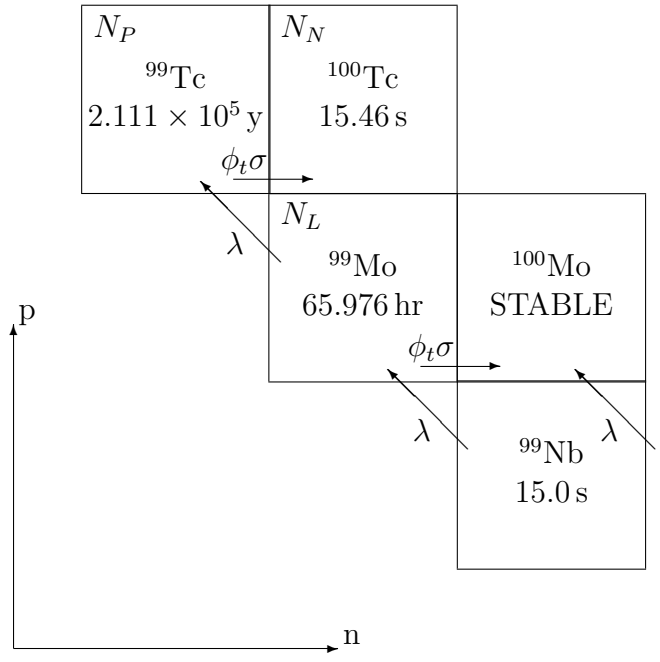

Figure 4.2: Example of a good non-linear beta-decaying nuclide (N_N), ^{100}Tc, and its accompanying precursor nuclide (N_P), ^{99}Tc, where ^{100}Tc is fission-blocked by ^{100}Mo. The cells include the nuclide ID and its halflife. Also included are the main production methods (arrows) and the long-lived precursor parent (N_L), ^{99}Mo. The beta-decay chain flows diagonally along the arrows and the neutron capture chain flows from left to right. Figure by author.

To provide a visual representation of our non-linear candidates we give Fig. 4.2. Here, we use the example of ^{100}Tc as our non-linear nuclide. It is only produced via neutron-captures on ^{99}Tc as it is blocked from the beta-chain by stable ^{100}Mo. Both the JEFF [125] and the LBL [185] yields show negligible yields for ^{100}Tc, below $\mathcal{O}(10^{-6})$ atoms/fission, which ensures ^{100}Tc will not have a linear component. For this analysis and all reactor designs, nuclides with hafflives above 10^3 y are effectively stable, so ^{99}Tc is deemed stable. The nuclear parameters for our non-linear candidates are provided in Tab. 4.1, where it is observed that conditions (1-4) are met. Visually, non-linear nuclides will follow the layout of Fig. 4.2, which, after inspecting the various fragment yields, result in ~ 30 nuclides.

Also included in Fig. 4.2 is the long-lived precursor parent N_L. The impact of this nuclide has a very interesting effect on the non-linear production, where it acts as a sort of resistor in the generic non-linear series $N_L \to N_P \to N_N$, but its impact will be shown later.

After searching through all nuclides in the fission yield databases, many non-linear candidates that resemble the layout of Fig. 4.2 are found. Using the restrictions above and a helpful set of visuals, which compare the antineutrino spectra, calculated via Ref. [128] and the cumulative yields via JEFF [125], reduces this list to 4 nuclides. An interesting side note is that all four non-linear nuclides are blocked by a double beta-decaying isobar. Two examples of these visuals are given as Fig. 4.3. These visuals allow one to easily eliminate some of

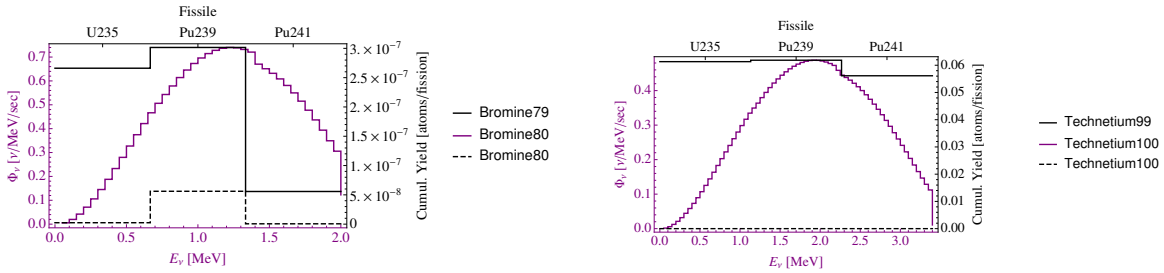

Figure 4.3: A visual providing some of the necessary parameters for determining good non-linear nuclides in a reactor. The neutrino spectrum, calculated by Huber [128], is given in purple for the beta-decaying non-linear N_β (^{80}Br or ^{100}Tc). Also provided (in black) are the cumulative fission yields from JEFF [125] for the feeder N_F (^{79}Br or ^{99}Tc) and for the non-linear candidate. Figures by author.

the possible non-linear candidates. Using the left figure for ^{80}Br, note that the cumulative yields for the precursor are small, violating restriction (1). In addition, the fission yields of the non-linear candidate ^{80}Br are comparable to its precursor ^{79}Br for ^{239}Pu fissions, which provides it with a linear component. Finally, note that while the beta endpoint E_0 is above IBD threshold (~ 1.8 MeV), it is only just barely so for ^{80}Br. These factors combine to make ^{80}Br a weak non-linear candidate.

On the right, there is ^{100}Tc, which has negligible fission yields across all fissiles, a beta endpoint far above IBD, and a sizable cumulative precursor yield. Additionally, the precursor is effectively stable (see Fig. 4.2) for reasonable reactor irradiation times, and the cross-section for ^{99}Tc(n,γ)^{100}Tc is large (~ 20 b). These qualities make ^{100}Tc a very good non-linear candidate. Using similar criteria and visuals the 4 excellent non-linear candidates are located and their properties are presented in Tab. 4.1.

		^{100}Tc	^{104}Rh	^{110}Ag	^{142}Pr
N_N E_0 (MeV)		3.2	2.45	2.9	2.2
N_N $\tau_{1/2}$ (sec)		15.5	42.3	24.6	68800
N_P Cumul. Fission Yields (atoms/fiss.)	^{235}U(522b)	0.061	0.031	2.90×10^{-4}	0.059
	^{239}Pu(698b)	0.062	0.069	0.017	0.052
	^{241}Pu (950b)	0.056	0.065	0.030	0.049
N_P σ_t^c (b)		17.0	127	80.9	6.53
N_L $\tau_{1/2}$ (d)		2.75	39.3	0.57	32.5
N_L σ_t^c (b)		1.57	7.08	18.2	26.7

Table 4.1: Properties of the four selected non-linear nuclides including their cumulative precursor fission yields [atoms/fission], beta endpoints (MeV), halflives (sec), and their feeder flux-averaged thermal cross-section (b) taking the thermal flux from Fig. 3 of Ref. [193] and the cross-sections from CINDER [186]. Also provided are the long-lived precursor parent cross-sections (b) and halflives (d).

There are other qualities that make certain non-linear candidates able to distinguish the nuclide being fissioned. For example, ^{110}Ag is dominantly produced in plutonium fissions (primarily ^{241}Pu) meaning it is sensitive to the plutonium grade. Plutonium grade is a measure of the fraction of ^{239}Pu to the other isotopes, weapons-grade containing $\geq 93\%$ ^{239}Pu [175], and is an important non-proliferation concept discussed in Chp. 5.

Table 4.1 calculates the thermal group-averaged cross-sections using the thermal neutron flux from Fig. 3 of Ref. [193] and the cross-sections from the CINDER library [186]. This method is also used for the fissile cross-sections. With these parameters and the analytic technique of solving our generalized Bateman equations, the abundance of the 4 non-linear nuclides can be calculated in a reactor environment, using Eq. 4.7 and Eq. 4.10 to our specific non-linear layout of Fig. 4.2, performed next.

4.1.3 Analytical solution to non-linears

Four specific non-linear nuclides have now been identified and their nuclear parameters are known. These parameters can be applied to the expressions for the parents and daughters of beta-decay chains to solve for the non-linear abundance. This can then be converted to an activity and, finally, a neutrino spectra. First, a re-examination of Fig. 4.2 determines that each non-linear nuclide will be governed by a set of 3 Bateman equations, one for N_L, one for N_P, and one for N_N. Starting the beta-chain with N_P will ignore the large halflives of N_L, see Tab. 4.1, which must be avoided.

The Bateman equations for any given non-linear set is represented by the three linear non-homogeneous coupled differential equations:

$$\begin{aligned}\frac{dN_L}{dt} &= \vec{Z}_L \cdot \vec{\mathcal{F}} - \tilde{\lambda}_L N_L \\ \frac{dN_P}{dt} &= \vec{Y}_P \cdot \vec{\mathcal{F}} + \lambda_L N_L - \phi_t \sigma_P N_P \\ \frac{dN_N}{dt} &= \phi_t \sigma_P N_P - \lambda_N N_N\end{aligned} \tag{4.11}$$

where the fact that $\vec{Z}_L \cdot \vec{\mathcal{F}}$ is the dominant producer of N_L, or N_L is linear, from the arguments of Chp. 4.1.1 is used. Thus, N_L is produced via the cumulative fission yields $\vec{Z}_L$ and destroyed via its neutron captures and decays $\tilde{\lambda}_L$. Then, the precursor nuclide N_P is produced via decays of N_L and fission, but the individual yields $\vec{Y}_P$ must be used, as its cumulative growth will already be accounted for in the $\lambda_L N_L$ term. The stable precursor is destroyed only through its own neutron captures, where ϕ_t and σ_P are taken to be the group-averaged flux and (n,γ) cross-section for thermal energies. Lastly, N_N, the non-linear antineutrino producer, is only generated via neutron captures on N_P and destroyed via its own decays. Accounting for the neutron captures on N_N is a negligible effect, as the decay rates are much greater than the capture rates.

This set as already been solved. The first differential equation in Eq. 4.11, given by Eq. 4.7, but is reproduced in terms of the nuclear parameters of N_L, N_P, and N_N. In addition, the second differential equation has been solved as Eq. 4.10 with the simple replacements of $\tilde{\lambda}_{\alpha,i} \rightarrow \phi_t \sigma_{\alpha,i}$ and $\sigma_{\alpha-1,j} = 0$, as the growth of N_P is dominated by its parent N_L. Finally, the third differential equation is another version of Eq. 4.10 with $\tilde{\lambda}_{\alpha,i-1} = 0$ and $\vec{Y}_{\alpha,i} = 0$. Therefore, the solutions to Eq. 4.11 are given by:

$$N_L(t) = \left[\frac{\vec{Z}_L \cdot \vec{\mathcal{F}}}{\tilde{\lambda}_L}\right]\left(1 - e^{-\tilde{\lambda}_L t}\right) \tag{4.12}$$

$$N_P(t) = \left[\frac{\lambda_L \vec{Z}_L \cdot \vec{\mathcal{F}} + \tilde{\lambda}_L \vec{Y}_P \cdot \vec{\mathcal{F}}}{\phi_t \sigma_P \tilde{\lambda}_L}\right]\left(1 - e^{-\phi_t \sigma_P t}\right) - \left[\frac{\lambda_L \vec{Z}_L \cdot \vec{\mathcal{F}}}{\tilde{\lambda}_L(\phi_t \sigma_P - \tilde{\lambda}_L)}\right]\left(e^{-\tilde{\lambda}_L t} - e^{-\phi_t \sigma_P t}\right) \tag{4.13}$$

$$N_N(t) = \left[\frac{\tilde{\lambda}_L \vec{Y}_P \cdot \vec{\mathcal{F}} + \lambda_L \vec{Z}_L \cdot \vec{\mathcal{F}}}{\tilde{\lambda}_L \tilde{\lambda}_N}\right]\left(1 - e^{-\tilde{\lambda}_N t}\right) + \left[\frac{\lambda_L \phi_t \sigma_P \vec{Z}_L \cdot \vec{\mathcal{F}}}{\tilde{\lambda}_L(\tilde{\lambda}_L - \phi_t\sigma_P)(\tilde{\lambda}_N - \tilde{\lambda}_L)}\right]\left(e^{-\tilde{\lambda}_L t} - e^{-\tilde{\lambda}_N t}\right) - \left[\frac{(\tilde{\lambda}_L - \phi_t\sigma_P)\vec{Y}_P \cdot \vec{\mathcal{F}} + \lambda_L \vec{Z}_L \cdot \vec{\mathcal{F}}}{(\tilde{\lambda}_L - \phi_t\sigma_P)(\tilde{\lambda}_N - \phi_t\sigma_P)}\right]\left(e^{-\phi_t\sigma_P t} - e^{-\tilde{\lambda}_N t}\right) \tag{4.14}$$

where all initial conditions are assumed to be zero (a fresh reactor core at $t = 0$) and all nuclear parameters (decay constants λ, cross-sections σ, and yields $\vec{Z}$ and $\vec{Y}$) are identified by their subscript. This set of equations, derived in full detail in App. C, illustrates the linear nature in Eq. 4.12 and the complete non-linear nature of Eq. 4.14. For example, setting $\sigma_P = 0$ renders all production of N_N to zero identically. We also note that Eq. 4.13 is linear for $\phi_t\sigma_L \ll \lambda_L$ and non-linear for $\phi_t\sigma_L \sim \lambda_L$.

These equations and the information given in Tab. 4.1 can be used to determine the limiting cases for non-linear production. For irradiation times much shorter than the halflives of the long-lived feeder parent N_L, the production of N_P is severely reduced as not enough atoms have decayed from $N_L \to N_P$, yet. The N_L halflives range from $0.57 - 39.3\,\mathrm{d}$, comparable or $\sim \times 20$ larger than the experiment times of the ILL measurements [133, 134]. This supports the result of a highly suppressed non-linear correction in these short irradiation experiments. Another case of short irradiation periods comes with the calculation of the High Flux Isotope Reactor (HFIR), modeled by Dan Ilas [194] and reproduced in Chp. 4.1.4 next, via SCALE. The HFIR reactor has the highest publicly-available steady-state neutron flux of $2.5 \times 10^{15}\,\mathrm{n/cm^2/sec}$. However, this reactor is irradiated in cycles at a maximum length of $20\,\mathrm{d}$. Therefore, despite its large ϕ_t, the HFIR reactor will have a suppressed non-linear correction. All other calculations that are made will involve irradiation cycles $\geq 250\,\mathrm{d}$, long after N_L reaches equilibrium. Therefore, we conclude that reactors with irradiation cycles $\leq 30\,\mathrm{d}$ will have suppressed non-linear corrections, irrespective of their thermal neutron fluxes.

The next limiting case is the thermal neutron flux. One can see diagrammatically, from Fig. 4.2, that extremely high neutron fluxes will pull atoms from the $N_L \to N_P \to N_N$ chain via $N_L + n$ neutron capture to the stable blocker. A critical flux ϕ_t^{crit} that 'turns off' the non-linear correction can be solved for by determining when $\phi_t^{\mathrm{crit}}\sigma_L \sim \lambda_L$. Using Tab. 4.1, it is found that ϕ_t^{crit} ranges from 9.25×10^{15} to $1.86 \times 10^{18}\,\mathrm{n/cm^2/sec}$ for the four non-linear nuclides. As these are $\sim 1 - 3$ orders of magnitude larger than the current reactor limits, we can confidently state that these 'turn-off' fluxes will not be reached in our simulations.

For the majority of the reactor considerations, the irradiation time will be large enough to allow equilibrium in the N_L nuclides. The beta-decaying non-linear nuclides rapidly decay (in seconds to hours) meaning that they will always be in equilibrium with their production mechanism for irradiation times longer than the N_L halflives. Thus, the decay rate for N_N

will be given, roughly, by

$$\Gamma_{\text{non-linear}} = \underbrace{\vec{\Sigma}_t^{\text{fiss}} \cdot \vec{Z}_P \phi_t T_{\text{irr}}}_{\text{atoms N}_P} \sigma_P \phi_t \propto T_{\text{irr}} \phi_t^2 \tag{4.15}$$

where the macroscopic fission cross-section of the fissiles, $\vec{\Sigma}_t^{\text{fiss}}$, multiplied by the thermal neutron flux ϕ_t produces the fission vector $\vec{\mathcal{F}}$. Noting that Eq. 4.15 illustrates a non-linear production dependence on $\phi_t^2 T_{\text{irr}}$ illuminates why these nuclides are indeed dubbed as 'non-linear' and supports our non-linear claim at the beginning of this chapter.

Utilizing the T_{irr} limiting case we can do a quick comparison between our simplified non-linear analytical calculation and the simulation-based calculation. For this comparison, irradiation times and thermal neutron fluxes are chosen that fall well within the critical values found earlier. A calculation of the abundance of the precursor nuclide is computed in the realm of N_L equilibrium, so that N_P represents the parent nuclide. The analytical calculation for the

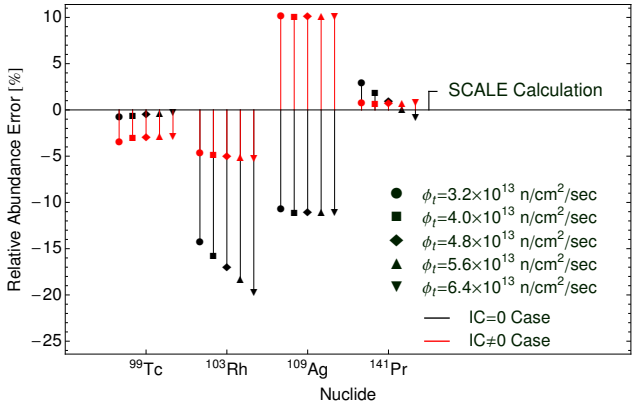

Figure 4.4: Comparison of the analytical and SCALE-calculated precursor nuclide abundance for 1-batch PWR calculation. Two analytical methods are tested. The first attempts to calculate the N_P abundance at the end of 3 irradiation cycles with no shutdowns or initial conditions (black). The second attempts to calculate the same, but uses the initial conditions at the start of each cycle to simulate a shutdown (red). All calculations are made with the same fluence $\phi_t T_{\text{irr}} \simeq 4.30 \times 10^{16}\,\text{n/cm}^2$. Figure by author.

N_P abundance compared with that of SCALE for a 1-batch PWR irradiated for three cycles is given by Fig. 4.4. We note that equal fluences were considered with $\phi_t T_{\text{irr}} = 4.30{\times}10^{16}\,\text{n/cm}^2$. Thus, if any of the precursors were non-linear it would be evidenced as a flux-dependence. The analytical computations are accurate to about ±20% when an attempt is made to analytically solve for the abundance of N_P at the end of the third cycle. This method (black) skips the shutdowns between each cycle as computed with Origen-S, meaning that it ignores the initial conditions ($IC = 0$). On the other hand, if the initial conditions at the start of each irradiation cycle are used (red), the analytical prediction is accurate to within ±10% and shows no non-linear tendencies for N_P.

With this comparison it becomes obvious that the incorporation of shutdowns and, for that matter, a detailed reactor simulation, is important. One critical note is that the errors seem to be flux-dependent in the $IC = 0$ case, but lose this dependence in the $IC \neq 0$ case. This is important as our calculations will rely on having low errors even for high fluxes in the N_P production, as it is directly related to the non-linear decay rate, see Eq. 4.15. All future simulations will be computed with shutdowns to ensure the highest accuracy. The simulations will be outlined in the next section.

Now that an analytical solution to the non-linear nuclide production exists and the accuracy of said analytical expression is sufficient, the antineutrino spectra for the four non-linears can be used to generate the non-linear antineutrino contribution. These spectra are given by Fig. 4.5 and are computed via Huber [128]. Therefore, one can simply apply the antineutrino

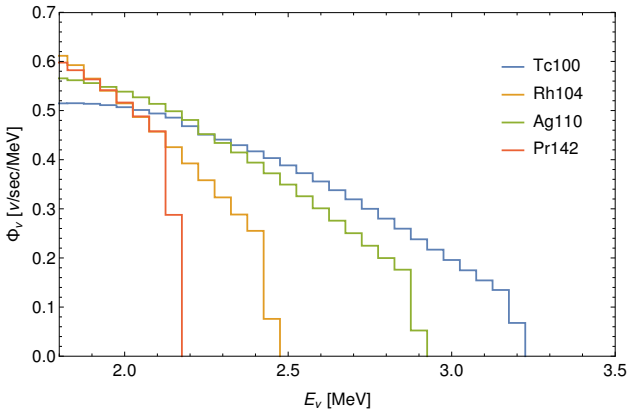

Figure 4.5: Neutrino spectrum for the four major non-linear nuclides: ^{100}Tc, ^{104}Rh, ^{110}Ag, and ^{142}Pr. The spectra are cut above IBD threshold and are computed via Ref. [128]. Figure by author.

spectra of Fig. 4.5 to the activities trivially acquired from Eq. 4.14 (via $\alpha_N(t) = \lambda_N N_N(t)$) to generate the total antineutrino signal from non-linear nuclides. This spectrum will be completely independent of the ILL-calculated reactor spectrum and, thus, constitutes a correction to the reactor antineutrino spectrum. Next, a full reactor simulation is used to generate the correction size.

4.1.4 Computational calculation of non-linear correction

In this section our procedure is outlined to determine the non-linear correction over several orders of magnitude for ϕ_t and T_{irr} with accurate reactor simulations generated by SCALE [145]. A total of ten experiments, six of them being actual reactor calculations and the remaining four representing the famous ILL measurements, are computed. The details of all reactor simulations will be outlined next. Three of these simulations will be used and

discussed in the non-proliferation application, found in Chp. 5 and another one has been the focus of Chp. 3.

The first in the simulation list is a natural uranium loaded and graphite-moderated reactor, similar in design to the British Calder-Hall reactor. This reactor is referred to as the $5\,\mathrm{MW_e}$ reactor and has been previously modeled [3]. The next reactor uses natural uranium as fuel and heavy water as a moderator, similar in design to the CANDU reactors. This reactor, referred to as the IR40, has also been previously modeled [5]. The third reactor is fueled with low-enriched uranium (LEU) and has a water moderator. These reactors are pressurized water reactors (PWR) similar in design to the Daya Bay cores. The Daya Bay reactors have also been previously modeled to estimate the spent fuel contribution [2], detailed in Chp. 3. The PWR cores are simulated using a 3-batch method, where a full core consists of 3 parts: a third each of fresh, once-irradiated, and twice-irradiated fuel. A single-batch calculation is included for comparison. Next, a research reactor, named the IRT reactor, is simulated, which is a pool-type reactor using highly-enriched uranium (HEU) fuel elements, natural uranium target elements, and water as a moderator. It was previously simulated, also in Ref. [3]. The measurements conducted at the ILL and Garching are also reproduced, irradiating a fissile mass with a specific neutron flux according to Ref. [133–135]. Finally, the HFIR at Oak Ridge National Laboratory, which represents the highest steady-state neutron flux commercially available, is simulated. Our simulation closely follows that of Ref. [194].

Each reactor in this list is irradiated according to its typical power history, which have been acquired from various sources [133–135, 174, 194–196]. These simulations utilize multiple subroutines of the SCALE suite depending on the simulation difficulty. For example, the IR40, IRT, and HFIR reactors all required uniquely designed core cross-section libraries so subroutines such as NEWT (a 2d neutron transport code), Triton (a depletion code coupled with NEWT), and Keno-VI (a 3d transport code), in addition to the aforementioned Origen-S depletion method, have been utilized. A summary of the burnups and reactor designs are given in Tab. 4.2.

After producing the cross-section libraries for the various reactors, Origen-S is used to determine the composition of the reactor during its irradiation cycle. This composition includes the fission rates for the four main fissiles and the physical abundance of the non-linear nuclides ^{100}Tc, ^{104}Rh, ^{110}Ag, and ^{142}Pr at all time steps. The familiar fissile antineutrino yields, measured as a beta-spectrum by Schreckenbach [133, 134], and converted by Huber [128] (summarized in Tab. A.1 - A.4 in App. A) are used to calculate the total reactor spectrum (Φ_{Rx}) without any non-linear contribution. Then, the antineutrino spectra of Fig. 4.5 is applied to the activity of the non-linear nuclides given by the final Origen-S calculation to represent the non-linear contribution (Φ_{NL}). Both the total reactor spectrum and non-linear spectrum are binned into 250 keV bins starting at 2.0 MeV and the non-linear correction is determined from the ratio of $\Phi_{NL}(t,E)/\Phi_{Rx}(t,E)$ for each energy bin and time step during the irradiation cycle. This result is then used to calculate the time-averaged non-linear correction over the entire irradiation period as outlined in Eq. 4.16.

$$C(E) = \int_0^{T_{\rm irr}} \frac{\Phi_{NL}(E,t)}{\Phi_{Rx}(E,t)} dt \tag{4.16}$$

As ^{238}U fissions comprise a small number of fissions and contain a larger error on their neutrino spectrum [135], they are neglected.

	$5\,\mathrm{MW_e}$	IR40	PWR		IRT	ILL			HFIR
			1-batch	3-batch		^{235}U	^{239}Pu	^{241}Pu	
Fuel/Moderator	NU+C	NU+D_2O	LEU+H_2O		HEU+H_2O	HEU+D_2O			HEU+H_2O
Burnup [MWd]	32380	31200	31510	1890000	2230	7.3×10^{-5}	1.1×10^{-4}	1.7×10^{-4}	2550
ϕ_t [n/cm^2/sec]	1.6×10^{12}	3.6×10^{13}	4.4×10^{13}	4.4×10^{13}	1.5×10^{14}	3.3×10^{14}	3.3×10^{14}	3.3×10^{14}	2.5×10^{15}
Max[$\langle\Phi_{\rm NL}/\Phi_{\rm R}\rangle_T$] [%]	2.7×10^{-1}	0.15	0.25	0.93	0.11	3.1×10^{-5}	2.6×10^{-3}	4.7×10^{-3}	0.10

Table 4.2: Details of the reactor calculations via Origen-S including the burnup, thermal neutron flux, and design details. The burnup calculations for the PWR cores and IRT have been separated into their individual batches and elements, respectively. The maximum cycle-average non-linear correction given is the conservative lower bound from the ILL errors [128].

Examining Fig. 4.5 and the total reactor spectrum (given by $\tau = 0\,\mathrm{d}$ in Fig. 3.3) indicates that the highest non-linear to reactor antineutrino ratio will occur in the lowest energy bins. Thus, the maximum time-averaged correction, as given by Tab. 4.2 and determined by Eq. 4.16 will always lie in the $2.0 - 2.25\,\mathrm{MeV}$ bin. The results show that the commercial PWRs can be quite sensitive to the non-linear correction ($\sim 1\%$), where this becomes comparable with the spent nuclear fuel ($1-3\%$), see Chp. 3 and non-equilibrium effects ($1-4\%$) [197, 198]. Therefore, neutrino experiments hoping to utilize reactors as their source will need to take this correction into account and perform reactor simulations to do so. Again, the emphasis is made that all three of these corrections appear in the low-energy region of the antineutrino spectrum, directly impacting geoneutrino searches via reactor subtraction [172, 173].

A comparison of the analytical and computational methods was conducted to ensure that the physics of the non-linear effect is accurately represented. For this, the fluxes and irradiation times given for each reactor were used to compute the activity of each non-linear nuclide via Eq. 4.14. After applying the neutrino spectra of Fig. 4.5, the ratio of non-linear to total reactor antineutrino flux is calculated across all energy bins. The total reactor flux was computed with the fissile antineutrino yields and the fission rates provided by the simulations. Finally, this ratio was time-averaged over the given irradiation cycle and found to agree with the pure SCALE method within a factor of 3 for all reactors. The ILL calculations see the most discrepancy between analytical and computational approaches, with the PWR 3-batch and 1-batch estimates following behind.

An item of note here is the calculation of the famous ILL measurements, which determined the beta spectrum of three main fissiles by Schreckenbach *et al.* and ^{238}U by Haag *et al.* have utilized a research reactor with an output neutron flux $\phi_t \simeq 3.3\times10^{13}\,\mathrm{n/cm^2/sec}$ and

irradiation times of 12 hr, 36 hr, 43 hr, and 42 hr for ^{235}U, ^{239}Pu, ^{241}Pu, and ^{238}U, respectively in accordance with Ref. [133–136, 199]. Not listed in Tab. 4.2, due to its large errors, is our calculation of the cycle-averaged non-linear correction to the ^{238}U spectrum measurement, a value of $\mathcal{O}(10^{-6})\%$. Therefore, it is concluded, as promised, that the ILL measurements are completely insensitive to the non-linear correction. This is of paramount importance, ensuring that the beta-conversion techniques of Huber [128] and Mueller [83], used by nearly every reactor neutrino experiment today, remains accurate.

The non-linear correction is given visually as Fig. 4.6 where we plot the size of the correction as a series of dots with their corresponding total irradiation time T_{irr} and thermal neutron flux ϕ_t. These values are the same as those given in Tab. 4.2, where we conservatively take the correction lower bound from the ILL errors, given as $\sim 2.0, \sim 2.5, \sim 2.5\%$ for ^{235}U, ^{239}Pu, and ^{241}Pu [128] for the lower energy bins.

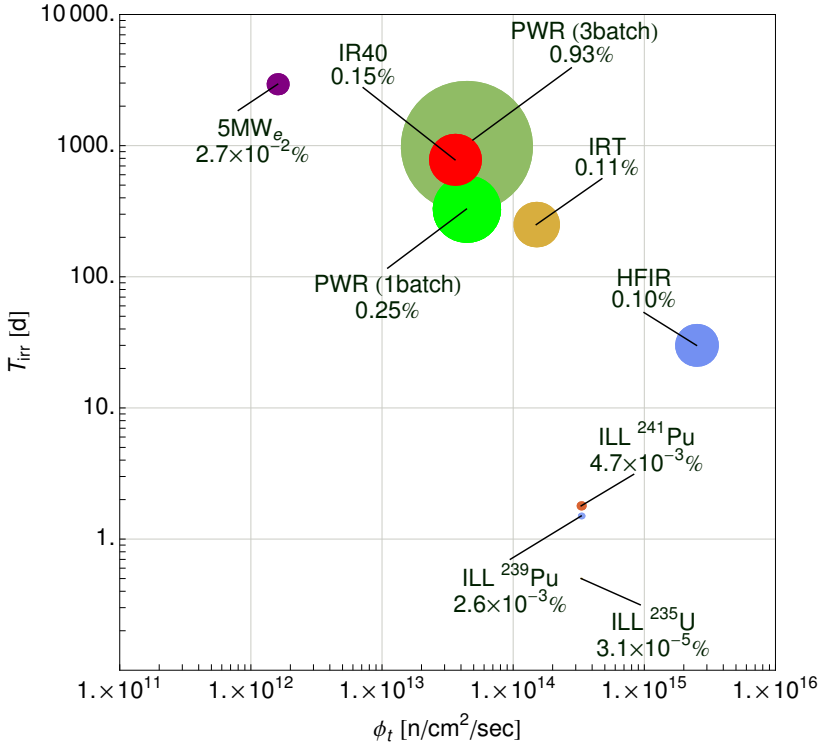

Figure 4.6: Correction sizes for the non-linear effect as computed in nine different reactor configurations. The size of the correction is listed along with the reactor identifier (see Tab. 4.2 for reactor details). Figure courtesy of Ref. [1].

Figure 4.6 illustrates the interesting physics behind the non-linear effect. Here, it is seen that there is a 'sweet' spot for maximizing the non-linear contribution at some ϕ_t value not too large to promote neutron captures on N_L, but large enough to supply neutron captures to N_N. Also apparent is the preference for longer irradiation times. The familiar ILL measurements

show completely negligible non-linear corrections, but reactors with high burnups, such as the 3-batch PWR, show a much larger non-linear correction. Both of these characteristics support the conceptual understanding and the analytical derivation of the non-linear correction. A simulation was conducted on the HFIR reactor to long irradiation times ($\sim 70\,\mathrm{d}$) and it was found that this reactor rapidly approaches the $\mathcal{O}(1\%)$ cycle-averaged non-linear correction as expected. However, this length of T_{irr} is completely unphysical for the HFIR design. One last conclusion is that reactors with large ϕ_t and extremely large burnups, such as naval reactors, could experience enormous non-linear corrections. For example, the analytical method estimates a $5\,\mathrm{y}$ running of a $165\,\mathrm{MW_t}$ HEU reactor, typical of naval submarines, would reach a non-linear correction of $\sim 4\%$. Thus, the non-linear correction is not negligible and could be even larger in high-T_{irr}, high-ϕ_t reactors requiring experiment-specific reactor simulations.

4.2 Non-linear Conclusion

This chapter has introduced a new reactor antineutrino correction, which we name the non-linear correction. It originates from nuclides whose primary production method is via neutron captures on stable isotopes. After a comprehensive examination of the fission fragments produced in a reactor, our search converged on 4 non-linear nuclides of interest: ^{100}Tc, ^{104}Rh, ^{110}Ag, and ^{142}Pr, all blocked from the fission chain by $\beta\beta$ nuclides. An analytical expression for the size of this correction was derived via Bateman equations. After verifying this expression with reactor simulations, provided by SCALE [145], it was determined that non-linear nuclides are produced in very low quantities for small T_{irr} and small ϕ_t reactors. Thus, this correction is independent of the ILL measurements [133–135] and corresponding conversions [83, 128], which is shown in Fig. 4.6.

Spanning nearly 3 orders of magnitude in reactor thermal flux and more than 3 orders of magnitude in irradiation time, a series of reactor simulations using various subroutines of SCALE found that the cycle-averaged non-linear correction can be as large as $\sim 1\%$ for commercial reactors. A comparison of the analytical and computational approaches resulted in reasonably similar non-linear corrections. The locations and sizes of the SCALE-calculated corrections seem to match nicely with the trend of the analytically-computed non-linear activity in Fig. 4.6. For these reasons, it can be confidently stated that the physics of the non-linear correction as we have described throughout this chapter are sound.

This non-linear correction is again found in the low-energy region of the reactor antineutrino spectrum and, thus, poses a problem for precision neutrino measurements. As concluded in Chp. 3, the NL correction ($\leq 1\%$) for a commercial PWR, where many neutrino oscillation studies are based, combined with the SNF correction ($1-3\%$) and the NE effect ($1-4\%$) can influence the observed to expected ratio of antineutrino events in the low energy bins, currently below unity and providing strong evidence for sterile neutrinos [81]. The addition

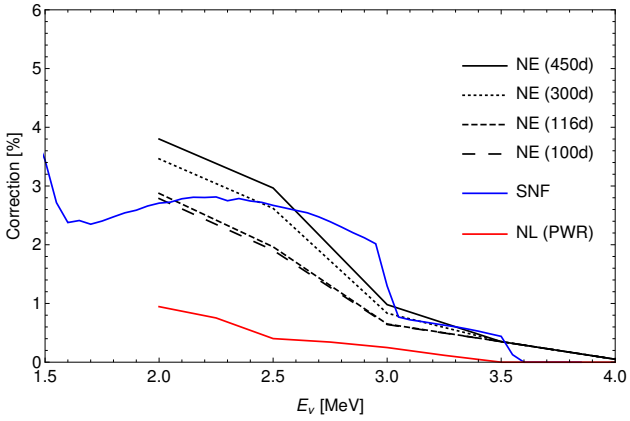

Figure 4.7: Comparison of the non-linear (red) and spent nuclear fuel (blue) correction with the non-equilibrium (black) correction calculated by Mueller *et al.* [83] for four different irradiation times. All corrections are with respect to a PWR-like commercial reactor. The NL correction is slightly smaller than the SNF and NE corrections, but still in the $\sim 1\%$ window of the total reactor signal. This NL correction assumes a 3-batch core, utilized by almost all commercial reactors, and is time-averaged over a typical irradiation cycle. Figure by author.

of the NL correction provides yet another $\sim 1\%$ reduction to the low-energy antineutrino spectrum. Again, the θ_{13} oscillation searches occur in these low-energy bins as well, making the non-linear correction a non-trivial source of error. Currently, the use of several baselines removes this error sources, but would be problematic for single detector applications.

In addition, these corrections in the low-energy bins, now amounting to $3 - 8\%$, will make geoneutrino measurements based on reactor subtraction [172, 173] immensely difficult. A dedicated antineutrino experiment, such as a short-baseline detector [71, 162, 200], may be necessary to fully quantify all of the corrections presented in this work and elsewhere [83] with a combined experimental and computational approach.

Chapter 5

Nuclear Safeguards with Reactor Antineutrinos

This chapter provides an exploration of the viability and limits of antineutrino detectors as a method of monitoring nuclear reactors. In it, the goals of non-proliferation are introduced and a brief history of reactor monitoring via antineutrinos is provided. The first test of antineutrino safeguards utilizes the historic case of the North Korean nuclear crisis of 1994. The highlights of the historical scenario are provided and it is determined how antineutrino-based monitoring would perform in comparison to conventional safeguards methods. Primarily, a measurement of the antineutrino rate is linked to the reactor power and a spectral measurement to the plutonium content. The next project focuses on a current-events issue of safeguards, mainly the Iranian heavy water reactor located near Arak. Antineutrino monitoring capabilities are discussed for this reactor as well. Lastly, a complete summarization of the status of antineutrino safeguards and the advantages they bring is given.

The analysis and results of this research is presented in Ref. [3] and Ref. [5]. The research presented next provides a brief introduction to the historical significance and provides more information on the reactor simulation and statistical analyses used to derive the limits of antineutrino safeguards.

5.1 Safeguards Introduction

As discussed in Chp. 2, nuclear reactors are a copious source of electron antineutrinos. The same small interaction cross-section that makes neutrinos so difficult to detect experimentally also provides them with unusually large penetrating power. Currently, there are no practical methods of shielding or attenuating neutrinos, meaning the information they carry is secure. For this reason, it became apparent, first to Borovoi and Mikaelyan in 1978 [66], that antineutrinos could be used to monitor nuclear reactors. Since this first inception, many

attempts have been made to quantify the feasibility of reactor antineutrino monitoring, both in theory [201–203] and experiment [70,163,204]. This technology is of special interest to the International Atomic Energy Agency (IAEA) and the international community as a whole because it allows for a means of preventing the spread of nuclear material. Indeed, it was widely held in 1970, when the Non-proliferation Treaty (NPT) [205] was enacted, and still today, that a larger number of nuclear parties is more dangerous.

> *The States concluding this Treaty [...] Believing that the proliferation of nuclear weapons would seriously enhance the danger of nuclear war [...] call[ing] for the conclusion of an agreement on the prevention of the wider dissemination of nuclear weapons.* –Treaty on the non-proliferation of nuclear weapons

For this reason, the work presented in this chapter represents a detailed investigation into the feasibility of antineutrino safeguards in an attempt to support the non-proliferation of nuclear weapons. A focus is made on historical events and real reactor simulations to provide the most realistic measures of the benefits and limitations of this unique application of neutrinos. Chp. 5.2 is replicated in Ref. [3] and Chp. 5.3 is given in Ref. [5]. Next, basic monitoring techniques and the statistical calculations used in the safeguards examples are outlined.

Basic monitoring relies on the link between two antineutrino properties to two reactor parameters: 1) the absolute rate of antineutrinos is directly related to the reactor power and 2) the spectral shape is a measure of the fission vector. Both concepts will be described next. Most nuclide decay rates in the reactor environment are linear in flux, a claim defended in Chp. 4.1.1, which leads to an antineutrino rate linear in flux. Reactor power is directly related to the neutron flux via

$$P_{th} = \sum_{f}^{N_f} \mathcal{F}_f \kappa_f = \sum_{f}^{N_f} \phi_t \Sigma_f \kappa_f \tag{5.1}$$

where the thermal power P_{th} is given by the weighted sum of the fission rates $\mathcal{F}_f$ of each fissile f with the energy yield per fission κ_f, taken from Kopeikin [122]. The fission rates can be expressed as the thermal neutron flux ϕ_t multiplied by the macroscopic cross-sections for each fissile Σ_f, which reveals a linear relation between reactor power and flux[1]. Finally, as both the antineutrino rate and reactor thermal power are linear in ϕ_t, it can be concluded that power and antineutrino rate are also linearly related. Therefore, a measurement of the antineutrino rate yields the reactor power, a feat first demonstrated by Korovkin [68] at a Soviet VVER-440 reactor.

Conversions of the beta-spectra performed by Huber [128], Mueller [83], and Fallot [206] for the major fissiles measured at ILL (^{235}U, ^{239}Pu and ^{241}Pu) [133,134] and Garching (^{238}U) [135] have shown that each fissile has a different antineutrino yield $N_\nu^f(E)$. It should be noted

[1]Technically, Eq. 5.1 should include epithermal and fast fissions, especially for ^{238}U

that the absolute values for the fissile yields differ between the various conversion models. However, the relative differences between that of ^{235}U and the three other main fissiles are almost equivalent among the various models. In other words, while the models may derive

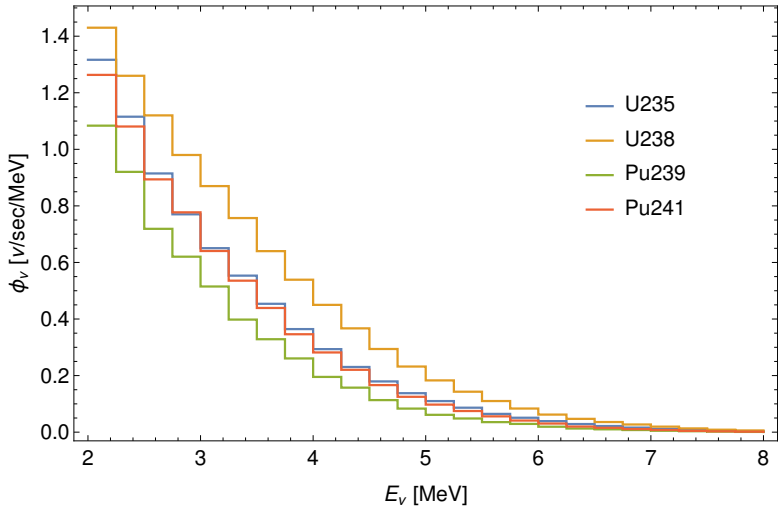

Figure 5.1: Fissile electron antineutrino event rate for each of the four major fissles. The yields of ^{235}U, ^{239}Pu, and ^{241}Pu are taken from Ref. [128] and the yields of ^{238}U are taken from Tab. III of Ref. [83]. All are binned in 250 keV bins and are normalized to one ν per fission. Figure by author.

different mean antineutrino energies and overall rates, they all agree on how the antineutrino spectra varies from fissile to fissile. Plotting these antineutrino yields in 250 keV bins and integrating over the νp cross-section illustrates this concept. Figure 5.1 shows that ^{239}Pu has a much 'softer' antineutrino event spectrum than the other major fissiles. Therefore, if one can measure the spectral shape accurately, the relative contributions from each of the four main fissiles can be estimated via a χ^2 minimization between the true event spectrum measured and the reproduced event spectrum composed as a linear sum of the individual fissile components

$$R_\nu(E) = \sum_f \mathcal{F}_f N_\nu^f(E) \tag{5.2}$$

where the fission rates $\mathcal{F}_f$ weight the fissile antineutrino yields $N_\nu^f(E)$ for a fissile f and $N_\nu^f(E)$ will be given by Fig. 5.1, for example.

5.1.1 Determining the Core Composition

The differences seen between the various fissiles in Fig. 5.1 is critical to reactor monitoring as it allows for a measurement of both the core evolution and content. Recall that as a nuclear reactor runs, it will transmute ^{238}U into plutonium isotopes, such as ^{239}Pu with one neutron

capture and ^{241}Pu with three, in a process given the name burnup[2]. Therefore, a reactor that burns longer will typically have a more plutonium-dominated fission vector producing a softer spectrum. Reactors that use mixed-oxide (MOX) fuels, which contain plutonium and uranium, will begin with a plutonium-dominated fission vector and softer spectrum. As the fission cross-section for plutonium isotopes is higher than for uranium isotopes, the MOX core will burn through the plutonium faster than the uranium resulting in a reverse transition to a more uranium-dominated fission vector and a harder spectrum as burnup increases.

Qualitatively, the shift in spectral shape during irradiation can be demonstrated by comparing the reactor spectrum at an irradiation time $t = \tau$ with the original spectrum at $t = 0$ across all energy bins. Figure 5.2 is a depiction of one such calculation for four different core compositions: low-enriched uranium (LEU), a mixture of 2/3 low-enriched uranium and 1/3 mixed-oxide (LEU+MOX), reactor grade mixed oxide (RGMOX), and weapons grade mixed-oxide (MOX). The grade of the mixed-oxide indicates the percentage of ^{239}Pu out of

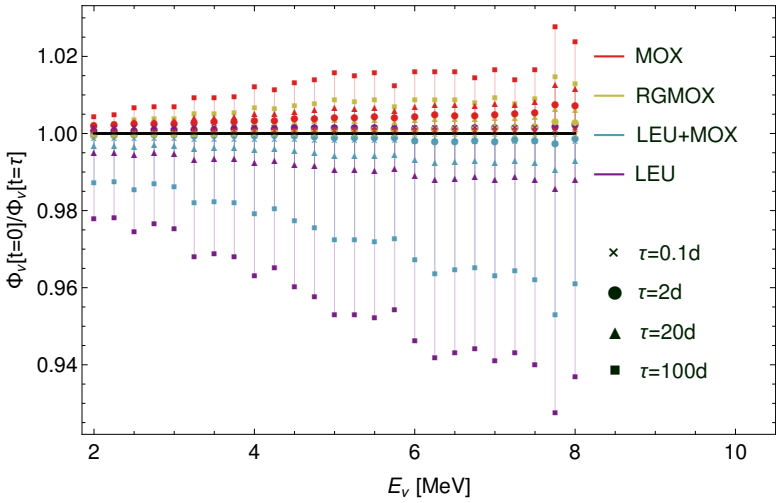

Figure 5.2: Ratio of the reactor antineutrino spectrum in 250 keV energy bins at an irradiation time $t = \tau$ with the initial spectrum at $t = 0$. The ratio illustrates a concept known as differential burnup analysis and shows that uranium-dominated cores transition to plutonium-dominated ones and vice-versa, resulting in a softening or hardening of the antineutrino spectrum. Figure by author.

the total plutonium. For example, weapons grade requires $\geq 93\%$ of ^{239}Pu, whereas reactor grade will contain a higher percentage of the plutonium isotopes ^{240,241,242}Pu. Note that the plutonium-dominated cores of RGMOX and MOX experience a 'hardening' of their respective antineutrino spectra for longer t and the uranium-dominated cores of LEU+MOX and LEU experience a 'softening.' Visually, this is demonstrated by the positive deviation from the initial antineutrino spectrum $\Phi_\nu(t = 0)$ for MOX and RGMOX cores and a negative de-

[2]It is unfortunate, but burnup refers to both this transmutation process and the physical unit $BU = \langle \mathcal{P} \rangle T$

viation for LEU and LEU+MOX. This observation, while qualitative right now, represents a new method of verifying the core content of a nuclear reactor. We dub this differential burnup analysis (DBA).

An antineutrino detector will see this differential burnup process, showing a qualitative change in core composition with irradiation time, but a precise spectral measurement can lead to a quantitative measurement of the fission vector and, as shown next, the plutonium content. This is done through a deconvolution of the total antineutrino spectrum into its fissile components, resulting in an estimate of the fission rates. Then, knowledge of the fission rates lead to a limit on the actual abundance of each fissile in the core. For a given choice of fissile antineutrino yield $N_\nu^f(E)$, say those determined by Huber [128], the total number of antineutrino events in an energy bin is given by

$$n_i = N \sum_f \mathcal{F}_f \int_{E_i-\Delta E/2}^{E_i+\Delta E/2} \sigma(E) P(L,E) N_\nu^f(E) \tag{5.3}$$

where the antineutrino yield is multiplied by the oscillation probability $P(L,E)$, which depends on the baseline L and antineutrino energy E, and the interaction cross-section $\sigma(E)$ [147], and is integrated over energy bins defined by a central energy E_i and bin width ΔE. These integrals are then weighted by the fission rates $\mathcal{F}^f$ and multiplied by some normalization constant N, where N can be thought of as a function of the detector mass.

Equation 5.3 shows that the number of events in the i^{th} bin is determined by four free parameters $\mathcal{F}^f$. If the baseline L and detector mass (or number of target protons in the case of IBD) are well-known then N will be known and the rate measurement from a reactor can be used to fix the power and reduce the number of degrees of freedom to three. This constraint is effectively given by Eq. 5.1, where it is assumed that the four main fissiles produce all of the reactor power. Whether the power is known or not, a χ^2 comparison can be computed between a true spectrum (denoted by a ^{0} superscript) and the fitted spectrum, given in Eq. 5.3. Thus, by minimizing Eq. 5.4, one can solve for the best fits to the fission vector $\vec{\mathcal{F}}$.

$$\chi^2(\vec{\mathcal{F}}) = \sum_i \frac{(n_i(\vec{\mathcal{F}}) - n_i^0)^2}{n_i^0} \tag{5.4}$$

If an overall plutonium measurement is desired, one can simplify the fission vector by writing $\vec{\mathcal{F}} = \{\mathcal{F}_{U235}, \mathcal{F}_{U238}, (1-\rho)\mathcal{F}_{Pu}, \rho\mathcal{F}_{Pu}\}$, where the combined fission rates of the plutonium isotopes have been simplified into $\mathcal{F}_{Pu} = \mathcal{F}_{Pu239} + \mathcal{F}_{Pu241}$ and ρ determines the 'dirtiness' of the plutonium, i.e. the grade. Now, the minimization of this adjusted χ^2, denoted as $\tilde{\chi}^2$ is only performed over the one parameter $\mathcal{F}_{Pu}$ and is given by

$$\tilde{\chi}^2(\vec{\mathcal{F}}) = \min_{\mathcal{F}_{U235}, \mathcal{F}_{U238}, \rho} [\chi^2(\vec{\mathcal{F}})] \tag{5.5}$$

where the minimum of the function $\chi^2(\vec{\mathcal{F}})$ is taken by setting $\mathcal{F}_{U235}$, $\mathcal{F}_{U238}$, and ρ to some constant set of values. A different grouping of variables can be used to isolate a single parameter in the minimization to determine the reactor thermal power.

Once a value of $\mathcal{F}_{Pu}$ is determined from the minimization scheme, it can be translated into an estimate of the abundance of plutonium through the relation $\mathcal{F}_{Pu} = \phi_t \Sigma_{Pu}$, which can be simply written as

$$\gamma = m_{Pu}/\mathcal{F}_{Pu} \tag{5.6}$$

so that $\mathcal{F}_{Pu}\gamma$ yields the plutonium mass and γ is some proportionality constant, relating the fission rate to the fissile abundance. From a quick dimensional analysis, it is obvious that $\gamma = 1/(\phi_t \sigma_{Pu})$ meaning γ has some dependence on the specific reactor in question. To determine the values of this ratio of plutonium mass to fission rate a detailed reactor simulation must be conducted.

As before, SCALE [145] is the simulation suite chosen as it has been developed by Oak Ridge National Laboratory and is considered a benchmark code for depletion analysis. A brief summary of the subroutines and functions of SCALE is given in App. B. For the non-proliferation focus, five different reactor designs are computed, each with a unique power history and fuel. The relation found in Eq. 5.6 is illustrated in Fig. 5.3, where the curves are based on full simulations of the reactor burnup with typical irradiation histories. The

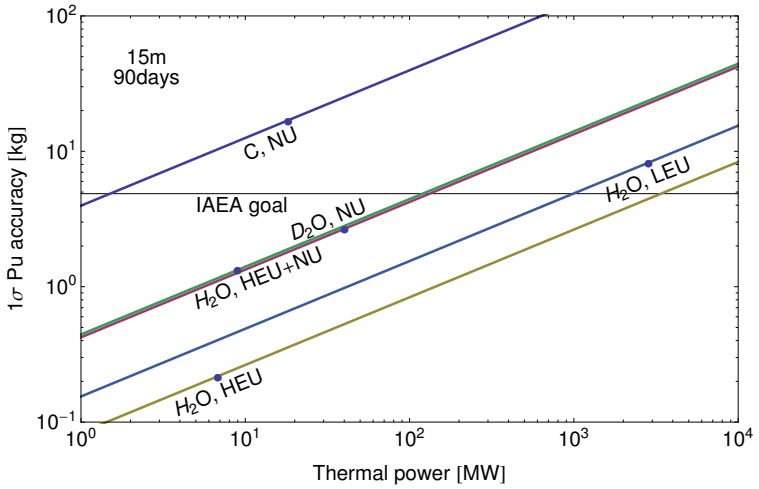

Figure 5.3: Absolute accuracy in the determination of the plutonium content as determined by a antineutrino measurement as a function of reactor thermal power. Each line represents a different type of reactor, where the labels indicate the moderator (C for graphite, D_2O for heavy water, and H_2O for water) and the fuel (NU for natural uranium, HEU for highly-enriched uranium, and LEU for low-enriched uranium). All plutonium accuracies assume a 15 m baseline, 90 d of data-taking, and a 5 t detector. The horizontal line represents the IAEA detection goal of 8 kg plutonium at 90% confidence level, corresponding to ~ 5 kg plutonium at the 1σ level. Figure courtesy of Ref. [4].

reactors present in these calculations are selected because they will appear in the non-proliferation study, with a reference commercial PWR supplied as well. For example, the

'C,NU' dot in Fig. 5.3 is the 5 MW_e reactor used by North Korea. Likewise, the 'H_2O,HEU' and 'H_2O,HEU+NU' dots are two configurations of the pool-style research reactor (the IRT) used by North Korea. Finally, the 'D_2O,NU' dot is a simplified version of the heavy water reactor used by Iran. An analog of the Daya Bay reactors, the 'H_2O,LEU' dot, is also computed for comparison. The details of the reactor simulations used in the non-proliferation cases will be described in Chp. 5.2 and Chp. 5.3. The PWR calculation can be found in Chp. 3.1.2.

Figure 5.3 indicates that for most of the considered reactor designs antineutrino monitoring can achieve the required sensitivity of the International Atomic Energy Agency, amounting to the detection of 8 kg of plutonium at the 90% confidence level in 90 d [175], which corresponds to ~ 5 kg plutonium at 1σ. This limit is defined by what the IAEA labels as a "significant quantity" and is the amount of plutonium required to construct a weapon, after fabrication and assumed material losses. The sensitivity curves have an increasing trend with reactor power, such that most reactors above 1 GW_t power, the majority of commercial reactors, will fail to meet the IAEA sensitivity limit. This is simply due to the incredibly large powers and corresponding fission rates, which translate into large plutonium production easily masked by the equally large uranium fissions. However, low-power research reactors, small modular reactors, and other plutonium producing reactors can be readily safeguarded by antineutrinos. This finding addresses the need for reliable safeguards for the research and plutonium-producing reactors, as these types of reactor have been the primary culprit of nuclear proliferation, not commercial reactors.

A rough estimate to the full reactor simulations can be found by writing the plutonium accuracy in terms of the proportionality constant, the average thermal power, and the baseline, mass, and data-taking time for the antineutrino detector. This expression is given as

$$\delta m_{Pu} = 1.942\,\text{kg}\left(\frac{\gamma}{10^{-16}\,\text{kg s}}\right)\left(\frac{L}{m}\right)\left(\frac{P_{th}}{MW}\right)^{1/2}\left(\frac{\text{tonnes}}{M}\right)^{1/2}\left(\frac{\text{days}}{t}\right)^{1/2} \tag{5.7}$$

where the detector mass assumes 8.65×10^{28} protons/tonne. Equation 5.7 reproduces the results of the full reactor simulation calculation within a few percent, with the following values of γ for the different reactor designs in Tab. 5.1.

Design	C,NU	H_2O,HEU	H_2O,HEU+NU	D_2O,NU	H_2O,LEU
γ [10^{16} kg s]	2.89	0.064	0.337	0.299	0.108

Table 5.1: Values of γ for the given reactor designs.

Now, a method of determining the core composition for a detected reactor antineutrino spectrum exists with the following steps. The detected antineutrino spectrum can be compared with a deconvolved one, as in Eq. 5.3, to generate a best fit for the total plutonium fission rate $\mathcal{F}_{Pu}$ with the adjusted χ^2 analysis of Eq. 5.5. Using the reactor simulations, one can determine a conversion from the plutonium fission rate to the plutonium mass. Therefore, a

successful link has been established between a signal seen at an antineutrino detector and a plutonium mass measurement m_{Pu} with some absolute accuracy δm_{Pu}, as given in Eq. 5.7.

This plutonium measurement can be done in a slightly different fashion by using the core burnup phenomenon. In this scenario, the reactor simulation can be used to determine the fission vector as a function of reactor burnup, where burnup is given by $BU = \langle \mathcal{P}_{th} \rangle T_{\text{irr}}$, or the average specific thermal power multiplied by the irradiation time. Recalling that the thermal power is related to the fission rate, results in the claim that BU is really a measure of the number of fissions that have occurred in the reactor. Burnup is typically measured in units of MWd/MTU, or MegaWatt days (MWd) per metric tonne of uranium (MTU)[3]. Thus, if a reliable reactor simulation with an initial fuel composition and a given power history is used, one can determine the progression of $\vec{\mathcal{F}}$ as a function of a single parameter, BU. This leads to the simplification of $\vec{\mathcal{F}}(BU)$, where, now, knowledge of the value for BU and an accurate reactor simulation, will result in a measurement of the fission vector and, thus, the plutonium content.

Essentially, this burnup analysis looks to draw upon the reactor physics to provide constraints to the progression of the fission rates. An example of this concept can be seen for the fission fractions of the C,NU core, where the fission fractions are defined as

$$F_f = \frac{\mathcal{F}_f}{\sum_{f=1}^{N_f} \mathcal{F}_f} \quad \text{where} \quad \sum_{f=1}^{N_f} F_f = 1 \tag{5.8}$$

and are subject to the constraint that all fissions in the core are from N_f fissiles, typically selected as $N_f = 4$. For example, in the case of the C,NU core, simulations show that the ^{235}U and ^{239}Pu fission fractions are highly anticorrelated, demonstrated in the right plot of Fig. 5.4. Thus, if one knows the original composition of the C,NU core and, thus, the original fission vector $\vec{\mathcal{F}}_0$ at the initial burnup $BU = 0$, the anticorrelation found by the reactor simulations can be used to infer $\vec{\mathcal{F}}$ at some later burnup BU.

This method of determining the fission vector from a single BU measurement requires a reasonably accurate reactor simulation. SCALE simulations require information about the core design, initial loading, and power history. If this information is not available, the reactor simulations cannot be performed without entering a bias into the problem. Using unfounded reactor information will produce inaccurate measurements of the plutonium content and erroneous reactor physics constraints. However, if the reactor information is readily available, this alternative burnup constraint method yields the core inventory within $5-10\%$, oftentimes a small contribution to the overall error budget. In addition, the burnup constraint method relies on the measurement of a single parameter, BU, which will reduce the overall plutonium mass uncertainty in most cases. For example, if we propagate the BU error through to a δm_{Pu}, an error reduction of roughly 50% for the C,NU core is obtained. This will be explicitly shown later in Chp. 5.2.4.

[3]In reality, this unit is often used synonymously with metric tonnes of heavy metal (HM), which includes all heavy actinides

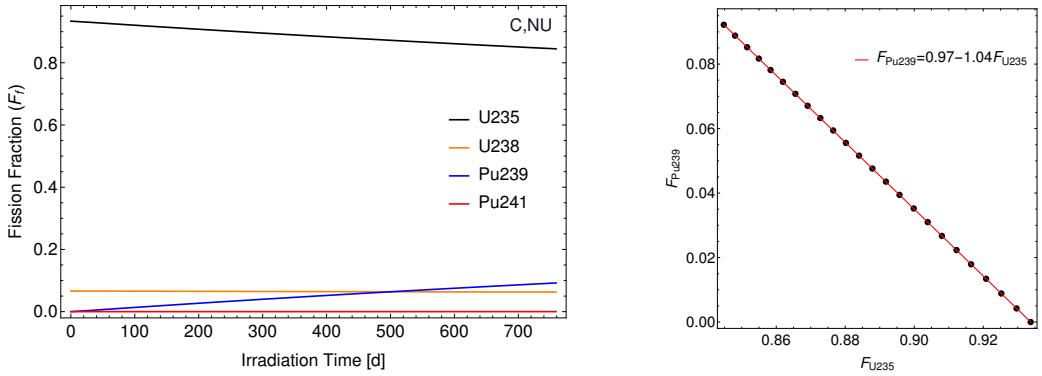

Figure 5.4: Progression of the four major fission fractions (left panel) in a graphite-moderated, natural uranium fueled reactor. The anticorrelation between ^{235}U and ^{239}Pu is identified in the right panel, where each BU step is plotted in f_{U235} and f_{Pu239} space. The best fit line is provided and shows almost perfect anticorrelation. Figure by author.

So far, two methods for determining the plutonium content in a nuclear reactor from an antineutrino measurement have been identified. If reliable and accurate knowledge of the reactor design and power history is available, the fission rates can be written as a function of burnup $\mathcal{F}_f(BU)$ and a value of BU that best matches the antineutrino spectrum can be acquired. This BU measurement and error can then be translated into a plutonium content measurement m_{Pu} and error δm_{Pu}. The alternative method, if reliable reactor data is unavailable, is to determine the best fit value of the combined plutonium fission rate $\mathcal{F}_{Pu}$ directly from the antineutrino spectrum. This is converted again to plutonium content and error. Using these two methods the impact of antineutrino safeguards in the special case of the North Korean nuclear crisis of 1994 and the Iranian heavy water reactor will be determined.

5.2 Antineutrinos and the DPRK Crisis

The impact of antineutrino safeguards is outlined for a real-world example of the North Korean nuclear crisis of 1994. A concrete example, such as the 1994 crisis, allows for a measure of the antineutrino safeguards' impact without introducing some bias against existing safeguards methods. No far-fetched scenario is invented to bolster the application of antineutrinos, but, rather, a historic event where existing safeguards did not produce the desired outcome is explored. Currently, the Democratic People's Republic of Korea (DPRK) is a nuclear power, defying the non-proliferation goals of the international community despite conventional safeguards. This acquisition of nuclear means first began with the 1994 crisis. First, a brief outline of the events leading up to the crisis is provided and a definition of the parameters for our sandbox example are given. Next, the application of

antineutrino safeguards is analyzed in several detector configurations to determine the best and most probable outcomes. Finally, a summary with some general statements concerning safeguards is provided.

5.2.1 DPRK Introduction

The DPRK, in our time of interest, operated two different reactors. The first is a $5\,\mathrm{MW_e}$ ($\sim 20\,\mathrm{MW_t}$) graphite-moderated and NU fueled reactor. This reactor is commonly labeled by its electrical power, so it is dubbed the $5\,\mathrm{MW_e}$ from now on. Design characteristics of the $5\,\mathrm{MW_e}$ closely follow those of the British Calder-Hall design and is a so-called Magnox-style reactor, named for the magnesium non-oxidizing fuel cladding used. The second reactor, the IRT, is a pool-style water-moderated research reactor. Little is known about the specific design characteristics of the IRT, but it operates using HEU fuel as the driving mechanism for fission, hence these fuel assemblies are named driver elements. The IRT also has the option of running with NU target elements, which absorb neutrons resulting in plutonium. Driver elements used in the IRT range from 10% to 80% enrichment of ^{235}U and the nominal power is $\sim 8\,\mathrm{MW_t}$ [195]. Both reactors will be described in detail after the history is unveiled next.

Major irradiation activity began in the DPRK in the mid 1980s. By this time the IRT research reactor was already running and under safeguards, using HEU supplied by the Soviet Union. As the IRT runs for 250 d out of the year [195] at only $8\,\mathrm{MW_t}$ the plutonium that can be generated, even with the use of NU targets, is small. In December of 1985, the DPRK signed the NPT [205], allowing the IAEA to placed its reactors under safeguards. A critical note, however, is that the safeguards agreement for the $5\,\mathrm{MW_e}$ did not enter into force until 1992, when the DPRK provided its initial plutonium declaration. The NPT allowed for the inspections of nuclear sites by the IAEA, which were conducted three times in 1992. Swipe samples were taken at various sites to investigate the ^{240}Pu content. Preliminary inspections found at least three different levels of ^{240}Pu content, indicating three separate reprocessing campaigns in 1989, 1990, and 1991 [207], compared with the DPRK declaration of a single campaign in 1990. Reprocessing is a method used to separate plutonium from spent nuclear fuel; plutonium potentially used for weaponization. The question of where the DPRK could acquire the spent nuclear fuel for three reprocessing campaigns quickly drew focus to the $5\,\mathrm{MW_e}$ reactor and a particularly suspicious shutdown.

Irradiation in the $5\,\mathrm{MW_e}$ reactor began in January of 1986. This reactor was run along the following burnup curve, adapted from Ref. [195], with one lone shutdown in 1989 before its eventual defueling in 1994. The shutdown in 1989 lasted for 70 d, enough time to remove $50 - 100\%$ of the core. Declarations by the DPRK indicated 90 g [208] of plutonium, but IAEA information allowed for as much as 14 kg [207]; the construction of a weapon typically requiring $\sim 8\,\mathrm{kg}$ plutonium. The primary method of safeguards at the time was a measurement of the burnup BU, a measure of the number of fissions that occurred in the

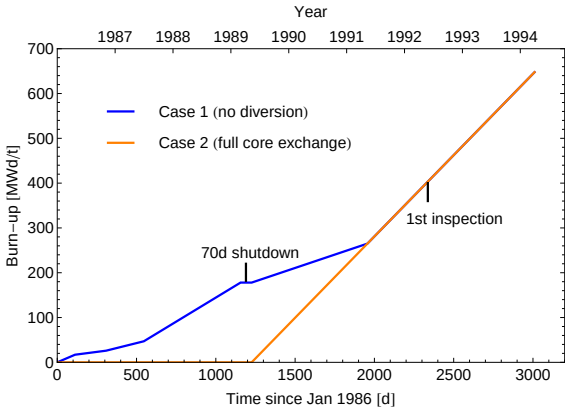

Figure 5.5: Burnup history of the 5 MW_e reactor at the Yongbyong site in North Korea. The core is suspected of having two different burnup options, labeled case I (blue) and case II (orange). Case I is based on the DPRK initial declaration that no core removal during the 70 d shutdown occurred and case II claims a fresh core was swapped in during the shutdown, which was then burned at higher power to reach equivalent burnups by the time of IAEA inspections. Figure courtesy of Ref. [4].

fuel. By the definition of $BU = \langle \mathcal{P}_t \rangle T$, one can see that the replacement of $\langle \mathcal{P}_t \rangle \to \alpha \langle \mathcal{P}_t \rangle$ and $T \to T/\alpha$ will leave the burnup invariant. Therefore, the DPRK could burn fuel along the blue burnup curve in Fig. 5.5, shut the reactor down for 70 d and restart with the same fuel, eventually measured by the 1992 IAEA inspection as having some burnup $BU = X$. However, the DPRK could have also burned the fuel along the blue burnup curve, shut the reactor down and **removed** the original fuel, replacing it with new fuel. This new fuel could then be burned at a higher power ($\sim 2\times$ higher) along the orange curve in Fig. 5.5 so that by the 1992 IAEA inspections the new fuel would be measured with the same burnup $BU = X$. The inability of the IAEA burnup measurement to differentiate between these two cases coupled with the evidence of multiple reprocessing campaigns lead to the suspicion that the DPRK had diverted an entire core, estimated to be as much as 14 kg of plutonium, from the 5 MW_e reactor. This is the central issue of the 1994 nuclear crisis.

The North Korean nuclear crisis of 1994 continued, ultimately resulting in three nuclear tests by the DPRK in 2006, 2009, and 2013. These nuclear tests have removed much ambiguity concerning the status and ultimate goal of the North Korean nuclear program, but at the time of the crisis there was a large degree of uncertainty over the amount of plutonium the DPRK could have and where it might be. For this antineutrino safeguards application, let us focus on the 5 MW_e reactor and test what information a dedicated antineutrino detector (AD) could have determined given the real historical boundaries. Our analysis is restricted to time periods when the DPRK was under some form of safeguards admitting that the installation of a hypothetical antineutrino detector would be naturally opposed by North Korea without a safeguards agreement. Next, the specific simulations conducted to model the 5 MW_e and IRT reactors are described in detail.

	SCALE	Ref. [209]	SCALE	Ref. [209]
Burn-up [MWd/t]	$\%^{240,241,242}$Pu	$\%^{240,241,242}$Pu	kg of Pu	kg of Pu
100	0.99	0.75	0.10	0.1
200	1.9	1.5	0.20	0.19
300	2.9	2.3	0.29	0.28
400	3.8	3.1	0.38	0.36
500	4.7	3.7	0.47	0.45
600	5.5	4.4	0.56	0.535
700	6.4	5.1	0.64	0.62
800	7.2	5.7	0.72	0.7
900	8.0	6.3	0.79	0.78
1000	8.8	6.9	0.87	0.86
1100	9.5	~ 7.5	0.94	~ 0.94
1200	10	~ 8.1	1.0	~ 1.02

Table 5.2: SCALE and Ref. [209] Magnox burn-up comparison of the isotopic percentages for plutonium.

5.2.2 Simulating the $5\,\mathrm{MW_e}$ Reactor

The simulation of the $5\,\mathrm{MW_e}$ reactor meets several benchmark estimates and can, thus, be considered an accurate model of the core used by the DPRK. The simulation is conducted in SCALE, specifically Origen-S, to compute the fission rates and abundances of various nuclides over the given irradiation history of Fig. 5.5. The core has a nominal power of $20\,\mathrm{MW_t}$ and runs with a full core size of 50 MTU and fuel in the form of a uranium-aluminum alloy. This core contains 812 vertical channels with 10 fuel elements per channel. The cladding used in the fuel elements is a magnesium-zirconium mixture called Magnox. Magnox cladding has the distinct characteristic of corrosion in contact with water. For this reason, the moderator of the $5\,\mathrm{MW_e}$ is CO_2 and the fuel elements that are removed from the core cannot be kept in some spent nuclear fuel pool, but instead must be immediately reprocessed. For this reason, the SNF correction of Chp. 3 is irrelevant here. The design specifications and the power history of Fig. 5.5 are taken from Ref. [195].

SCALE contains a pre-designed cross-section library corresponding to the Magnox-style reactors, so this is used for the calculation. The first benchmark comparison is of the plutonium isotopic content for a Magnox reactor. The simulated reactor is burned to various specific burnups, resulting in a measure of the isotopic percentages for plutonium. The results are computed by the Origen-Arp subroutine and are given by Tab. 5.2. Both the SCALE simu-

lation and Ref. [209] estimate very similar quantities of plutonium, but SCALE consistently determines a 'dirtier' plutonium content, that is more of the ^{240,241,242}Pu isotopes. The burnup values in Tab. 5.2 are simulated by running the core at a constant power P_{th} for 1000 d to reach the given burnup BU. The irradiation time of 1000 d is selected it is a typical cycle length for Magnox cores.

A second comparison was conducted between the fissile abundances and the values reported in Tab. VIII.5 of Ref. [195]. Here, the exact power history is simulated following Fig. 5.5 for a Magnox core of 50 MTU assuming a start date of January 1, 1986. Plotted on the right in Fig. 5.6 is the absolute abundance in kilograms of each of the four main fissiles. The two cases, diversion in orange and no diversion in blue, are again plotted with estimates of Ref. [195] as red dots. Again, the SCALE simulations are extremely accurate, with the exception of

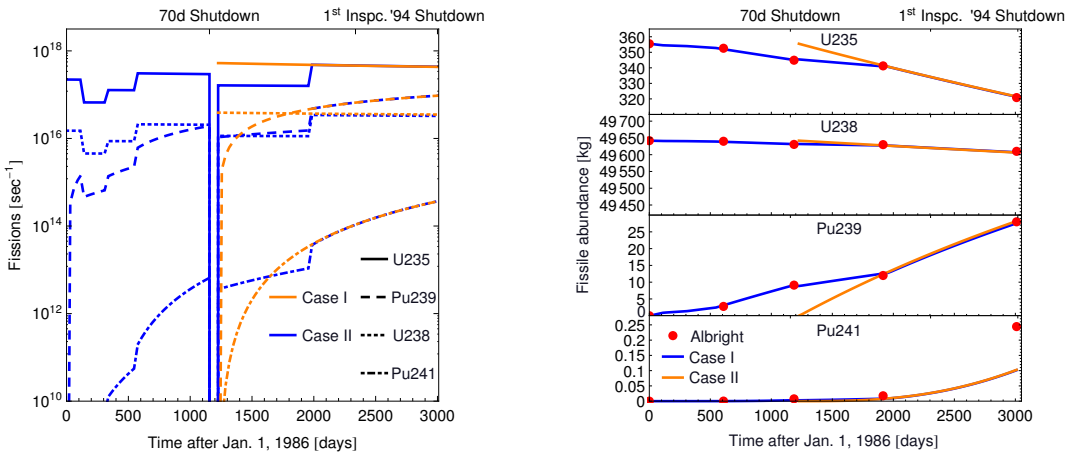

Figure 5.6: Fission rates (left) and fissile abundances (right) for the four main fissiles during the irradiation history of the 5 MW_e reactor. We provide the two cases of diversion (blue) and no diversion (orange) of plutonium. Estimates of the abundances from Ref. [195] are provided for reference. Figure courtesy of Ref. [3].

the ^{241}Pu production already addressed in Tab. 5.2. On a safeguards note, the differences between the two cases is clearly visible shortly after the 70 d shutdown, but rapidly vanishes by the time of the first IAEA inspection. Noting the value for the plutonium abundance just before the 1989 shutdown, provides an estimate of $\sim$ 8.8 kg of weapons-grade plutonium in the core that would have been removed. On the left side of Fig. 5.6 are the fission rates of the four main fissiles. Again, we note that there is a large discrepancy between the two cases immediately following the 1989 shutdown. This indicates that a spectral measurement, resulting in a measure of $\vec{\mathcal{F}}$, could identify the difference in core composition, but only in a specific window of time. We will show later that this disagreement can be used to accurately identify a core diversion after the shutdown.

5.2.3 Simulating the IRT Reactor

The IRT is a research reactor using a pool-style configuration with water as the moderator. This reactor contains 56 core grid compartments during the period of interest after 1986 [195]. Simulating the IRT is difficult as no pre-made cross-section library exists in SCALE and the exact configuration of driver and target elements is unknown. Thus, one must base possible configurations on similar IRT reactors, such as the IRT-Sofia [210] located in Bulgaria. The total number of driver elements available to the DPRK is restricted to about 92, each with 80% enrichment [195] and the IRT could operate at 8 MW_t for 250 d out of the year. In order to simulate the IRT reactor, a design must be constructed for the driver and target element, then these design accuracies and the overall effect of different fuel configurations on fission rates and abundances can be examined in the Origen-S calculations.

The data on the composition and dimensions of the driver and target elements can be found in Tab. VIII.6 of Ref. [195] and the IRT power history used is from Tab. VIII.7 of Ref. [195]. To summarize our model, the IRT used 80% enriched uranium-aluminum alloy drivers with an aluminum cladding in a light water moderator surrounded by a reflector. The target elements are quatrefoil natural uranium metal in an aluminum cladding. The initial core loading for the IRT is taken to be 6 kg for the drivers and 633 kg for the targets [195]. With this information, the maximum typical load is approximately 30 drivers with a remaining 26 element slots for target elements, but only 24 were used according to the mass estimates. The individual design characteristics of the driver and target elements are given as Fig. 5.7.

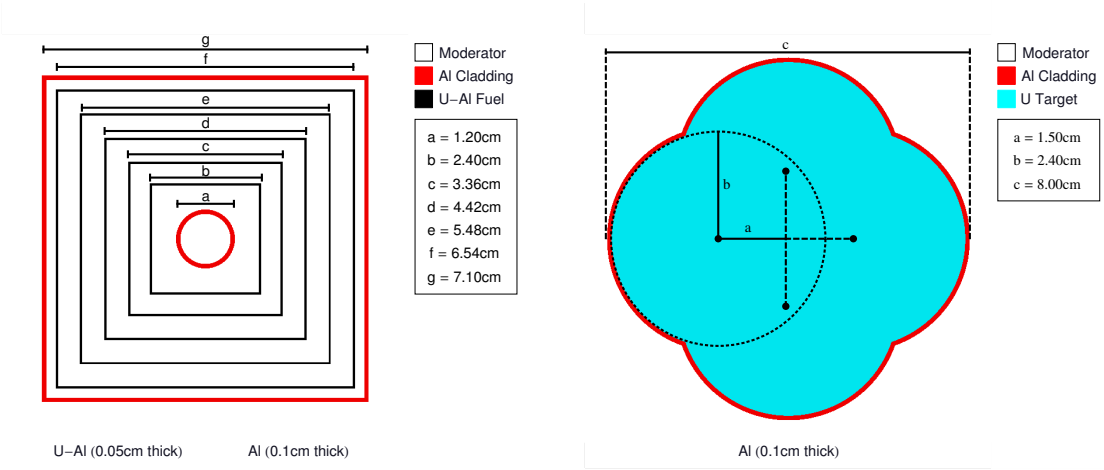

Figure 5.7: Design specifications for the IRT driver elements (left) of 80% enriched uranium, and the IRT target elements (right) of natural uranium. Dimensions and material listings are provided via the KENO-VI subroutine of SCALE [145] and are based on Tab. VIII.6 of Ref. [195]. Figure courtesy of Ref. [3].

Starting with the designs of the drivers and targets a simulation can be performed with the neutron-transport subroutine NEWT and the depletion coupling routine Triton to generate cross-section libraries for various configurations and the supplied burnup history of the IRT. The first test will determine the impact of choosing a specific core configuration, where two possible core configurations are considered. Both configurations are produced to maximize the proximity between a target element and any driver element. The core configurations and dimensions are provided as Fig. 5.8, where the left panel has been deemed version one and the right panel is version two. Each separate core configuration uses the different

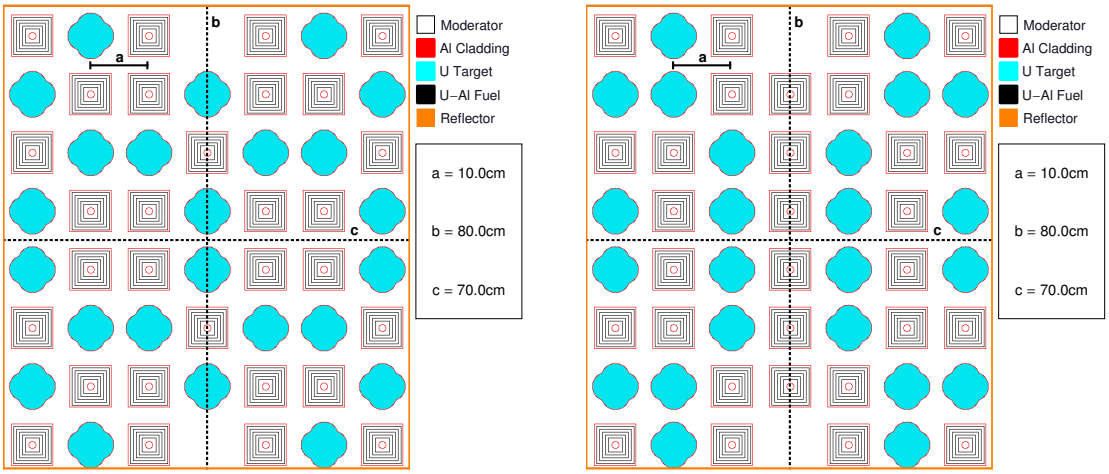

Figure 5.8: Two possible core configurations for the IRT research reactor in Yongbyong, North Korea. The dimensions and materials are based upon Ref. [195] and the layout resembles that of the IRT-Sofia [210] in Bulgaria. These material diagrams are the result of the Keno-VI subroutine. Figure courtesy of Ref. [3].

SCALE subroutines to generate the cross-section libraries for the two core versions and this is followed with an Origen-S depletion calculation to generate the fission rates and abundances. To simplify the simulation, the method of element summation was also considered. This consisted of simulating only the drivers or only the targets in these core configurations and summing the resulting fission rates and abundances. Finally, the most simplified method of simulating a lone driver and lone target element, weighting them by their core loads and summing was also tested. Interestingly, the fission rates and abundances were found to be nearly identical in all three simulation methods: the full core, the partial cores, and the lone sums. Full core simulations yielded slightly larger fission rates for ^{239}Pu and ^{238}U, but the total fission rates were dominated by ^{235}U. All abundance calculations yielded the same results within a few percent, leading to the conclusion that the core configuration is a very small effect. For this reason, the lone element simulations with a weighted sum is used as it introduces no configuration assumptions.

The fission rates calculated from the IRT via just drivers and just targets, as well as the sum of these for a driver+target run is given as the left plot of Fig. 5.9. The fission rates

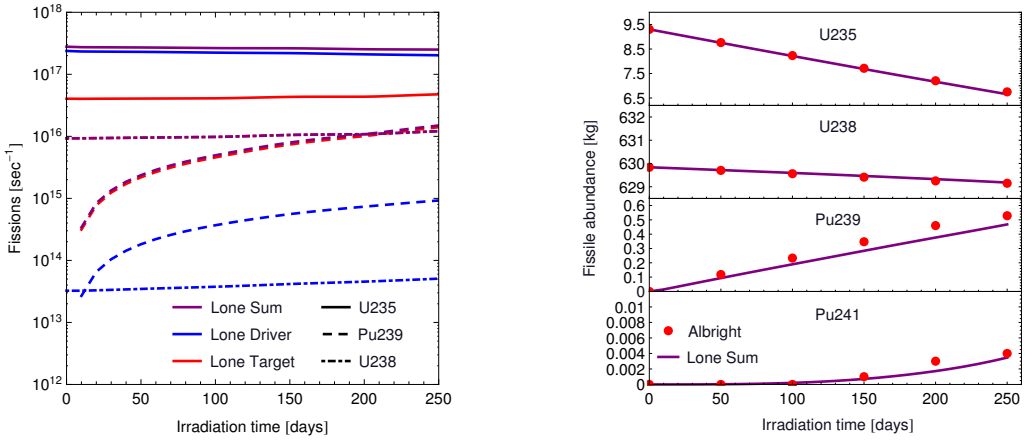

Figure 5.9: The fission rates (left) of the three main fissiles (^{241}Pu is negligible here) in the IRT reactor during the power history given in Ref. [195]. The fission rates are computed using the lone sum method (see text). The fissile abundances (right) for the four main fissiles are also included and compared with the estimates provided in Ref. [195]. Again, the fissile abundances are computed via the lone sum method. Figure courtesy of Ref. [3].

are clearly dominated by ^{235}U. In addition, as the majority of ^{235}U fissions are from the drivers, the drivers will dominate both the power and fission rate for the whole IRT, with or without targets. The targets only supply a small number of fissions, in agreement with the relative power contributions of the drivers and targets. The weighted sum of the fission rates assumes 6 kg for the drivers and 633 kg for the targets, in accordance with Ref. [195]. The fissile abundances of the four major fissiles show that the lone sum method is accurate in determining the plutonium content for the IRT as well. The results show that about 0.5 kg of plutonium could be extracted from each 250 d run of the IRT, but there would only be enough 80% enriched drivers for three such runs, limiting the IRT plutonium production in our time of interest to $\sim$ 1.5kg.

One final item of note is that the non-linear corrections estimated in Chp. 4 for the 5 MW$_e$ reactor and the IRT are 2.7×10^{-2} % and 0.11%, respectively. As these numbers were calculated with the irradiation histories supplied by Ref. [195] and the antineutrino monitoring is only being applied to the exact historical scenario of the North Korean nuclear crisis of 1994, there is no need to estimate non-linear corrections for any other power history. Thus, the non-linear correction is deemed negligible for this case.

5.2.4 Antineutrino Safeguards in the DPRK

In the previous two sections SCALE was determined to accurately reproduce the fission rates and fissile abundances in the 5 MW_e and IRT reactors when compared with reference estimates. In addition, the statistical methods of determining the plutonium content based on an antineutrino spectrum has been outlined in Chp. 5.1.1. With these two tools, one can reliably estimate the impact of antineutrino safeguards for the DPRK. A hypothetical antineutrino detector near the 5 MW_e reactor before and after its 1989 shutdown is considered first. This consideration uses the standard of a 5 t detector with 100% efficiency at 20 m baseline distance from the reactor. The detector mass is chosen to allow for a mobile AD, contained completely within a standard 20′ shipping container. In reality, a larger detector mass can fit in such a container, but after reasonable detector efficiencies are considered, the detector mass will be increased accordingly. Using these parameters, a detector of this size will observe around 95000 events for one year of data-taking.

First, consider a power sensitivity measurement, which uses the χ^2-function given by

$$\chi^2 = \sum_i \frac{1}{n_i^0}\left[\left(NP_{th}\sum_f F_f R_i^f\right) - n_i^0\right]^2 \tag{5.9}$$

where the n_i^0 are the measured number of antineutrino events, F_f are the fission fractions, and R_i^f are the fissile antineutrino yields in the i^{th} energy bin for a fissile f. Finally, P_{th} is the thermal reactor power and N is some normalization constant. In the context of the detection process, N is dependent on the baseline and detector efficiency. As N and P_{th} can be combined into some extra factor $\tilde{P}_{th}$, any uncertainty on the value of N will directly translate to an uncertainty in P_{th}. The antineutrino fluxes in each energy bin can be computed using the fission rates from Fig. 5.6 for each fissile combined with the fissile antineutrino yields of Fig. 5.1, which is then converted to an antineutrino event rate via Eq. 5.3. Allowing the fission fractions to float and assuming the baseline and detector properties are well-known, a solution for P_{th} can be acquired from minimizing Eq. 5.9, which results in the left plot of Fig. 5.10. The results of this power measurement show that any deviation from the declared power history is extremely apparent to a dedicated antineutrino detector. Power sensitivities as small as 2% are achieved assuming N is well-constrained, meaning that antineutrino safeguards for the 5 MW_e reactor before and after its 1989 shutdown would have provided clear evidence of a diversion.

As discussed in Chp. 5.1.1, the plutonium content of a reactor can be measured via Eq. 5.5. First, the combined plutonium fission rates are determined, allowing the power, uranium fission fractions, and plutonium grade ρ to float. A best-fit value for $\mathcal{F}_{Pu}$ is determined for the 5 MW_e reactor during each data-taking period and converted into a plutonium mass measurement via Eq. 5.6. The result is given by Fig. 5.10, where the dashed error bars indicate the errors from this plutonium fission variation fit. Recall that a plutonium mass measurement can be made using the burnup model derived from the SCALE simulations as

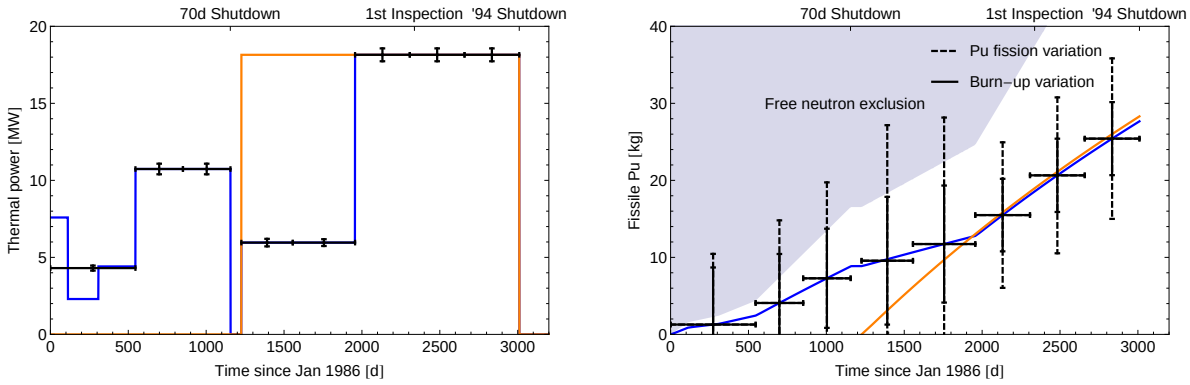

Figure 5.10: The power measurement (left) for the 5 MW_e reactor and the corresponding 1σ errors for the no diversion case (blue) reported by the DPRK. Also provided are the plutonium mass measurements (right) for the 5 MW_e reactor for several detection periods. Black dashed errors are the 1σ sensitivity using a plutonium fission rate variation. The solid black errors show the 1σ sensitivity when using a burnup model generated by simulation to constrain the fission vector. The diversion case (orange) assumes a complete core replacement in 1989. Both measurements use a 5 t detector at 20 m baseline from the 5 MW_e reactor. Figure courtesy of Ref. [3].

well. This method replaces the four independent fission rates with four functions of the single parameter BU, i.e. $\vec{\mathcal{F}} \mapsto \vec{\mathcal{F}}(BU)$. Then, the χ^2 is conducted by minimizing the value of BU. As claimed in Chp. 5.1.1, the incorporation of the burnup variation constraint reduces the overall plutonium error by about 50%. The blue exclusion region included in Fig. 5.10 results from assuming that all prompt neutrons created in fission that are not needed to maintain a $k_{eff} = 1$ are captured on ^{238}U to produce plutonium.

Next, safeguards mechanisms for the IRT reactor are briefly explored. Using the fission fractions of Fig. 5.9 and the antineutrino yields, the IRT antineutrino spectrum can be produced for all irradiation steps. Using the power measurement, for 50 d data-taking times each and a 5 t detector at 20 m baseline, the thermal power will be constrained to within 0.6 MW_t in each 50 d period. This uncertainty is below the additive power supplied when targets are introduced to the reactor ($\sim$ 2 MW_t), which indicates that the use of target elements could be seen by an antineutrino detector when compared to the IRT running on only driver elements. Unfortunately, it is trivial for the reactor operator to simply lower the IRT power to compensate for the targets, rendering this distinction inadequate. This power adjustment masks the addition of the targets simply because the entire core is dominated by ^{235}U fissions, see Fig. 5.9, making any spectral measurement of the plutonium content difficult. These same power manipulations are easily caught with antineutrino safeguards in cases like the 5 MW_e reactor because the burnup measurement will still show the plutonium composition in that a normalization factor (power change) in the ^{235}U fission yield can never precisely reproduce the 'softening' aspect of the ^{239}Pu fission yield, see Fig. 5.1. Therefore,

safeguards at the IRT are found to be difficult and will merely result in a plutonium estimate per 250 d cycle.

Next, an intriguing safeguards option is presented, the parasitic safeguards method. This method is the most probable, historically. As mentioned previously, the 5 MW_e had not entered into a safeguards agreement prior to 1992, which indicates that the prospect of an AD located adjacent to the reactor building of the 5 MW_e is, at best, implausible. However, the IRT reactor has been under safeguards since 1977. A method of measuring the 5 MW_e

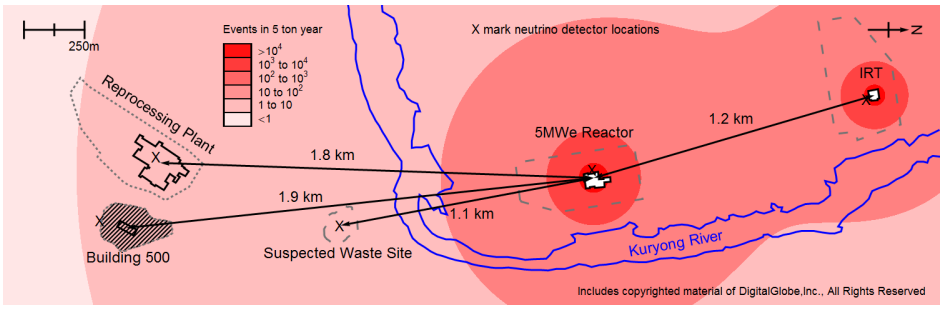

Figure 5.11: A map of the relevant facilities to the North Korean nuclear crisis of 1994. Possible antineutrino detector (5 t) locations are marked with an 'X'. The antineutrino event rates are given as the red contours. This detailed map is based on a satellie image taken on May 16, 2013 by GeoEye-1. Figure courtesy of Ref. [4].

reactor power from a deployment at the IRT reactor would, then, be historically possible; this is the parasitic measurement. A parasitic power measurement will rely on a good signal to noise ratio between the much farther 5 MW_e reactor, which is the source of interest, and the much closer IRT reactor, now serving as a background. To put the measurement in perspective, an antineutrino event rate map of the areas of interest is provided as Fig. 5.11.

For the parasitic measurement, the AD at the IRT would have a baseline of ~ 1.2 km from the true source, the 5 MW_e reactor. The routine shutdown periods of the IRT allow one to conduct safeguards for the IRT, while it is running, and safeguards for the 5 MW_e reactor, while the IRT is shut down. The period of the IRT reactor operations allows for two crucial measurements of the 5 MW_e reactor power, following the 1989 shutdown, but before IAEA inspections were conducted. This region is precisely where the largest difference in $\vec{\mathcal{F}}$ is observed in the simulations of the 5 MW_e reactor, see Fig. 5.6. To match the burnup value found in the 1992 inspection, the 5 MW_e reactor would have to operate at ~ 18 MW_t, instead of the declared 8 MWt immediately following the 70 d shutdown. When the IRT shuts down, data-taking can begin on the 5 MW_e reactor once all but the long-lived nuclides remain. Using the information from Fig. 3.3 in Chp. 3.1.2, the long-lived nuclide dominance occurs about $1-5$ d after shutdown, leaving only the SNF contribution of ^{90}Sr, ^{106}Ru, and ^{144}Ce. A spent nuclear fuel calculation was conducted for the IRT and an initial abundance of these long-lived nuclides was determined, represented by Tab. 5.3

The SNF calculation can be used to determine the contribution of the IRT during shutdown

Isotope	^{90}Sr	^{106}Ru	^{144}Ce
Abundance [atoms]	3.4×10^{23}	2.8×10^{22}	2.5×10^{23}

Table 5.3: SCALE-calculated spent nuclear fuel composition for the IRT reactor after a typical irradiation history with driver and target elements.

to the power measurement of 5 $\mathrm{MW_e}$. The data is collected over two separate 100 d periods, but the event rates from the 5 $\mathrm{MW_e}$ reactor are still small enough to warrant a Poisson log-likelihood definition for a χ^2-function given by

$$\chi^2 = 2\sum_i (n_i \log\left(\frac{n_i}{n_i^0}\right) - (n_i - n_i^0)) \quad \text{with} \quad n_i = NP_{th}\sum_f f_f R_{f,i} + SNF_i \tag{5.10}$$

where the SNF_i is the spent nuclear fuel contribution from the IRT shutdown for some energy bin i. The power measurement made in this scenario utilizes the finite endpoint of the SNF signal from the IRT. As discussed in Chp. 3, the endpoints of the long-lived nuclides fall in the range $E_0 \leq 3.55$ MeV. However, the spectrum from a nuclear reactor will extend far above this endpoint. Therefore, the large background of the SNF from the IRT can be completely removed with judicious energy cuts, leaving the pure[4] reactor spectrum from the 5 $\mathrm{MW_e}$ reactor. This is illustrated in Fig. 5.12. The 1σ sensitivities, $\sim 3.2\,\mathrm{MW_t}$,

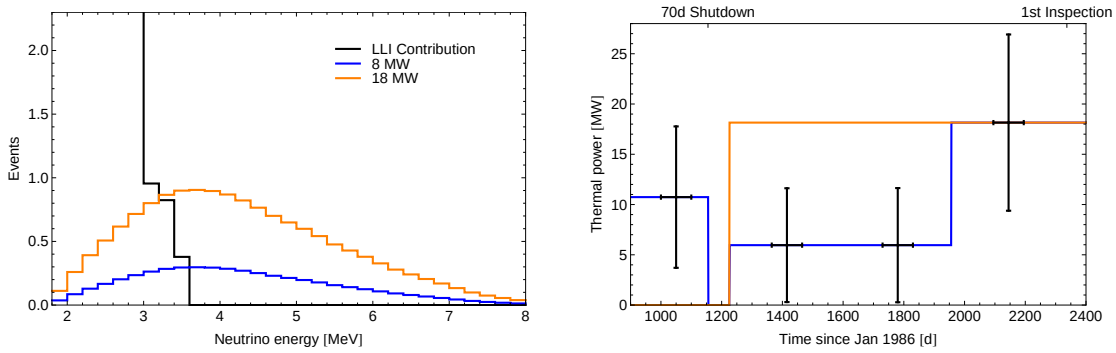

Figure 5.12: Event spectrum from the 5 $\mathrm{MW_e}$ (on) and IRT (off) reactors. Parasitic measurement of the 5 $\mathrm{MW_e}$ reactor power (right) with a 5 t detector located at the IRT (20 m baseline), but observing the 5 $\mathrm{MW_e}$ reactor (1.2 km). Both plots show the declared no removal case (blue) and the suspected removal case (orange). Figure courtesy of Ref. [3].

for the parasitic power measurement of the 5 $\mathrm{MW_e}$ reactor still show a discrepancy at the 3.2σ level between the two cases. This indicates that if the backgrounds can be shielded sufficiently with an overburden or pulse shape discrimination, a single AD could monitor multiple reactors. In addition, if the signal is detectable at a significant distance, the detector

[4]Background rates are discussed later

Location	Reactor Distance [m]	Waste Distance [m]	Reactor Events	Waste Events	χ^2	2σ Time [y]
Building 500	19080	80	10.1	0.9	0.34	≥ 10
"Suspected Waste Site"	1060	25	35.3	8.9	8.22	0.33
Reprocessing Plant	1830	25	11.8	8.9	16.95	0.15
Reprocessing Plant	1800	100	12.2	0.6	0.12	≥ 10

Table 5.4: Various waste detection via antineutrino detection scenarios. Listed are the location of the hidden waste, the baselines to the two major signals ($5\,\mathrm{MW_e}$ reactor and waste), events, χ^2, and 2σ significance detection time. All calculations assume a 5 t detector with 1 y of integrated data-taking. The waste source is the SNF from the $5\,\mathrm{MW_e}$ reactor decayed to 3 y before detection begins.

could be placed far enough underground to boost overburden [211]. Background suppression will be discussed later. The result of Fig. 5.12 is the most probable safeguards scenario for the DPRK during the time of interest. The parasitic antineutrino measurement of the $5\,\mathrm{MW_e}$ reactor, backgrounds pending, could distinguish between the diversion and no-diversion case at a high level of confidence, which would certainly prompt international action.

An alternative monitoring scenario is the detection of spent nuclear waste that is being reprocessed or otherwise hidden. If sufficiently accurate knowledge of the potential waste location is available, an AD can be specifically placed to measure it. In this case, the measurement is looking for an SNF-like signal with the running reactor as background. For example, the waste from the 70 d shutdown was suspected to be located at the reprocessing plant, "suspected waste site", or building 500 [195], the locations of these are given in Fig. 5.11. The radiochemical and "suspected waste site" can be safeguarded at relatively short baselines ($\sim 25\,\mathrm{m}$), but building 500 was declared to be a military site and, thus, is exempt from safeguards. The SNF atomic abundances are calculated for the $5\,\mathrm{MW_e}$ reactor, as we did in Tab. 5.3, and decayed to about 3 y, the elapsed time from removal in 1989 until the 1992 inspection. This allows us to determine the sensitivity of an AD to the long-lived nuclides still present in the nuclear waste.

The same Poisson log-likelihood χ^2-function of Eq. 5.10 is used in this analysis. The best possible baselines are assumed for the three different scenarios: the waste is located at building 500, the waste is located at the "suspected waste site", or the waste is in the reprocessing plant. In the case of the reprocessing plant, we also consider the case that the waste could be in several locations within the plant itself, so the worst-case scenario (i.e. longest baseline) is also provided here. Table 5.4 provides the details of these waste detection calculations. Table 5.4 indicates that a positive detection can be made for the existence of waste above the background reactor spectrum in ~ 120 or ~ 55 days from the start of IAEA inspections in 1992 at the 2σ confidence level if the waste is located at the "suspected waste site" or in the nearest wing of the reprocessing plant, respectively. The other two scenarios

Source	Fast neutron [S:N]	β-n [S:N]
$5\,\mathrm{MW_e}$	14.3	4.76
IRT	7.14	2.32
IRT parasitic	3.85×10^{-3}	9.52×10^{-4}
Waste	1.35×10^{-3}	3.25×10^{-4}

Table 5.5: Signal to noise ratios of the predicted backgrounds from fast neutrons and cosmogenically produced β-n radionuclides in the 5 t detector at the surface.

indicate that no significant measurement can be made in a reasonable time simply because the waste source is too far away.

Again, this analysis has been presented with no background estimate. This issue is remedied now, providing an estimated signal to noise ratio for the four different antineutrino safeguards options listed. As all of these safeguards options assume surface-deployment, the background rates will be equivalent between them. The primary backgrounds for IBD detectors are accidentals, where two single events accidentally satisfy the prompt-delayed signature, fast neutron induced backgrounds, where a neutron enters the target and scatters off of a proton (mistaken for the prompt signal) and finally thermalizes and captures (mistaken for a delayed signal), and cosmogenically produce radionuclides that beta-neutron decay, where a cosmic muon produces a short-lived radionuclide that decays with an electron (mistaken for the prompt signal) and a neutron (mistaken for the delayed signal). The largest contributors of the β-n background are ^{9}Li and ^{8}He.

Both fast neutrons and cosmogenically produced radionuclides are determined by the cosmic ray flux, which has typically been measured underground. One can scale the fluxes seen in underground experiments, but this scaling is non-trivial as it depends both on the raw flux and the particle energy. For example, the scaling can be expressed in terms of the flux and the average muon energy given by $R \propto \phi_\mu \langle E_\mu \rangle^\alpha$ [212], where ϕ_μ is the muon flux and $\langle E_\mu \rangle$ is the average muon energy. At the surface these values are $127\,\mathrm{m^{-2}s^{-1}}$ and 4 GeV, respectively using Ref. [213]. The value of α depends on the background type and can range between 0.7-0.9. Beginning with the measured values of ϕ_μ and $\langle E_\mu \rangle$ from 300 meters water equivalent (mwe) and the background rates given by Ref. [212], one can scale up to the surface deployment finding a rate of $1\mathrm{d^{-1}t^{-1}}$ fast neutron events and $43\,\mathrm{d^{-1}t^{-1}}$ β-n events in our detectors, which are assumed to have the composition of CH_2. Applying these background rates to our reported event rates for the different safeguards methods produces the corresponding signal to noise ratios (S:N) given in Tab. 5.5.

Clearly, some of the measurements that have been explored in this chapter will be currently impossible due to the large backgrounds, primarily the parasitic power measurement and the waste measurement. This finding definitely diminishes what would be the historically probable application of antineutrino safeguards at the DPRK. However, it should be noted

that our calculation assumed no overhead shielding and does not utilize background rejection methods. While perfect background rejection is unphysical, recent experimental efforts have aimed to reduce these backgrounds enough for surface-deployment [71,162,163]. In addition, pulse shape discrimination shows promise of separating different particle types based on their differential energy deposition, which could greatly reduce backgrounds. For example, this was first demonstrated to separate gammas and neutrons [164], but pulse shape discrimination has been applied to the solar antineutrino experiment Borexino [165] and has lowered the backgrounds of antineutrino experiments at the surface [166].

Both safeguards methods that are safe from extreme background noise are the reactor site measurements. In this case, a reactor adjacent to the containment building is utilized to measure the power, burnup, and, thus, the plutonium content. The highest level of constraint antineutrino reactor monitoring provides is the simultaneous measurement of a power and a burnup by an AD, both of which are possible for nearby reactors. Furthermore, if the AD was present at the start of an irradiation history, the initial burnup is known and a power measurement would alone constrain any deviation from the declared operation history. Coupling this online monitoring with a burnup measurement ensures that no core diversion is possible between shutdowns, either. In this fashion, **an antineutrino detector monitoring a reactor from startup removes nearly all possibilities of diversion without detection** with a simultaneous power and burnup measurement.

To summarize, the North Korean nuclear crisis of 1994 provides a real historical example of a non-proliferation attempt where the conventional safeguards methods failed to prevent a nation from acquiring nuclear weapons. The main issue centered around a degeneracy in fuel burnup and an overall uncertainty in the amount of plutonium that the DPRK may have. A hypothetical antineutrino detector for safeguards at each of the reactors in question would have thwarted any diversion attempt via a power measurement. In addition, the antineutrino safeguards is able to estimate the amount of plutonium that was available (8.8 kg), providing the international community with valuable knowledge. These measurements are aided by the use of detailed reactor simulations, which reduce the errors in the plutonium measurement significantly. For a reduced background rate, which many current experiments are currently pursuing [71, 73, 162, 214], a parasitic measurement may be possible allowing a single AD to monitor multiple reactors as well. A waste detection method would also be possible provided credible location tips are provided.

5.3 Antineutrinos for the Iranian D_2O Reactor

Next, the focus shifts to a current-events scenario that also provides an interesting application of antineutrino safeguards. The IR40 reactor located in Arak, Iran is a 40 MW_t natural uranium fueled and heavy water moderated reactor. Again, the use of natural uranium makes the IR40 highly capable of producing plutonium. It has been postulated that a

redesign of the IR40 into a reactor fueled by LEU might alleviate some of the non-proliferation concerns [215]. Indeed, the feasibility of this redesign has been studied by Willig *et al.* [216] and found to be physically possible with minor safety modifications to the reactor. As of the most recent version, the Joint Comprehensive Plan of Action (JCPOA), signed on July 14, 2015, has envisioned such a modification of the IR40. The JCPOA, an international agreement between the P5+1 (China, France, Russia, United Kingdom, United States + Germany) and Iran, calls for a redesign of the IR40 so that it will operate using uranium enrichments not to exceed 3.67% [217]. The benefits of a dedicated antineutrino detector for safeguards at the IR40 is offered next. This supplemental safeguards option was determined prior to the calls for a redesigned IR40, but a unique application of the differential burnup analysis is studied in light of the core redesign.

The scenario outlined here is hypothetical, but based on the prior non-proliferation failures in the North Korean nuclear crisis of 1994. Therefore, the events considered for the IR40 are meant to mimic the DPRK crisis and no suggestion that Iran will conduct operations in this way is intended. Say that the IR40 is under safeguards with a dedicated antineutrino detector near the reactor containment vessel. The reactor begins irradiating for $N-1$ months, but in the N^{th} month continuity of knowledge (CoK) is broken, where communication breaks down between Iran and the IAEA. Furthermore, let us assume that the reactor is shut down immediately following the loss of CoK. This scenario mirrors the actions of the DPRK in the 1994 nuclear crisis and so it becomes important to determine if antineutrino safeguards would apply in a modern case with this different reactor design. The same statistical analyses used in the DPRK case are used here, but first a simulation for the IR40 is needed.

5.3.1 Simulating the IR40

The IR40 operates at a nominal power of $40\,\mathrm{MW_t}$ using approximately $10\,\mathrm{t}$ of UO_2, fabricated with natural uranium. The IR40 contains approximately 150 fuel assemblies, each inside individual pressure tubes. The pressure tubes, composed of Zircalloy-2, contain a light water coolant and 18 fuel elements. The fuel is UO_2 with Zircalloy-2 cladding. A thin helium gap exists between the fuel and the cladding. The fuel assemblies are arranged in a triangular lattice pattern with one centralized open guide tube for neutron measurements. The containment unit itself is designed from stainless steel. A visual representation of a single fuel assembly is given as Fig. 5.13. These individual fuel assemblies can be arranged into a full core simulation, where the two dimensional model is derived from a full three dimensional analysis conducted by Willig *et al.* [216]. The subroutine Triton manages a NEWT neutron transport calculation and then couples this with a depletion calculation to generate cross-section libraries for the IR40 along its typical burnup history. These cross-section libraries are then used in an Origen-S depletion calculation to generate the fission rates and fissile abundances. The results obtained, in terms of isotopic composition for the major fissiles and the main plutonium isotopes, agree within $1-2\%$ of the 3d model.

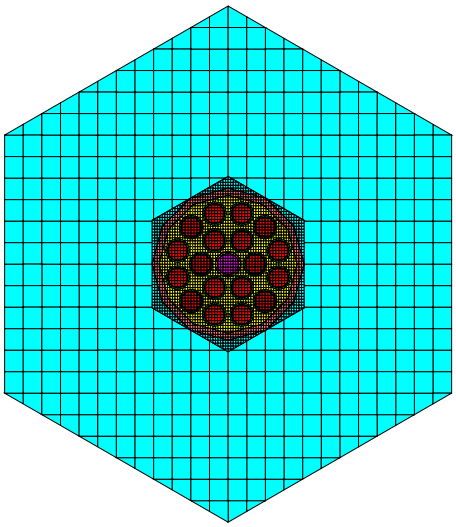

Figure 5.13: Material design specifications for the IR40 fuel assembly as calculated by the neutron transport code NEWT. The teal and yellow regions are the D_2O moderator, the red is the UO_2 fuel, green and pink are the cladding, the magenta is pressurized nitrogen gas and the blue (barely visible) is the helium gap. Figure by author.

Alternate designs were considered, where the LEU fuel would be doped with some amount of erbium to act as a burnable poison. This simulation is trivially determined from the original calculation by replacing the UO_2 fuel with natural enrichment in Fig. 5.13 with UO_2 fuel enriched to 2.8% with 1.5% erbium by volume. Using the reactor simulation, Willig *et al.* found that the addition of erbium would reduce the k_{eff} from ~ 1.5 to ~ 1.06 for higher uranium enrichment values, thus providing a safe alternative to NU fuel. These values were checked with our 2d simulations as well, verifying that the conversion of the IR40 from NU to LEU fuel is indeed possible by reactor standards.

Similar to the calculation of the IRT reactor in Chp. 5.2.3, it was found that simplifying the simulation by considering a lone fuel assembly, then weighting it with the corresponding core mass resulted in negligible differences compared with a full core simulation. Therefore, the lone fuel assembly seen in Fig. 5.13 can be used to calculate the safeguards limits and sensitivities for the IR40 to high accuracy. One last note is that the non-linear correction derived in Chp. 4 for the IR40, estimated at 0.15% per fuel cycle is negligible against the total reactor antineutrino spectrum.

5.3.2 Safeguards for the IR40

The hypothetical scenario for the IR40 operation involves irradiating the core at the reactor nominal power of 40 MW_t for 270 d. Here, 270 d represents the longest irradiation time possible without diminishing the ^{239}Pu content below 93% of the total plutonium amount [216]. This value is the limit of weapons-usability [175] and, in the case of a diversion attempt, considered to be the goal of a rogue nation. Next, suppose an unexpected shutdown occurs for 30 d. In this time, inspections are refused and diplomatic tensions rise limiting the ability of the IAEA to monitor the core through conventional means: cameras and seals. After the shutdown, the core is powered on again without any indication of a refueling process. Continuity of knowledge has been lost in this case and the analysis below illustrates that antineutrinos can restore it with high confidence.

Suppose the IR40 is under antineutrino safeguards and, as such, it has a dedicated 5 t AD located outside the reactor containment building, approximately 17.5 m from the core. The AD has an assumed efficiency of 100%, which can be scaled to reasonable levels with an appropriate increase in the detector volume. Using the statistical framework of Eq. 5.5 in the previous section, where the antineutrino events n_i^0 are derived from the fission rates as calculated by SCALE and the fissile antineutrino yields of Fig. 5.1. An adjusted χ^2 is formed by allowing the plutonium fissions to be combined and leaving the power, uranium fission fractions, and plutonium grade ρ as free parameters. Minimizing the $\tilde{\chi}^2$ and converting it via Eq. 5.6 yields our plutonium measurement over time as given by Fig. 5.14. The burnup

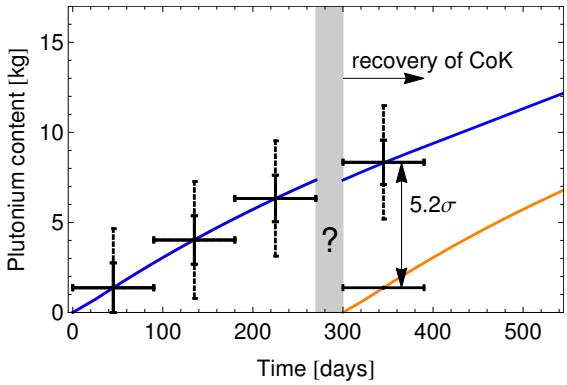

Figure 5.14: Measurement of the plutonium mass in the IR40 reactor for a case with no material diverted (blue) and all material diverted (orange) during a 30 d shutdown. The measurements are taken every 90 d. During the shutdown, continuity of knowledge is lost, but antineutrino safeguards demonstrate a clear ability to restore this knowledge. Figure courtesy of Ref. [5].

constraint can be applied to the IR40 case, as the reactor simulation model has shown that is it accurate. This burnup constraint lowers the errors in the plutonium measurement, which promotes the confidence of a full core swap to 5.6σ after the core has been restarted. In addition, if only a 90% confidence level is required, a detection of as little as 1.9 kg of removed

plutonium can be seen in 90 d after restart. Alternatively, the full-core swap is discernible only 7 d after the restart at the 90% confidence level.

This high level of sensitivity essentially arises due to the significant differences between a fresh and an old reactor core. The older cores will have much more plutonium, so their spectra will be much softer. Analyzing the χ^2 between two such reactor spectra results in Fig. 5.15, where the core of average age 45 d has a much harder spectrum than the core with an average age of 315 d. Note that the fit of Fig. 5.14 assumes a free power, so attempts to mask the spectral difference via a power shift are unable to fool the antineutrino detector. A key item to take away from Fig. 5.15 is that the change in spectral shape is completely

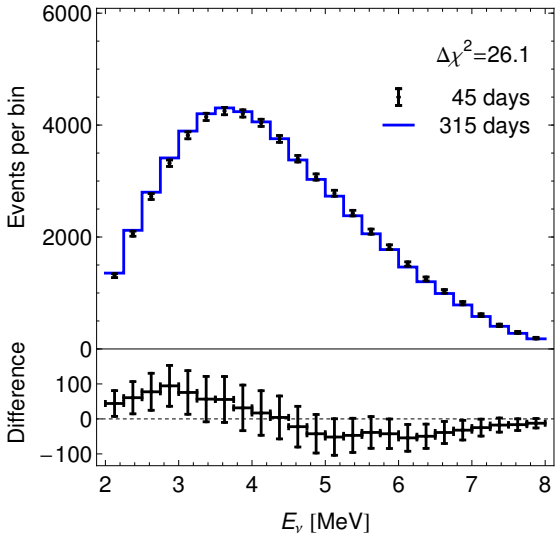

Figure 5.15: Comparison of the spectral shapes between a core with an average age of 45 d (black data points) and a core with an average age of 315 d (blue). The events are taken over 90 d and assume the same detection characteristics. The bottom panel illustrates the absolute difference between the two cores and the corresponding 1σ error bars. Figure courtesy of Ref. [5].

bimodal, meaning that above $\sim$ 4 MeV it decreases with core age and below $\sim$ 4 MeV it increases with core age. This indicates that the change in the measured age of a core is relatively insensitive to energy resolution effects. The above difference in χ^2 of $\sim$ 26.1 units indicates a plutonium difference of 7 kg.

A possible deterrent to antineutrino monitoring could be the permanent shutdown of the core. If the core is unloaded and the reactor is never turned back on, the determination of a core swap is made more difficult, even though this may increase international intrigue. Supposing the IR40 remains shut down, the antineutrino detector can still utilize the long-lived nuclides that remain in the shut down core. The same three long-lived nuclides, and their daughters, are used in this analysis. The SNF composition of the shut down IR40 is estimated and a search for these low-energy antineutrino events is conducted. Searching for

270 days reactor runtime							
BKG	TSS	90% CL			99% CL		
factor	[d]	Signal	BKG	TTD [d]	Signal	BKG	TTD [d]
2	30	81	3923	56	226	12471	178
1	0	37	806	23	93	2102	60
	30	39	911	26	101	2487	71
	90	46	1261	36	120	3503	100
0.5	30	20	228	13	49	578	33
180 days reactor runtime							
1	30	55	1857	53	152	5780	165

Table 5.6: Long-lived nuclide measurements, where the event rates are integrated over the energies between 1.8 and 3.6 MeV reconstructed antineutrino energy. The corresponding time to detection (TTD) is listed for the two confidence levels with the number of signal and background rates. The time since shutdown (TSS) is also varied, as well as the background scaling (BKG factor).

the long-lived nuclides has the advantage that the signal is constrained to energies below 3.6 MeV allowing for a fit to some backgrounds above this energy, which can constrain the background limits in the energy bins of interest. For example, if the shapes of the backgrounds are well known, see Chp. 3.2 for example, a measurement of the rate above 3.6 MeV will constrain the background rates in the energy region of the SNF. Using the same background estimates as in the DPRK case, which admittedly ignores the hadronic component of backgrounds, the conclusion is again made that a demonstration of sufficient background reduction will be needed for these types of in-core waste measurements.

With the appropriate background reduction, significant SNF measurements can be made at long times after shutdown. For example, in Tab. 5.6, one can see that even for double the background rates expected and a 30 d delay in data-taking, a 90% confidence determination of a missing core can be made within 56 d. Running the reactor to smaller burnups is more ideal for plutonium production, ensuring that the percentage of ^{239}Pu remains high. In these cases, with the estimated backgrounds, a 90% confidence determination of a missing core is still possible within 53 d at current background estimates. The measurements provided in Tab. 5.6 allow for a probe of the physical removal of the reactor core, eliminating the last possible avenue for diversion. Note that these limits still rely on untested background rejection abilities, but detector technology is expected to improve as more experiments head to surface-deployment.

It was mentioned earlier that the IR40 has been tested in different fuel configurations in Ref. [216] and that, indeed, has been the selection of the international community today [217].

A natural question that arises is the viability of antineutrino safeguards to verify the contents of the core. In this new scenario, the goal is to investigate whether antineutrinos can differentiate between a LEU and a NU core, in order to verify the core content at start-up. The technique used in this analysis is dubbed differential burnup analysis (DBA) and is visually given by Fig. 5.16. The primary observation of DBA is that the fission vectors of different fuel types progress at different rates in a reactor core. For example, the slope of the anti-correlation between ^{235}U and ^{239}Pu in the case of the natural uranium (NU) core, in green, is much steeper than that of the LEU core, in blue.

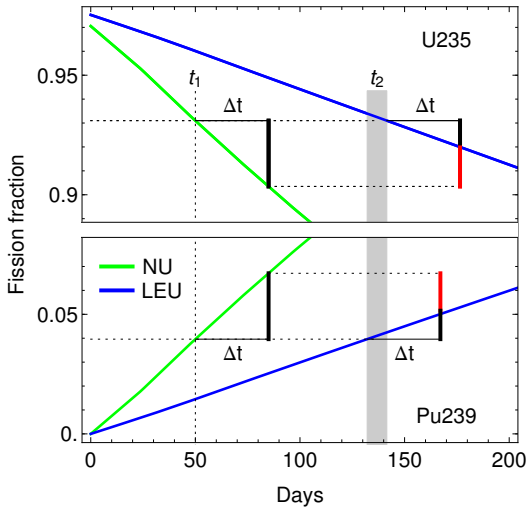

Figure 5.16: Differential burnup analysis (DBA) to distinguish between the burning of a natural uranium (green) and low-enriched uranium (blue) core. The top panel provides the fission fractions for ^{235}U and the bottom panel is for ^{239}Pu as a function of irradiation time. An analysis of the fission fractions at two different times, separated by Δt, shows that the rate of change of the fission fractions is significantly different for NU and LEU cores (i.e. the slopes of the green and blue curve are different). Figure courtesy of Ref. [5].

Different slopes mean that if two fission fraction measurements are taken separated by some time $\Delta t = t' - t$, with $\Delta F_{U235} = F'_{U235} - F_{U235}$ and $\Delta F_{Pu239} = F'_{Pu239} - F_{Pu239}$, then the difference between $\Delta F_{U235}/\Delta t$ and $\Delta F_{Pu239}/\Delta t$ will indicate the fuel type. In general, for $\Delta F_{U235} < 0$, cores with more plutonium will show smaller $|\Delta F_{U235}/\Delta t|$ and vice versa for $\Delta F_{U235} > 0$. This concept is echoed in Fig. 5.2, where the cores with more initial plutonium (RGMOX and MOX) will transition to more uranium-dominated cores for increases in irradiation time. Similarly, a core with more initial uranium (NU and LEU) will transition to more plutonium-dominated cores for increases in irradiation time. This analysis can be conducted for stable antineutrino detectors [158] to ensure no bias. Thus, two separate measurements of the fission fractions could yield an indicator of the fuel type. This analysis, applied to the IR40 in Fig. 5.16, shows that running the IR40 with the required fuel modifications (LEU) could be discernible from running the IR40 with NU fuel because NU fuel gains ^{239}Pu fissions

much more rapidly than LEU fuel.

With respect to the IR40 heavy water reactor in Iran, the center of a recent international diplomatic agreement, antineutrino safeguards applies very well for non-proliferation in many aspects. Using a constant, dedicated antineutrino detector, one can ensure that both the power and plutonium can be consistently measured, preventing any deviation from declared irradiation histories. In addition, antineutrino safeguards can recover from losses in continuity of knowledge if the IR40 were to shut down and restart. This recovery allows for a measurement of critical knowledge, such as the plutonium in the core before and after a shutdown. If the IR40 were to shut down and remain this way, measurements from long-lived nuclides could be used to determine if the core is being removed. This specific waste application requires more research and development in background suppression, but would be feasible with reductions by factors of $2-3$ from the first estimates made in Chp. 5.2.4. Finally, a new method named differential burnup analysis provides a unique method of determining the core content based on the fission vector progression, which could verify that the IR40 is running on LEU and not NU. The method of differential burnup analysis will be examined in future work to derive quantitative measurements.

5.4 Safeguards Conclusion

This chapter has focused on the application of reactor antineutrinos as a means of monitoring nuclear reactors for the purpose of non-proliferation of nuclear material. Using real historical scenarios, both past and present, the feasibility of antineutrinos has been demonstrated in these unbiased problems. Utilizing accurate reactor simulations, via the SCALE [145] simulation suite, antineutrinos have demonstrated the ability to determine an accurate power and plutonium mass measurement for a given reactor. The work has assumed cooperation between the reactor personnel and the scientists running the antineutrino detector, primarily through the close proximity $\sim 20\,\mathrm{m}$ of these detectors, but long-distance monitoring experiments have also been explored [72,218]. The findings presented here show that antineutrinos have an impactful application on the current status of international safeguards.

In the context of the North Korean nuclear crisis of 1994, it was determined that with all existing restrictions, the use of antineutrino safeguards could have supplied valuable information to the international community, consisting of accurate power measurements to determine deviations from declared histories and an estimate of the North Korean plutonium stockpile. The exact extent of the knowledge gained by antineutrino monitoring depends on the ability to reduce the estimated backgrounds for surface deployment, which are current avenues of research. However, it is not the goal of these results to rewrite history or claim what could have been; the goal is to present the abilities of antineutrino safeguards in light of any future nuclear disaster. Thus, a study was also conducted for a present-day case, where a diversion of plutonium is possible. This current case is the heavy water reactor,

the IR40, in Iran. Again, antineutrino safeguards perform extremely well. Simultaneous measurements of the power and burnup by a single antineutrino detector severely restricts the ability of a reactor operator to produce extra plutonium without detection. Lastly, for modest increases in background rejection techniques for surface-deployed antineutrino detectors, measurements of the physical presence of long-lived nuclides can indicate the proximity of a shut-down core. This last type of measurement would ensure that the removal of a core does not go unnoticed. Finally, a new examination, dubbed the differential burnup analysis, is qualitatively explored and results in a promising ability to discern fuel types used in a reactor.

For these reasons, antineutrinos can fulfill a very unique and substantial role in the field of reactor monitoring and safeguards. The results found in this work utilize a combination of the corrections found in Chp. 3 and Chp. 4 before applying antineutrinos to a practical use. Past theory derivations and experiments have paved the way for the future antineutrino monitoring tests, along with a increased effort of short-baseline neutrino detectors in the search of sterile neutrino oscillations. The marriage of these two experimental efforts seems appropriate as they both utilize the same source, at the same baselines, with the same background concerns. Therefore, it is the expectation that antineutrino monitoring will see tremendous progress with projects like Nucifer [162, 219], DANSS [214], Neutrino-4 [220], PROSPECT [71], NuLAT [73], and SOLID [221] all projected to start within the next few years.

Chapter 6

Conclusion and Outlook

Neutrino physics has progressed immensely in the nearly 90 years after its inception. Neutrino oscillation has been tested to high accuracy with a number of experiments, almost all finding excellent agreement with the 3ν oscillation framework. The three mixing angles and two independent mass splittings have been measured with good accuracy by accelerator, atmospheric, reactor, solar, and other experiments. Limits on the neutrino mass and preferences for nonzero CP-violating Dirac phase δ have also arisen. However, with the great success neutrino physics has witnessed, there are still many unanswered questions that require increased accuracy and new experiments. A measure of the value of δ, the mass hierarchy distinction, and any solution to the reactor, Gallium, and LSND anomalies will require well-constrained errors, excellent knowledge of the source and detection, and exceptional detectors. Therefore, for neutrino physics to become the more precision-based field it must, higher order corrections can no longer be ignored.

A critical source of neutrino information are the experiments conducted at nuclear reactors. Nuclear reactors represent both an immense and pure source of electron antineutrinos $\bar{\nu}_e$, as well as an incredibly complicated source. Corrections to the source are of paramount interest as they will affect all reactor neutrino experiments. One correction this work has studied in detail is produced by spent nuclear fuel (SNF). The SNF source is similar in structure to the non-equilibrium correction, as they both are derived from long-lived nuclides. It is well-known, and reinforced here, that these long-lived nuclides can contribute to the events seen in inverse beta-decay (IBD) detectors due to their rapidly beta-decaying daughters. As all commercial reactors, and most research reactors, store some amount of SNF onsite for several years, the contribution of this pure antineutrino source will affect the total reactor measurements made by oscillation studies. Essentially, all reactor neutrino experiments will measure both the antineutrinos from the reactor core itself (accounted for in the experimental analysis) and the spent nuclear fuel antineutrinos from the SNF pools (not typically accounted for in the analysis).

Our results, which use detailed reactor simulations, have shown that the SNF signal can be

as large as $1-3\%$ of the pure reactor spectrum in the low-energy bins just above IBD and below $\sim 3.6\,\mathrm{MeV}$. Over a significantly large data-taking period this low-energy excess in the observed antineutrino spectrum could be identified in current reactor experiments, e.g. Daya Bay. The signal itself is restricted to a few low-energy bins and can be seen easier for reactor-off data, but is still estimated to manifest itself as a 2.5σ excess in the Daya Bay near halls. An attempt to measure this excess would most likely be complicated with other higher-order corrections as well, such as the non-equilibrium and non-linear correction making a precise quantification difficult. However, if this complication can be overcome, an identification of the SNF signal, with its distinct shape and endpoint, will function as a benchmark for future reactor neutrino experiments. This measurement by Daya Bay would mark the first in a series of incredibly beneficial measurements to form a database of SNF signals for the different reactor experiments, similar to muon-based background measurements at various overburdens. This SNF database, dependent on the baselines and discharge burnup, would provide valuable background corrections for future reactor experiments, especially short baseline-single reactor layouts, many of which have been proposed as the next-generation of experiments.

A second correction was identified in this work from neutron-capture effects in a nuclear reactor. Original measurements of the beta-spectra from the fissions of ^{235}U, ^{238}U, ^{239}Pu, and ^{241}Pu have very little contribution from the neutron-capture component as proven in our research. Thus, the results here have identified another unaccounted-for antineutrino correction to the total reactor spectrum. Again, this contribution can be present in all reactor neutrino experiments, so it must be quantified. Detailed reactor simulations were used to emulate true reactor operations and derive the non-linear component across a wide expanse of reactor irradiation times and thermal neutron fluxes. This analysis of the neutron-capture impact on the antineutrino spectrum will need to be applied to all reactors used in oscillation studies, but will require dedicated reactor simulations to do so.

The non-linear results are found to have a dependence on the product of $\phi_t^2 T_{\mathrm{irr}}$. We have used reactor simulations with publicly accessible power histories to span 3 orders of magnitude in ϕ and nearly 4 orders of magnitude in T_{irr}. These simulations have matched with the analytical estimates of the non-linear component, providing confidence that the physics is well-understood. After analyzing the various reactors, a resulting $\sim 1\%$ correction in the low-energy bins was revealed for typical PWRs irradiated in a 3-batch system. The 3-batch system provides larger burnup for the core, effectively increasing the value of T_{irr} and the non-linear component. These types of reactors have been used in the major θ_{13} searches and some long-baseline and will be used in new hierarchy searches. To accurately model the low-energy component of the reactor antineutrino spectrum, a non-linear correction must be employed. Individualized simulations are, therefore, of paramount importance in order to ensure that the corrections from non-linear nuclides, spent nuclear fuel, and the non-equilibrium accumulation are handled in the appropriate manner for each antineutrino experiment.

Second order corrections, like the spent nuclear fuel and non-linear, have direct impacts in oscillation studies and other areas of neutrino research. Measurements of the mixing

parameter θ_{13} require a well-understood low-energy component to the total observed reactor antineutrino spectrum. The corrections of spent nuclear fuel, the non-equilibrium effect, and the non-linear effect, in total comprise a correction of $\sim 8\%$ in these low-energy bins. Thus, an accurate accounting of them is necessary for precise θ_{13} measurements at single baselines. These corrections could also cloud a measurement of short-baseline sterile oscillations in the low-energy bins if not accounted for, but the sterile oscillations would be observed across all energy bins. In addition, searches for geoneutrinos via reactor subtraction is highly dependent on an accurate parameterization of the reactor signal, most critically in the low-energy region. Furthermore, the spent nuclear fuel and non-linear nuclides could represent only a small number of the true reactor corrections. Additional consideration is needed to fully understand the reactor antineutrino source.

Neutrinos have not only provided immense knowledge and intriguing anomalies to the scientific community, but it is shown in this work that antineutrinos can also serve as a practical solution to the issue of reactor safeguards. Antineutrinos are uncommonly difficult to shield or manipulate meaning that true information of the reactor source can be inferred from their detection. The extent of antineutrino safeguards has been shown in the context of past circumstances, as in the North Korean nuclear crisis of 1994, and in recent events, as with the IR40 heavy water reactor in Iran. Coupling current International Atomic Energy Agency safeguards methods with a dedicated antineutrino detector would result in more robust monitoring. Antineutrinos can determine the reactor power with a rate measurement and the plutonium content with a spectral measurement. This information is critical for guaranteeing that a reactor is operated with power-generation in mind and not for the purposes of plutonium production and diversion. The benefit of antineutrino detectors is that real-time data is available and recovery of knowledge is possible, which are both assets that are missing from traditional IAEA safeguards.

Our analyses has shown that antineutrino monitoring can be an experimental possibility with moderate advancements in background suppression. These types of improvements are currently being pursued by surface-deployed antineutrino detectors and short-baseline searches. With these improvements, reactor antineutrino safeguards have the capability of determining the reactor power, the plutonium in a core, the fuel content via differential burnup analysis, and the existence of a shutdown core through the measurement of long-lived nuclides. These properties have been demonstrated in this research with a variety of nuclear reactors.

Some of the uses of antineutrino safeguards have been derived with the aid of these corrections, specifically the spent nuclear fuel. The non-linear corrections are seen to be a negligible effect in the cases of the DPRK reactors and the IR40, which ensures safeguards can be appropriately modeled, but individualized simulations are needed for any given reactor. The calculation of the spent nuclear fuel allows for a measurement of the existence of a shutdown core from the long-lived nuclides. This same union of applications and corrections research will be required for the future commercialization of reactor antineutrino safeguards, as well as standard physics searches. Therefore, the identification and quantification of higher order corrections serve both a scientific use, in the clarification of the source used to solve many

neutrino anomalies and unknowns, and as a practical use, in the online monitoring of nuclear reactors via dedicated antineutrino detectors.

Appendices

Appendix A

Fissile neutrino spectra

This section of the appendix provides the converted neutrino spectra for ^{235}U, ^{239}Pu, and ^{241}Pu as computed by Huber [128]. The tables of Tab. A.1 - A.3 below represent the antineutrino spectrum as well as a comprehensive summary of the errors and bias from the regularization technique used. The values in Tab. A.4 correspond to the ^{238}U *ab initio* calculation performed by Mueller [83]. Also listed with the Mueller data for ^{238}U is the recent measurement conducted at Garching [135]. This measurement was not conducted over the full Mueller energy range, so data is listed when it is available.

value		1σ errors
E_ν MeV	$N_{\bar{\nu}}$ fission^{-1}MeV^{-1}	total %
2.	1.32	1.8
2.25	1.12	1.8
2.5	9.15×10^{-1}	1.9
2.75	7.7×10^{-1}	1.9
3.	6.51×10^{-1}	1.9
3.25	5.53×10^{-1}	2.
3.5	4.54×10^{-1}	2.
3.75	3.64×10^{-1}	2.1
4.	2.94×10^{-1}	2.1
4.25	2.3×10^{-1}	2.3
4.5	1.79×10^{-1}	2.5
4.75	1.38×10^{-1}	2.5
5.	1.1×10^{-1}	2.6
5.25	8.64×10^{-2}	2.6
5.5	6.46×10^{-2}	$^{+2.7}_{-2.8}$
5.75	5.1×10^{-2}	$^{+2.9}_{-3.}$
6.	3.89×10^{-2}	$^{+3.1}_{-3.2}$
6.25	2.87×10^{-2}	$^{+3.3}_{-3.4}$
6.5	2.17×10^{-2}	$^{+3.3}_{-3.5}$
6.75	1.61×10^{-2}	$^{+3.4}_{-3.7}$
7.	1.14×10^{-2}	$^{+3.6}_{-3.9}$
7.25	7.17×10^{-3}	$^{+4.1}_{-4.5}$
7.5	4.64×10^{-3}	$^{+4.3}_{-4.8}$
7.75	2.97×10^{-3}	$^{+4.7}_{-5.2}$
8.	1.62×10^{-3}	$^{+6.8}_{-7.2}$

Table A.1: Antineutrino spectrum for ^{235}U. A beta spectrum is determined by Ref. [133] from 12 hr irradiation time, and converted by Huber [128]. Included are the energy bins, the $\bar{\nu}$ per fission and MeV, and the 1σ total errors in each of these bins.

value		1σ errors
E_ν MeV	$N_{\bar{\nu}}$ fission^{-1}MeV^{-1}	total %
2.	1.08	2.6
2.25	9.2×10^{-1}	2.6
2.5	7.19×10^{-1}	2.5
2.75	6.2×10^{-1}	2.6
3.	5.15×10^{-1}	2.9
3.25	3.98×10^{-1}	3.1
3.5	3.29×10^{-1}	3.3
3.75	2.61×10^{-1}	3.3
4.	1.95×10^{-1}	3.4
4.25	1.57×10^{-1}	4.
4.5	1.13×10^{-1}	4.9
4.75	8.33×10^{-2}	5.
5.	6.13×10^{-2}	4.7
5.25	4.83×10^{-2}	5.1
5.5	3.54×10^{-2}	5.7
5.75	2.92×10^{-2}	6.4
6.	1.92×10^{-2}	8.5
6.25	1.28×10^{-2}	9.4
6.5	9.98×10^{-3}	$^{+9.7}_{-9.8}$
6.75	7.54×10^{-3}	11.
7.	4.98×10^{-3}	13.
7.25	3.26×10^{-3}	18.
7.5	1.95×10^{-3}	23.
7.75	8.47×10^{-4}	27.
8.	5.87×10^{-4}	29.

Table A.2: Antineutrino spectrum for ^{239}Pu. A beta spectrum is determined by Ref. [134] from 36 hr irradiation time, and converted by Huber [128]. Included are the energy bins, the $\bar{\nu}$ per fission and MeV, and the 1σ total errors in each of these bins.

value		1σ errors
E_ν MeV	$N_{\bar{\nu}}$ fission^{-1}MeV^{-1}	total %
2.	1.26	2.5
2.25	1.08	2.4
2.5	8.94×10^{-1}	2.3
2.75	7.77×10^{-1}	2.3
3.	6.41×10^{-1}	2.4
3.25	5.36×10^{-1}	2.5
3.5	4.39×10^{-1}	2.5
3.75	3.46×10^{-1}	$^{+2.4}_{-2.5}$
4.	2.82×10^{-1}	2.6
4.25	2.2×10^{-1}	2.9
4.5	1.66×10^{-1}	$^{+3.3}_{-3.4}$
4.75	1.25×10^{-2}	3.5
5.	9.74×10^{-2}	$^{+3.3}_{-3.4}$
5.25	7.47×10^{-2}	$^{+3.4}_{-3.5}$
5.5	5.58×10^{-2}	$^{+3.6}_{-3.8}$
5.75	4.11×10^{-2}	$^{+4.2}_{-4.3}$
6.	3.05×10^{-2}	$^{+4.9}_{-5.}$
6.25	1.98×10^{-2}	$^{+5.3}_{-5.5}$
6.5	1.54×10^{-2}	$^{+5.4}_{-5.7}$
6.75	1.09×10^{-2}	$^{+5.6}_{-5.9}$
7.	7.75×10^{-3}	$^{+5.8}_{-6.1}$
7.25	4.47×10^{-3}	$^{+7.2}_{-7.5}$
7.5	2.9×10^{-3}	$^{+8.4}_{-8.8}$
7.75	1.78×10^{-3}	$^{+9.1}_{-9.4}$
8.	1.06×10^{-3}	$^{+12.}_{-13.}$

Table A.3: Antineutrino spectrum for ^{241}Pu. A beta spectrum is determined by Ref. [134] from 43 hr irradiation time, and converted by Huber [128]. Included are the energy bins, the $\bar{\nu}$ per fission and MeV, and the 1σ total errors in each of these bins.

value		
	ab initio [83]	Measurement [135]
E_ν MeV	$N_{\bar{\nu}}$ fission^{-1}MeV^{-1}	$N_{\bar{\nu}}$ fission^{-1}MeV^{-1}
2.	1.43	
2.25	1.26	
2.5	1.12	
2.75	9.80×10^{-1}	
3.	8.70×10^{-1}	9.586×10^{-1}
3.25	7.57×10^{-1}	7.952×10^{-1}
3.5	6.50×10^{-1}	6.603×10^{-1}
3.75	5.49×10^{-1}	5.406×10^{-1}
4.	4.50×10^{-1}	4.433×10^{-1}
4.25	3.67×10^{-1}	3.498×10^{-1}
4.5	2.94×10^{-1}	2.787×10^{-1}
4.75	2.32×10^{-1}	2.171×10^{-1}
5.	1.83×10^{-1}	1.700×10^{-1}
5.25	1.43×10^{-1}	1.341×10^{-1}
5.5	1.10×10^{-1}	1.032×10^{-1}
5.75	8.35×10^{-2}	7.737×10^{-2}
6.	6.21×10^{-2}	5.618×10^{-2}
6.25	4.70×10^{-2}	3.973×10^{-2}
6.5	3.58×10^{-2}	3.048×10^{-2}
6.75	2.71×10^{-2}	2.085×10^{-2}
7.	1.95×10^{-2}	2.093×10^{-2}
7.25	1.32×10^{-2}	1.139×10^{-2}
7.5	8.65×10^{-3}	7.132×10^{-3}
7.75	6.01×10^{-3}	
8.	3.84×10^{-3}	

Table A.4: Antineutrino spectrum for ^{238}U. A beta spectrum is determined by the so-called *ab initio* approach for an irradiation time of 12 hr and converted by Mueller [83]. Included are the energy bins and the $\bar{\nu}$ per fission and MeV. Also included are the values obtained by Ref. [135] in the energy bins where data was available.

Appendix B

Description of SCALE

This section is meant to introduce the mechanisms of the SCALE calculations utilized in much of the work. Specifically, the simulation used is SCALE 6.1.1 [145]. This simulation suite was designed by Oak Ridge National Laboratory (ORNL) and has been verified and maintained by a specific group at ORNL. SCALE is commonly used by the Nuclear Regulatory Commission (NRC) to test new reactor designs for criticality and safety. It has been designed with modularity in mind. Thus, many of the subroutines can be used in stand-alone calculations, but the true power of the simulation suite lies in its ability to couple subroutines together. The main workhorse used in this research has been the Origen-S depletion calculation, but the research presented in this work is the result of several subroutines: Origen-Arp, Origen-S, NEWT, Triton, and Keno-VI. All of these are briefly explained next.

Origen[1] is designed to solve depletion problems for nuclear reactor designs. The depletion calculation is performed by solving the so-called Bateman equations, a set of differential equations governing the destruction and production of nuclides. The equations used by Origen are similar to the original Bateman equations [142], but with additional production and destruction modes to account for the full reactor environment.

$$\frac{dN_i}{dt} = \sum_{j=1}^{m} l_{ij}\lambda_j N_j + \bar{\Phi}\sum_{k=1}^{m} f_{ik}\sigma_k N_k + F_i - (\lambda_i + \bar{\Phi}\sigma_i)N_i \qquad (i = 1, ..., m) \qquad \text{(B.1)}$$

Equation B.1, which closely resembles the one used in the non-linear calculation, Eq. 4.2, accounts for processes that produce nuclide N_i in the first three terms and for processes that destroy nuclide N_i in the last, negative term. The first term represents the decays of nuclide j to i given by the decay constant, λ_j, the atom density of nuclide j, N_j and the branching fraction, l_{ij}, for decays from nuclide j to i. The second term indicates neutron captures and fission production into nuclide i given by the space and energy-averaged neutron flux, $\bar{\Phi}$, the fraction of absorption on nuclide k that produce nuclide i, f_{ik}, and the spectrum-averaged

[1]The label 'Origen' will refer to common practices in both Origen-Arp and Origen-S. The exact difference between the subroutines will be described.

neutron absorption cross section of nuclide k, σ_k. The third term is a simple user-defined feeding rate F_i. The last term is the collection of depletion modes consisting of the decay of nuclide i via decay constant, λ_i, and neutron absorption with a spectrum-averaged neutron absorption cross section of nuclide i, σ_i. The indices are summed over all branches including nuclide i.

The nuclide decay data used in Origen, and SCALE in general, is taken from from ENDF/B-VII [222] ($\sim$ 2600 decay transitions) and the neutron data is pulled from JEFF/A-3.0 [125] ($\sim$ 12000 neutron-induced reactions). The energy group structure is up to the user, but for the majority of the research work conducted a 238 group structure for the neutron energies was used. A 44 group structure was used for the simulation of the HFIR [1]. The values for the fluxes are derived in Origen and are a function of the moderator, moderator density, and supplied power. Note that the flux is spatially averaged, in addition to the energy averaging. This spatial average requires knowledge of the core configuration, meaning that the proper fluxes and cross-sections are only derived after a neutron transport. This results in what is known as the cross-section libraries, a set of cross-section data for a given reactor design at various burnup values, which account for the core evolution. Additionally, an option is available for calculations that wish to irradiate with a given neutron flux instead of a given power. This input flexibility was especially useful in calculating the non-linear component for the Institut Laue-Langevin (ILL) and Garching measurements in Chp 4.

Origen solves the set of depletion equations, given by Eq B.1, generally numbering around $200 - 300$ unique nuclides via a matrix exponential solution. The transmutation equations are given by $\dot{\mathbf{N}}(t) = \mathbf{A}\mathbf{N}(t)$ of which the solution is

$$\mathbf{N}(t) = \exp[\mathbf{A}t]\mathbf{N}_0 \tag{B.2}$$

where the solution to Eq. B.2 uses $\mathbf{N}_0$, which are the provided initial conditions to Origen. The matrix $\mathbf{A}$ is an $N \times N$ transition matrix containing rate coefficients for radioactive decay, neutron capture, fission, and more. It is explicitly given by $\mathbf{A} = -\boldsymbol{\lambda} - \bar{\Phi}\boldsymbol{\sigma}$ where the set of decay constants is given by the matrix $\boldsymbol{\lambda}$ and the neutron induced transitions, which include neutron capture and fission, are summarized in $\boldsymbol{\sigma}$. The exponential in Eq. B.2 is expanded in a series representation and solved. Short lived nuclides can produce unfortunate round-off errors, so they are removed and calculated separately. The resulting matrix is computed as an eigenvalue problem.

Origen can construct a full irradiation history, given by both reactor-on and reactor-off time by stitching these two cases together. For example, when two irradiation periods are separated by a shutdown, Origen will solve the first irradiation period with the supplied powers (related to $\bar{\Phi}$) and time steps to the final irradiation time, say t_1. Next, Origen will use the values of $\mathbf{N}(t = t_1)$ as the initial conditions for the next decay period, where $\bar{\Phi} = 0$ now for no power, and solve for the nuclide abundances at each time step of the shutdown. Finally, the abundances at the end of the shutdown, $\mathbf{N}(t = t_2)$, can be used as the initial conditions for the next irradiation period. This process is repeated for all irradiation and decay periods listed. The output of Origen is user-defined. For the calculations in this

research, Origen produces a list of nuclides and their corresponding abundance (in g or Cu) and fission rates for every time step supplied. These abundances are parsed through a personally-designed parsing code to produce the input for the various analyses conducted in Chp. 3 - 5.

The primary difference between Origen-S and Origen-Arp is the graphical user interface. Origen-S allows for a much wider expanse of flexibility, so it is the primary depletion mechanism used. Origen-Arp is only used for very simple depletion calculations, such as the plutonium content for various burnups of a Magnox reactor, see Tab. 5.2.

The full neutron transport calculations are handled in the SCALE subroutine of NEWT, the New ESC-based Weighting Transport code. NEWT is a multi-group discrete-ordinates radiation 2-dimensional transport code. The benefits of NEWT are its flexible mesh definitions, which allow for complex geometries to be simulated accurately and rapidly. The Extended Step Characteristic approach is the defining characteristic that allows for this type of geometry simulation to exist. The Boltzmann transport equation is used with discrete steps defined by the mesh and characteristic times. NEWT is used in this research when a cross-section library is unavailable. For example, SCALE contains libraries on Westinghouse, GE, Magnox, CANDU, and Russian VVER cores, to name a few. However, if a unique reactor design is used, then NEWT can be implemented to determine the cross-section libraries needed for the Origen depletion calculation.

The material and dimensional specifications must be supplied to NEWT, where various shapes and polygons can be combined to generate the desired reactor design. NEWT contains a helpful array structure as well, which allows for individual reactor parts to be modeled and placed within larger structures or in a defined array structure. As most nuclear reactors use some type of array for the configuration of fuel assemblies, this simulation option greatly reduces the time required to construct such a reactor design. Boundary solutions must also be incorporated to the different meshes; most often a reflective boundary condition is used. In addition, the convergence criteria must be specified as well as any acceleration techniques. Finally, the media in each shape is defined to generate the global neutron transport calculation. The specific calculation methods used by NEWT to solve the Boltzmann equation is quite complicated and, as the work conducted in Chp. 3 - 5 only utilizes the simplest functions in NEWT, only this brief summary is provided.

The primary output generated by NEWT that is of concern is the individual cross-section library that is generated as a result of the transport calculation. This library provides the spatial and energy averaged cross-sections and flux used in Eq. B.1 for each reactor material. It should be noted that the transport code will rely on the specific fuel composition and power (i.e. the flux), so NEWT calculations are typically performed with a depletion code.

Triton is the SCALE control module that is used to call the neutron transport calculations. Triton is used to couple the cross-section determination in NEWT with a given fuel burnup and depletion calculation done in Origen. Triton is responsible for connecting these two calculations, which will result in the desired cross-section library for a variety of burnup

values. In this way Triton acts to call a cross-section processing program, BONAMI, which feeds a list of energy-dependent cross-sections for the given nuclides and reactions to NEWT. Then, a full 2-d neutron transport is conducted with the provided geometry via the discrete ordinates method. NEWT sends its library to COUPLE, which manages the cross-sections for the next step, an Origen-S depletion calculation. Once all of the material mixtures in the reactor design have a corresponding depletion and cross-section value, the process is restarted with BONAMI and the next burnup value. After all burnup values have been solved, the result is a cross-section library for a unique reactor design over a range of burnups. This library is then used by Origen-S in place of the standard supplied Westinghouse, etc. libraries, to conduct a final depletion calculation and generate the fission rates and nuclide abundances.

Triton also has the option of coupling with a 3-dimensional neutron transport code Keno-VI. Keno-VI is an extension of the KENO Monte Carlo criticality program developed for its use in SCALE. Keno-VI has the added benefit of a specialized geometry package, which can model an extensive variety of shapes. Keno-VI runs a full Monte Carlo particle transport with the provided reactor design and material listing. The primary purpose of Keno-VI is to determine the criticality, k_{eff}, for a given reactor design. This was the primary use of Keno-VI in this research as well, but the subroutine can, in principle, be used to calculate the fissions, fission densities, and flux densities as well. For example, Keno-VI was used to determine the value for k_{eff} in the redesigned IR40 reactor as well as estimate the criticalities of the IRT simulations used, ensuring that our design did not produce a non-functioning ($k_{eff} \ll 1$) or dangerous ($k_{eff} \gg 1$) reactor.

All of this information can be readily found in the SCALE 6.1.1 user manual, so any further inquiries are referred to Ref. [223].

Appendix C

Non-linear Derivation

This portion of the appendix provides the explicit derivations used in the non-linear correction analytical solution of Chp. 4. Three primary solutions are required for the calculation of the non-linear correction, these are the solution for the nuclide abundance of some stable linear nuclide, the solution to the unstable daughters in the linear parent beta-decay chain, and the solution for a stable daughter in the beta-decay chain. First, the generalized Bateman equation is provided again, which includes neutron capture, decay, and fission components.

$$\frac{dN_{\alpha,i}}{dt} = \vec{Y}_{\alpha,i} \cdot \vec{\mathcal{F}} - (\lambda_{\alpha,i} + \phi_t \sigma_{\alpha,i}) N_{\alpha,i} + \lambda_{\alpha,i-1} N_{\alpha,i-1} + \phi_t \sigma_{\alpha-1,j} N_{\alpha-1,j} \tag{C.1}$$

This differential equation shows that a nuclide $N_{\alpha,i}$ is produced via fission (the first term), the decays from a parent (the third term), and neutron captures (the fourth term). Then, $N_{\alpha,i}$ is also destroyed by the combined 'effective' decay constant $\tilde{\lambda}_{\alpha,i} = \lambda_{\alpha,i} + \phi_t \sigma_{\alpha,i}$, comprised of both $N_{\alpha,i}$ decays and neutron captures on itself.

The goal will be to solve Eq. C.1 with the given forms of the beta-parent $N_{\alpha,i-1}$ and neutron capture parent $N_{\alpha-1,j}$. In the case of the linear parent of a nuclide chain $i = 1$, the term $\lambda_{\alpha,i-1} N_{\alpha,i-1}$ is ignored as $N_{\alpha,i=1}$ has already been labeled as the chain parent and so no other nuclides will beta-decay to it. Therefore, taking the form of Eq. C.2

$$N_{\alpha,j} = \sum_{n=1}^{j} A_{\alpha,n} e^{-\tilde{\lambda}_{\alpha,n} t} + B_{\alpha,j} \tag{C.2}$$

for $N_{\alpha-1,j}$ one can solve Eq. C.1 as such.

$$\frac{dN_{\alpha,1}}{dt} = \vec{Z}_{\alpha,1} \cdot \vec{\mathcal{F}} - \tilde{\lambda}_{\alpha,1} N_{\alpha,1} + \phi_t \sigma_{\alpha-1,j} \left[\sum_{n=1}^{j} A_{\alpha-1,n} e^{-\tilde{\lambda}_{\alpha-1,n} t} + B_{\alpha-1,j} \right] \tag{C.3}$$

One can use the method of undetermined coefficients to solve for two separate solutions denoted as $\tilde{N}_{\alpha,1}$ for the homogeneous solution to Eq. C.8 and $N'_{\alpha,1}$ for the particular solution.

The homogeneous solution is trivially found to be an exponential solution in $\tilde{\lambda}_{\alpha,1}$ given by $\tilde{N}_{\alpha,1}(t) = \tilde{C}\exp[-\tilde{\lambda}_{\alpha,1}t]$, so what remains is a form and derivation for the particular solution. From inspecting Eq. C.8 it becomes apparent that $N'_{\alpha,1}(t)$ must have a form similar to the neutron capture parent $N_{\alpha-1,j}$. Thus, $N'_{\alpha,1}$ is given by:

$$N'_{\alpha,1}(t) = \sum_{n=1}^{j} A'_{\alpha,n} e^{-\tilde{\lambda}_{\alpha,n}t} + B'_{\alpha,1} \tag{C.4}$$

which results in the following solution for the undetermined coefficients $A'_{\alpha,n}$ and $B'_{\alpha,1}$ below

$$\begin{aligned}\frac{d}{dt}\left(\sum_{n=1}^{j} A'_{\alpha,n} e^{-\tilde{\lambda}_{\alpha-1,n}t} + B'_{\alpha,1}\right) = &-\tilde{\lambda}_{\alpha,1}\sum_{n=1}^{j} A'_{\alpha,n} e^{-\tilde{\lambda}_{\alpha-1,n}t} - \tilde{\lambda}_{\alpha,1}B'_{\alpha,1} + \vec{Z}_{\alpha,1}\cdot\vec{\mathcal{F}} \\ &+ \phi_t\sigma_{\alpha-1,j}\sum_{n=1}^{j} A_{\alpha-1,n}e^{-\tilde{\lambda}_{\alpha-1,n}t} + \phi_t\sigma_{\alpha-1,j}B_{\alpha-1,j}\end{aligned} \tag{C.5}$$

Carrying out the time-derivative, where $B'_{\alpha,1}$ is simply a constant and grouping common terms of $A'_{\alpha,n}$ and $B'_{\alpha,1}$ yields the following:

$$\sum_{n=1}^{j} A'_{\alpha,n} e^{-\tilde{\lambda}_{\alpha-1,n}t} + B'_{\alpha,1} = \sum_{n=1}^{j}\left(\frac{\phi_t\sigma_{\alpha-1,j}}{\tilde{\lambda}_{\alpha,1}-\tilde{\lambda}_{\alpha-1,n}}\right)A_{\alpha-1,n}e^{-\tilde{\lambda}_{\alpha-1,n}t} + \left(\frac{\phi_t\sigma_{\alpha-1,j}B_{\alpha-1,j} + \vec{Z}_{\alpha,1}\cdot\vec{\mathcal{F}}}{\tilde{\lambda}_{\alpha,1}}\right) \tag{C.6}$$

Reading off exponentials in $(\tilde{\lambda}_{\alpha-1,n}t)$ yields the assignments for the individual $A'_{\alpha,n}$. Essentially, for each value of n, the first term on the left-hand side will equal the first term on the right-hand side, yielding an expression for $A'_{\alpha,n}$ in terms of $A_{\alpha,n}$. In addition, the $B'_{\alpha,1}$ will be given by the only constant term available. Thus, Eq. C.6 results in the assignments:

$$A'_{\alpha,n} = \left(\frac{\phi_t\sigma_{\alpha-1,j}}{\tilde{\lambda}_{\alpha,1}-\tilde{\lambda}_{\alpha-1,n}}\right)A_{\alpha-1,n} \qquad B'_{\alpha,1} = \left(\frac{\phi_t\sigma_{\alpha-1,j}B_{\alpha-1,j} + \vec{Z}_{\alpha,1}\cdot\vec{\mathcal{F}}}{\tilde{\lambda}_{\alpha,1}}\right) \tag{C.7}$$

which can then be plugged back into Eq. C.4 and summed with the homogeneous equation to arrive at the total solution to the parent differential equation.

$$N_{\alpha,1}(t) = \tilde{C}e^{-\tilde{\lambda}_{\alpha,1}t} + \sum_{n=1}^{j}\left(\frac{\phi_t\sigma_{\alpha-1,j}}{\tilde{\lambda}_{\alpha,1}-\tilde{\lambda}_{\alpha-1,n}}\right)A_{\alpha-1,n}e^{-\tilde{\lambda}_{\alpha,n}t} + \left(\frac{\phi_t\sigma_{\alpha-1,j}B_{\alpha-1,j} + \vec{Z}_{\alpha,1}\cdot\vec{\mathcal{F}}}{\tilde{\lambda}_{\alpha,1}}\right) \tag{C.8}$$

All that remains is to select a value for the initial abundance of $N_{\alpha,1}(t=0) = N_{\alpha,1_0}$, which results in the parent form originally provided as Eq. 4.4 here:

$$\begin{aligned}N_{\alpha,1}(t) = &\left[N_{\alpha,1_0}\right]e^{-\tilde{\lambda}_{\alpha,1}t} + \left[\frac{\phi_t\sigma_{\alpha-1,j}B_{\alpha-1,j} + \vec{Z}_{\alpha,1}\cdot\vec{\mathcal{F}}}{\tilde{\lambda}_{\alpha,1}}\right]\left(1 - e^{-\tilde{\lambda}_{\alpha,1}t}\right) \\ &+ \left[\sum_{n=1}^{j}\frac{\phi_t\sigma_{\alpha-1,j}A_{\alpha-1,n}}{\tilde{\lambda}_{\alpha,1}-\tilde{\lambda}_{\alpha-1,n}}\left(e^{-\tilde{\lambda}_{\alpha-1,n}t} - e^{-\tilde{\lambda}_{\alpha,1}t}\right)\right]\end{aligned} \tag{C.9}$$

This form can be converted into a linear parent form with the assumption that the neutron capture parent $N_{\alpha-1,j}$ is rapidly decaying. This assumption is valid for all parent nuclei sufficiently far from the line of stability, see Fig. 4.1. If $N_{\alpha-1,j}$ is rapidly decaying then $\lambda_{\alpha-1,j} \gg \phi_t \sigma_{\alpha-1,j}$ and few $N_{\alpha-1,j}(n,\gamma)N_{\alpha,1}$ captures will occur, resulting in $\sigma_{\alpha-1,j} \ll \lambda_{\alpha,i}$. This same linear claim can be made for the chain parent $N_{\alpha,i}$ such that $\lambda_{\alpha,1} \gg \phi_t \sigma_{\alpha,1}$ leading to $\tilde{\lambda}_{\alpha,1} \rightarrow \lambda_{\alpha,1}$. Therefore, the simplification of a linear parent can be given by:

$$N_{\alpha,1}(t) = \left[N_{\alpha,1_0}\right] e^{-\lambda_{\alpha,1}t} + \left[\frac{\vec{Z}_{\alpha,1} \cdot \vec{\mathcal{F}}}{\lambda_{\alpha,1}}\right]\left(1 - e^{-\lambda_{\alpha,1}t}\right) \tag{C.10}$$

Next, the solution for an arbitrary daughter $N_{\alpha,i}$ in the beta-decay chain is presented. Here, the assumption that $\lambda_{\alpha,i-1}N_{\alpha,i-1} = 0$ cannot be made. Thus, a form for the beta-chain parent must be supplied as well.

$$N_{\alpha,i-1} = \sum_{n=1}^{i-1} C_{\alpha,n} e^{-\tilde{\lambda}_{\alpha,n}t} + D_{\alpha,i-1} \tag{C.11}$$

Thus, the total differential equation for an arbitrary daughter is given as:

$$\begin{aligned} \frac{dN_{\alpha,i}}{dt} = \vec{Y}_{\alpha,i} \cdot \vec{\mathcal{F}} - \tilde{\lambda}_{\alpha,i}N_{\alpha,i} + \phi_t \sigma_{\alpha-1,j}\left[\sum_{n=1}^{j} A_{\alpha-1,n} e^{-\tilde{\lambda}_{\alpha-1,n}t} + B_{\alpha-1,j}\right] \\ + \lambda_{\alpha,i-1}\left[\sum_{n=1}^{i-1} C_{\alpha,n} e^{-\tilde{\lambda}_{\alpha,n}t} + D_{\alpha,i-1}\right] \end{aligned} \tag{C.12}$$

The method of undetermined coefficients is used again, but this time the particular solution $N'_{\alpha,i}(t)$ will need to have three undetermined coefficients to match the exponentials present in Eq. C.12. The reason for three coefficients, and not four, is because the two constant terms can be combined into a single one $E'_{\alpha,i}$ and, therefore, $N'_{\alpha,i}(t)$ has the form

$$N'_{\alpha,i}(t) = \sum_{n=1}^{j} A'_{\alpha,n} e^{-\tilde{\lambda}_{\alpha-1,n}t} + \sum_{n=1}^{i-1} C'_{\alpha,n} e^{-\tilde{\lambda}_{\alpha,n}t} + E'_{\alpha,i} \tag{C.13}$$

As the solution mechanism is exactly identical to that of the parent form, the assignments for the different coefficients is provided now instead of walking through the algebra.

$$\begin{aligned} A'_{\alpha,n} &= \left(\frac{\phi_t \sigma_{\alpha-1,j}}{\tilde{\lambda}_{\alpha,i} - \tilde{\lambda}_{\alpha-1,n}}\right) A_{\alpha-1,n} \qquad E'_{\alpha,i} = \left(\frac{\phi_t \sigma_{\alpha-1,j} B_{\alpha-1,j} + \vec{Y}_{\alpha,i} \cdot \vec{\mathcal{F}} + \lambda_{\alpha,i-1} D_{\alpha,i-1}}{\tilde{\lambda}_{\alpha,i}}\right) \\ C'_{\alpha,n} &= \left(\frac{\lambda_{\alpha,i-1}}{\tilde{\lambda}_{\alpha,i} - \tilde{\lambda}_{\alpha,n}}\right) C_{\alpha,n} \end{aligned} \tag{C.14}$$

With these assignments inserted into Eq. C.11 and the expression for the homogeneous solution $\tilde{N}_{\alpha,i}(t) = \tilde{C}e^{-\tilde{\lambda}_{\alpha,i}t}$ the total solution can be determined. Again, the last step is to select a value for the initial condition $N_{\alpha,i}(t=0) = N_{\alpha,i_0}$, which provides the initial solution found as Eq. 4.10, rewritten here

$$\begin{aligned} N_{\alpha,i}(t) =& \left[N_{\alpha,i_0}\right] e^{-\tilde{\lambda}_{\alpha,i}t} + \left[\frac{\phi_t\sigma_{\alpha-1,j}B_{\alpha-1,j} + \lambda_{\alpha,i-1}D_{\alpha,i-1} + \vec{Y}_{\alpha,i}\cdot\vec{\mathcal{F}}}{\tilde{\lambda}_{\alpha,i}}\right]\left(1 - e^{-\tilde{\lambda}_{\alpha,i}t}\right) \\ &+ \left[\sum_{n=1}^{j}\frac{\phi_t\sigma_{\alpha-1,j}A_{\alpha-1,n}}{\tilde{\lambda}_{\alpha,i} - \tilde{\lambda}_{\alpha-1,n}}\left(e^{-\tilde{\lambda}_{\alpha-1,n}t} - e^{-\tilde{\lambda}_{\alpha,i}t}\right)\right] + \left[\sum_{n=1}^{i-1}\frac{\lambda_{\alpha,i-1}C_{\alpha,n}}{\tilde{\lambda}_{\alpha,i} - \tilde{\lambda}_{\alpha,n}}\left(e^{-\tilde{\lambda}_{\alpha,n}t} - e^{-\tilde{\lambda}_{\alpha,i}t}\right)\right] \end{aligned} \tag{C.15}$$

Finally, the last form to derive is the stable daughter $N_{\alpha,N}$. This can be solved for trivially by simply asserting that this nuclide is given by the $N_{\alpha,i}$ solution with $i = N$, except we restrict $N_{\alpha,N}$ from decaying, that is $\tilde{\lambda}_{\alpha,N} = \phi_t\sigma_{\alpha,N}$. As this is a simple substitution, the result is just stated and not derived.

$$\begin{aligned} N_{\alpha,N}(t) =& \left[N_{\alpha,N_0}\right] e^{-\phi_t\sigma_{\alpha,N}t} + \left[\frac{\phi_t\sigma_{\alpha-1,j}B_{\alpha-1,j} + \lambda_{\alpha,N-1}D_{\alpha,N-1} + \vec{Y}_{\alpha,i}\cdot\vec{\mathcal{F}}}{\phi_t\sigma_{\alpha,N}}\right]\left(1 - e^{-\phi_t\sigma_{\alpha,N}t}\right) \\ &+ \left[\sum_{n=1}^{j}\frac{\phi_t\sigma_{\alpha-1,j}A_{\alpha-1,n}}{\phi_t\sigma_{\alpha,N} - \tilde{\lambda}_{\alpha-1,n}}\left(e^{-\tilde{\lambda}_{\alpha-1,n}t} - e^{-\phi_t\sigma_{\alpha,N}t}\right)\right] + \left[\sum_{n=1}^{N-1}\frac{\lambda_{\alpha,N-1}C_{\alpha,n}}{\phi_t\sigma_{\alpha,N} - \tilde{\lambda}_{\alpha,n}}\left(e^{-\tilde{\lambda}_{\alpha,n}t} - e^{-\phi_t\sigma_{\alpha,N}t}\right)\right] \end{aligned} \tag{C.16}$$

The solutions found for the particular 3-nuclide chain described by Eq. 4.11 are simply specific solutions to the general solutions derived here. For example, Eq. C.9, with the simplifications of $\sigma_{\alpha,1} = 0$ and by replacing the identifier $(\alpha, 1) \to L$ results in the long-lived precursor parent solution $N_L(t)$ given as Eq. 4.12. Similar simplifications are used to derive the solutions for $N_P(t)$ and $N_N(t)$.

Bibliography

[1] Patrick Huber and Patrick Jaffke. Neutron capture and the antineutrino yield from nuclear reactors. 2015. (Cited on pages ii, 58, 73, and 118.)

[2] F.P. An et al. Observation of electron-antineutrino disappearance at Daya Bay. *Phys.Rev.Lett.*, 108:171803, 2012. (Cited on pages ii, 4, 34, and 71.)

[3] Eric Christensen, Patrick Huber, and Patrick Jaffke. Antineutrino reactor safeguards - a case study. 2013. (Cited on pages ii, 5, 71, 76, 77, 88, 89, 90, 91, 93, and 95.)

[4] Patrick Jaffke Eric Christensen, Patrick Huber. Antineutrino reactor safeguards: A case study of the dprk 1994 nuclear crisis. *Science & Global Security*, 23(1):20–47, 2015. (Cited on pages ii, 81, 86, and 94.)

[5] Eric Christensen, Patrick Huber, Patrick Jaffke, and Thomas E. Shea. Antineutrino Monitoring for Heavy Water Reactors. *Phys. Rev. Lett.*, 113(4):042503, 2014. (Cited on pages ii, 5, 71, 76, 77, 101, 102, and 104.)

[6] Wolfgang Pauli. W. pauli letter of the 4th of december 1930. Pauli Archive at CERN. (Cited on page 1.)

[7] E. Fermi. Trends to a Theory of beta Radiation. (In Italian). *Nuovo Cim.*, 11:1–19, 1934. (Cited on pages 1, 5, 15, 17, and 19.)

[8] J. Chadwick. The intensity distribution in the magnetic spectrum of beta particles from radium (B + C). *Verh.Phys.Gesell.*, 16:383–391, 1914. (Cited on pages 1 and 2.)

[9] H. Bethe and R. Peierls. The neutrino. *Nature*, 133:532, 1934. (Cited on page 1.)

[10] Jr. Davis, Raymond, Don S. Harmer, and Kenneth C. Hoffman. Search for neutrinos from the sun. *Phys.Rev.Lett.*, 20:1205–1209, 1968. (Cited on pages 2 and 29.)

[11] John N. Bahcall. Solar Neutrino Experiments. *Rev. Mod. Phys.*, 50:881, 1978. (Cited on page 2.)

[12] C.L. Cowan, F. Reines, F.B. Harrison, H.W. Kruse, and A.D. McGuire. Detection of the free neutrino: A Confirmation. *Science*, 124:103–104, 1956. (Cited on pages 2 and 28.)

[13] T.D. Lee, R. Oehme, and Chen-Ning Yang. Remarks on Possible Noninvariance Under Time Reversal and Charge Conjugation. *Phys.Rev.*, 106:340–345, 1957. (Cited on page 2.)

[14] T.T. Wu and Chen-Ning Yang. Phenomenological Analysis of Violation of CP Invariance in Decay of K0 and anti-K0. *Phys.Rev.Lett.*, 13:380–385, 1964. (Cited on page 2.)

[15] R.P. Feynman and Murray Gell-Mann. Theory of Fermi interaction. *Phys.Rev.*, 109:193–198, 1958. (Cited on page 2.)

[16] J.J. Sakurai. MASS REVERSAL AND WEAK INTERACTIONS. *Nuovo Cim.*, 7:649–660, 1958. (Cited on page 2.)

[17] E.C.G. Sudarshan and R.e. Marshak. Chirality invariance and the universal Fermi interaction. *Phys.Rev.*, 109:1860–1860, 1958. (Cited on page 2.)

[18] M. Goldhaber, L. Grodzins, and A. W. Sunyar. Helicity of Neutrinos. *Phys. Rev.*, 109:1015–1017, 1958. (Cited on page 2.)

[19] M. Agostini et al. Results on Neutrinoless Double-β Decay of ^{76}Ge from Phase I of the GERDA Experiment. *Phys.Rev.Lett.*, 111(12):122503, 2013. (Cited on pages 2 and 16.)

[20] J.B. Albert et al. Search for Majorana neutrinos with the first two years of EXO-200 data. *Nature*, 510:229–234, 2014. (Cited on page 2.)

[21] Ettore Majorana. Theory of the Symmetry of Electrons and Positrons. *Nuovo Cim.*, 14:171–184, 1937. (Cited on page 2.)

[22] H. Weyl. Electron and Gravitation. 1. (In German). *Z.Phys.*, 56:330–352, 1929. (Cited on page 2.)

[23] Chen-Ning Yang and Robert L. Mills. Conservation of Isotopic Spin and Isotopic Gauge Invariance. *Phys.Rev.*, 96:191–195, 1954. (Cited on page 2.)

[24] Y. Dothan, Murray Gell-Mann, and Yuval Ne'eman. Series of Hadron Energy Levels as Representations of Noncompact Groups. *Phys.Lett.*, 17:148–151, 1965. (Cited on page 2.)

[25] S.L. Glashow. Partial Symmetries of Weak Interactions. *Nucl.Phys.*, 22:579–588, 1961. (Cited on page 2.)

[26] Steven Weinberg. A Model of Leptons. *Phys.Rev.Lett.*, 19:1264–1266, 1967. (Cited on page 2.)

[27] Abdus Salam and John Clive Ward. Weak and electromagnetic interactions. *Nuovo Cim.*, 11:568–577, 1959. (Cited on page 2.)

[28] F.J. Hasert et al. Observation of Neutrino Like Interactions Without Muon Or Electron in the Gargamelle Neutrino Experiment. *Phys.Lett.*, B46:138–140, 1973. (Cited on page 2.)

[29] B. Pontecorvo. Electron and Muon Neutrinos. *Sov.Phys.JETP*, 10:1236–1240, 1960. (Cited on page 2.)

[30] B. Pontecorvo. Inverse beta processes and nonconservation of lepton charge. *Sov. Phys. JETP*, 7:172–173, 1958. [Zh. Eksp. Teor. Fiz.34,247(1957)]. (Cited on pages 2 and 8.)

[31] G. Danby, J.M. Gaillard, Konstantin A. Goulianos, L.M. Lederman, Nari B. Mistry, et al. Observation of High-Energy Neutrino Reactions and the Existence of Two Kinds of Neutrinos. *Phys.Rev.Lett.*, 9:36–44, 1962. (Cited on page 2.)

[32] Ziro Maki, Masami Nakagawa, and Shoichi Sakata. Remarks on the unified model of elementary particles. *Prog.Theor.Phys.*, 28:870–880, 1962. (Cited on pages 2 and 9.)

[33] K. Hirata et al. Observation of a Neutrino Burst from the Supernova SN 1987a. *Phys.Rev.Lett.*, 58:1490–1493, 1987. (Cited on page 3.)

[34] R.M. Bionta, G. Blewitt, C.B. Bratton, D. Casper, A. Ciocio, et al. Observation of a Neutrino Burst in Coincidence with Supernova SN 1987a in the Large Magellanic Cloud. *Phys.Rev.Lett.*, 58:1494, 1987. (Cited on page 3.)

[35] E. N. Alekseev, L. N. Alekseeva, V. I. Volchenko, and I. V. Krivosheina. Possible Detection of a Neutrino Signal on 23 February 1987 at the Baksan Underground Scintillation Telescope of the Institute of Nuclear Research. *JETP Lett.*, 45:589–592, 1987. [Pisma Zh. Eksp. Teor. Fiz.45,461(1987)]. (Cited on page 3.)

[36] Georg G. Raffelt. Particle physics from stars. *Ann.Rev.Nucl.Part.Sci.*, 49:163–216, 1999. (Cited on pages 3 and 4.)

[37] Y. Fukuda et al. Evidence for oscillation of atmospheric neutrinos. *Phys.Rev.Lett.*, 81:1562–1567, 1998. (Cited on pages 3 and 29.)

[38] Q.R. Ahmad et al. Direct evidence for neutrino flavor transformation from neutral current interactions in the Sudbury Neutrino Observatory. *Phys.Rev.Lett.*, 89:011301, 2002. (Cited on page 3.)

[39] K. Eguchi et al. First results from KamLAND: Evidence for reactor anti-neutrino disappearance. *Phys.Rev.Lett.*, 90:021802, 2003. (Cited on page 3.)

[40] M.H. Ahn et al. Indications of neutrino oscillation in a 250 km long baseline experiment. *Phys.Rev.Lett.*, 90:041801, 2003. (Cited on page 3.)

[41] D. G. Michael et al. Observation of muon neutrino disappearance with the MINOS detectors and the NuMI neutrino beam. *Phys. Rev. Lett.*, 97:191801, 2006. (Cited on page 3.)

[42] Dzh.N. Abdurashitov et al. Results from SAGE. *Phys. Lett.*, B328:234–248, 1994. (Cited on pages 4 and 29.)

[43] W. Hampel et al. GALLEX solar neutrino observations: Results for GALLEX IV. *Phys. Lett.*, B447:127–133, 1999. (Cited on page 4.)

[44] S. P. Mikheev and A. Yu. Smirnov. Resonant amplification of neutrino oscillations in matter and solar neutrino spectroscopy. *Nuovo Cim.*, C9:17–26, 1986. (Cited on pages 4, 12, and 13.)

[45] L. Wolfenstein. Neutrino Oscillations in Matter. *Phys. Rev.*, D17:2369–2374, 1978. (Cited on pages 4 and 12.)

[46] K. Abe et al. Indication of Electron Neutrino Appearance from an Accelerator-produced Off-axis Muon Neutrino Beam. *Phys. Rev. Lett.*, 107:041801, 2011. (Cited on page 4.)

[47] M. Apollonio et al. Initial results from the CHOOZ long baseline reactor neutrino oscillation experiment. *Phys. Lett.*, B420:397–404, 1998. (Cited on pages 4 and 32.)

[48] J.K. Ahn et al. Observation of Reactor Electron Antineutrino Disappearance in the RENO Experiment. *Phys.Rev.Lett.*, 108:191802, 2012. (Cited on pages 4, 14, and 56.)

[49] Y. Abe et al. Indication for the disappearance of reactor electron antineutrinos in the Double Chooz experiment. *Phys.Rev.Lett.*, 108:131801, 2012. (Cited on pages 4 and 56.)

[50] C. Arpesella et al. Direct Measurement of the Be-7 Solar Neutrino Flux with 192 Days of Borexino Data. *Phys. Rev. Lett.*, 101:091302, 2008. (Cited on page 4.)

[51] A. Gando et al. Reactor On-Off Antineutrino Measurement with KamLAND. *Phys. Rev.*, D88(3):033001, 2013. (Cited on pages 4 and 14.)

[52] K. Abe et al. Precise Measurement of the Neutrino Mixing Parameter θ_{23} from Muon Neutrino Disappearance in an Off-Axis Beam. *Phys. Rev. Lett.*, 112(18):181801, 2014. (Cited on pages 4 and 14.)

[53] F. P. An et al. Spectral measurement of electron antineutrino oscillation amplitude and frequency at Daya Bay. *Phys. Rev. Lett.*, 112:061801, 2014. (Cited on pages 4, 14, and 30.)

[54] K. A. Olive et al. Review of Particle Physics. *Chin. Phys.*, C38:090001, 2014. (Cited on page 4.)

[55] F. Capozzi, G. L. Fogli, E. Lisi, A. Marrone, D. Montanino, and A. Palazzo. Status of three-neutrino oscillation parameters, circa 2013. *Phys. Rev.*, D89:093018, 2014. (Cited on pages 5 and 14.)

[56] M.G. Aartsen et al. First observation of PeV energy neutrinos with IceCube. *Phys.Rev.Lett.*, 111:021103, 2013. (Cited on page 5.)

[57] M. G. Aartsen et al. Observation of High-Energy Astrophysical Neutrinos in Three Years of IceCube Data. *Phys. Rev. Lett.*, 113:101101, 2014. (Cited on page 5.)

[58] D. S. Ayres et al. NOvA: Proposal to build a 30 kiloton off-axis detector to study nu(mu) —¿ nu(e) oscillations in the NuMI beamline. 2004. (Cited on page 5.)

[59] Miao He. Jiangmen Underground Neutrino Observatory. 2014. (Cited on page 5.)

[60] C. Adams et al. The Long-Baseline Neutrino Experiment: Exploring Fundamental Symmetries of the Universe. 2013. (Cited on page 5.)

[61] J. Alonso et al. Expression of Interest for a Novel Search for CP Violation in the Neutrino Sector: DAEdALUS. 2010. (Cited on page 5.)

[62] A. Donini, M. B. Gavela, P. Hernandez, and S. Rigolin. Neutrino mixing and CP violation. *Nucl. Phys.*, B574:23–42, 2000. (Cited on page 5.)

[63] Steven R. Elliott and Petr Vogel. Double beta decay. *Ann. Rev. Nucl. Part. Sci.*, 52:115–151, 2002. (Cited on page 5.)

[64] Frank T. Avignone, III, Steven R. Elliott, and Jonathan Engel. Double Beta Decay, Majorana Neutrinos, and Neutrino Mass. *Rev. Mod. Phys.*, 80:481–516, 2008. (Cited on page 5.)

[65] S. M. Bilenky, C. Giunti, J. A. Grifols, and E. Masso. Absolute values of neutrino masses: Status and prospects. *Phys. Rept.*, 379:69–148, 2003. (Cited on page 5.)

[66] A.A. Borovoi and L.A. Mikaélyan. Possibilities of the practical use of neutrinos. *Soviet Atomic Energy*, 44(6):589–592, 1978. (Cited on pages 5, 18, and 76.)

[67] V.A. Korovkin, S.A. Kodanev, A.D. Yarichin, A.A. Borovoi, V.I. Kopeikin, L.A. Mikaélyan, and V.D. Sidorenko. Measurement of burnup of nuclear fuel in a reactor by neutrino emission. *Soviet Atomic Energy*, 56(4):233–239, 1984. (Cited on pages 5 and 22.)

[68] V.A. Korovkin, S.A. Kodanev, N.S. Panashchenko, D.A. Sokolov, O.M. Solov'yanov, N.D. Tverdovskii, A.D. Yarichin, S.N. Ketov, V.I. Kopeikin, I.N. Machulin, L.A. Mikaélyan, and V.V. Sinev. Measuring nuclear plant power output by neutrino detection. *Soviet Atomic Energy*, 65(3):712–718, 1988. (Cited on pages 5, 22, and 77.)

[69] N. S. Bowden et al. Experimental results from an antineutrino detector for cooperative monitoring of nuclear reactors. *Nucl. Instrum. Meth.*, A572:985–998, 2007. (Cited on page 5.)

[70] A. Bernstein, N. S. Bowden, A. Misner, and T. Palmer. Monitoring the Thermal Power of Nuclear Reactors with a Prototype Cubic Meter Antineutrino Detector. *J. Appl. Phys.*, 103:074905, 2008. (Cited on pages 5 and 77.)

[71] J. Ashenfelter et al. PROSPECT - A Precision Reactor Oscillation and Spectrum Experiment at Short Baselines. In *Community Summer Study 2013: Snowmass on the Mississippi (CSS2013) Minneapolis, MN, USA, July 29-August 6, 2013*, 2013. (Cited on pages 5, 32, 36, 75, 98, and 106.)

[72] M. Askins et al. The Physics and Nuclear Nonproliferation Goals of WATCHMAN: A WAter CHerenkov Monitor for ANtineutrinos. 2015. (Cited on pages 5 and 105.)

[73] C. Lane et al. A new type of Neutrino Detector for Sterile Neutrino Search at Nuclear Reactors and Nuclear Nonproliferation Applications. 2015. (Cited on pages 5, 36, 98, and 106.)

[74] Fabio Mantovani, Luigi Carmignani, Gianni Fiorentini, and Marcello Lissia. Antineutrinos from the earth: The Reference model and its uncertainties. *Phys. Rev.*, D69:013001, 2004. (Cited on page 5.)

[75] Pietro Antonioli et al. SNEWS: The Supernova Early Warning System. *New J. Phys.*, 6:114, 2004. (Cited on page 5.)

[76] Patrick Huber. Submarine neutrino communication. *Phys. Lett.*, B692:268–271, 2010. (Cited on page 5.)

[77] A. Aguilar-Arevalo et al. Evidence for neutrino oscillations from the observation of anti-neutrino(electron) appearance in a anti-neutrino(muon) beam. *Phys. Rev.*, D64:112007, 2001. (Cited on page 6.)

[78] A. A. Aguilar-Arevalo et al. Event Excess in the MiniBooNE Search for $\bar{\nu}\_\mu \to \bar{\nu}\_e$ Oscillations. *Phys. Rev. Lett.*, 105:181801, 2010. (Cited on page 6.)

[79] D. Decamp et al. A Precise Determination of the Number of Families With Light Neutrinos and of the Z Boson Partial Widths. *Phys. Lett.*, B235:399, 1990. (Cited on page 6.)

[80] Fred E. Wietfeldt and Geoffrey L. Greene. *Colloquium* : The neutron lifetime. *Rev. Mod. Phys.*, 83:1173–1192, Nov 2011. (Cited on page 6.)

[81] G. Mention, M. Fechner, Th. Lasserre, Th. A. Mueller, D. Lhuillier, M. Cribier, and A. Letourneau. The Reactor Antineutrino Anomaly. *Phys. Rev.*, D83:073006, 2011. (Cited on pages 6, 36, 55, and 74.)

[82] Patrick Huber. Erratum: Determination of antineutrino spectra from nuclear reactors [phys. rev. c **84** , 024617 (2011)]. *Phys. Rev. C*, 85:029901, Feb 2012. (Cited on page 6.)

[83] Th. A. Mueller et al. Improved Predictions of Reactor Antineutrino Spectra. *Phys. Rev.*, C83:054615, 2011. (Cited on pages 6, 18, 21, 22, 46, 55, 56, 57, 63, 73, 74, 75, 77, 78, 112, and 116.)

[84] Dzh.N. Abdurashitov et al. The Russian-American gallium experiment (SAGE) Cr neutrino source measurement. *Phys. Rev. Lett.*, 77:4708–4711, 1996. (Cited on page 6.)

[85] P. Anselmann et al. First results from the Cr-51 neutrino source experiment with the GALLEX detector. *Phys. Lett.*, B342:440–450, 1995. (Cited on page 6.)

[86] Carlo Giunti and Marco Laveder. Statistical Significance of the Gallium Anomaly. *Phys. Rev.*, C83:065504, 2011. (Cited on page 6.)

[87] B. Pontecorvo. Neutrino Experiments and the Problem of Conservation of Leptonic Charge. *Sov. Phys. JETP*, 26:984–988, 1968. [Zh. Eksp. Teor. Fiz.53,1717(1967)]. (Cited on page 9.)

[88] Dan-Di Wu and Zhi-Zhong Xing. On the unitarity triangles of the CKM matrix. *Phys. Lett.*, B341:386–390, 1995. (Cited on page 9.)

[89] C. Giunti. Energy and momentum of oscillating neutrinos. *Mod. Phys. Lett.*, A16:2363, 2001. (Cited on page 10.)

[90] Mikael Beuthe. Oscillations of neutrinos and mesons in quantum field theory. *Phys. Rept.*, 375:105–218, 2003. (Cited on page 10.)

[91] Maxim Dvornikov. Field theory description of neutrino oscillations. In *Neutrinos: Properties, Sources and Detection, ed. by J.P.Greene. (Nova Science Publishers, New York, 2011, p. 23-90*, pages 23–90, 2010. (Cited on page 10.)

[92] Boris Kayser. On the Quantum Mechanics of Neutrino Oscillation. *Phys. Rev.*, D24:110, 1981. (Cited on page 10.)

[93] C. Giunti. Neutrino wave packets in quantum field theory. *JHEP*, 11:017, 2002. (Cited on page 10.)

[94] Masataka Fukugita and Tsutomu Yanagida. *Physics of Neutrinos and Applications to Astrophysics*. Springer, 2003. (Cited on page 10.)

[95] M. Blasone and Giuseppe Vitiello. Quantum field theory of fermion mixing. *Annals Phys.*, 244:283–311, 1995. [Erratum: Annals Phys.249,363(1996)]. (Cited on page 10.)

[96] Stuart Samuel. Neutrino oscillations in dense neutrino gases. *Phys. Rev. D*, 48:1462–1477, Aug 1993. (Cited on page 12.)

[97] L. Wolfenstein. Neutrino Oscillations and Stellar Collapse. *Phys. Rev.*, D20:2634–2635, 1979. (Cited on page 13.)

[98] Boris Kayser. Neutrino Oscillation Phenomenology. In *Neutrinos in particle physics, astrophysics and cosmology. Proceedings, 61st Scottish Universities Summer School in Physics, SUSSP61, St. Andrews, UK, August 8-23, 2006*, pages 51–64, 2008. (Cited on page 13.)

[99] Jun Hidaka and George M. Fuller. Dark matter sterile neutrinos in stellar collapse: Alteration of energy/lepton number transport and a mechanism for supernova explosion enhancement. *Phys. Rev.*, D74:125015, 2006. (Cited on page 13.)

[100] H. A. Bethe. A Possible Explanation of the Solar Neutrino Puzzle. *Phys. Rev. Lett.*, 56:1305, 1986. (Cited on page 13.)

[101] S. Schael et al. Precision electroweak measurements on the Z resonance. *Phys. Rept.*, 427:257–454, 2006. (Cited on pages 14 and 16.)

[102] P. A. R. Ade et al. Planck 2013 results. XVI. Cosmological parameters. *Astron. Astrophys.*, 571:A16, 2014. (Cited on pages 14 and 16.)

[103] N. Agafonova et al. Observation of a first ν_τ candidate in the OPERA experiment in the CNGS beam. *Phys. Lett.*, B691:138–145, 2010. (Cited on page 14.)

[104] Samoil M. Bilenky, J. Hosek, and S. T. Petcov. On Oscillations of Neutrinos with Dirac and Majorana Masses. *Phys. Lett.*, B94:495, 1980. (Cited on page 14.)

[105] Y. Abe et al. Reactor electron antineutrino disappearance in the Double Chooz experiment. *Phys. Rev.*, D86:052008, 2012. (Cited on page 14.)

[106] E. W. Otten and C. Weinheimer. Neutrino mass limit from tritium beta decay. *Rept. Prog. Phys.*, 71:086201, 2008. (Cited on page 15.)

[107] Ch. Kraus et al. Final results from phase II of the Mainz neutrino mass search in tritium beta decay. *Eur. Phys. J.*, C40:447–468, 2005. (Cited on page 15.)

[108] V. N. Aseev et al. An upper limit on electron antineutrino mass from Troitsk experiment. *Phys. Rev.*, D84:112003, 2011. (Cited on page 15.)

[109] G. Hinshaw et al. Nine-Year Wilkinson Microwave Anisotropy Probe (WMAP) Observations: Cosmological Parameter Results. *Astrophys. J. Suppl.*, 208:19, 2013. (Cited on page 15.)

[110] G. Pagliaroli, F. Rossi-Torres, and F. Vissani. Neutrino mass bound in the standard scenario for supernova electronic antineutrino emission. *Astropart. Phys.*, 33:287–291, 2010. (Cited on page 15.)

[111] Nicola Cabibbo. Unitary symmetry and leptonic decays. *Phys. Rev. Lett.*, 10:531–533, Jun 1963. (Cited on page 15.)

[112] Makoto Kobayashi and Toshihide Maskawa. CP Violation in the Renormalizable Theory of Weak Interaction. *Prog. Theor. Phys.*, 49:652–657, 1973. (Cited on page 15.)

[113] C. Jarlskog. Commutator of the Quark Mass Matrices in the Standard Electroweak Model and a Measure of Maximal CP Violation. *Phys. Rev. Lett.*, 55:1039, 1985. (Cited on page 16.)

[114] Tommy Ohlsson, He Zhang, and Shun Zhou. Probing the leptonic Dirac CP-violating phase in neutrino oscillation experiments. *Phys. Rev.*, D87(5):053006, 2013. (Cited on page 16.)

[115] Boris Kayser. CPT, CP, and c Phases and their Effects in Majorana Particle Processes. *Phys. Rev.*, D30:1023, 1984. (Cited on page 16.)

[116] M. Auger et al. Search for Neutrinoless Double-Beta Decay in ^{136}Xe with EXO-200. *Phys. Rev. Lett.*, 109:032505, 2012. (Cited on page 16.)

[117] A. Gando et al. Limit on Neutrinoless $\beta\beta$ Decay of ^{136}Xe from the First Phase of KamLAND-Zen and Comparison with the Positive Claim in ^{76}Ge. *Phys. Rev. Lett.*, 110(6):062502, 2013. (Cited on page 16.)

[118] H. V. Klapdor-Kleingrothaus, A. Dietz, H. L. Harney, and I. V. Krivosheina. Evidence for neutrinoless double beta decay. *Mod. Phys. Lett.*, A16:2409–2420, 2001. (Cited on page 16.)

[119] Gianpiero Mangano and Pasquale D. Serpico. A robust upper limit on $N_{\rm eff}$ from BBN, circa 2011. *Phys. Lett.*, B701:296–299, 2011. (Cited on page 16.)

[120] Joachim Kopp, Pedro A. N. Machado, Michele Maltoni, and Thomas Schwetz. Sterile Neutrino Oscillations: The Global Picture. *JHEP*, 05:050, 2013. (Cited on page 16.)

[121] Carlo Giunti and Marco Laveder. 3+1 and 3+2 Sterile Neutrino Fits. *Phys. Rev.*, D84:073008, 2011. (Cited on page 16.)

[122] V. Kopeikin, L. Mikaelyan, and V. Sinev. Reactor as a source of antineutrinos: Thermal fission energy. *Phys. Atom. Nucl.*, 67:1892–1899, 2004. [Yad. Fiz.67,1916(2004)]. (Cited on pages 17, 47, 49, and 77.)

[123] John R. Lamarsh and Anthony J. Baratta. *Introduction To Nuclear Engineering*. Pearson, 3rd edition, 2012. (Cited on pages 17 and 35.)

[124] Michel Cribier. Reactor monitoring with neutrinos. *Nucl. Phys. Proc. Suppl.*, 221:57–61, 2011. (Cited on page 17.)

[125] A. Koning, R. Forrest, M. Kellett, R. Mills, H. Henriksson, and Y. Rugama. Joint Evaluated Fission and Fusion File, Incident-neutron data. `http://www-nds.iaea.org/exfor/endf00.htm`, 2006. (Cited on pages 17, 18, 28, 46, 60, 61, 65, and 118.)

[126] Ch. Straede, C. Budtz-Jørgensen, and H.-H. Knitter. 235u(n, f) fragment mass-, kinetic energy- and angular distributions for incident neutron energies between thermal and 6 mev. *Nuclear Physics A*, 462(1):85 – 108, 1987. (Cited on page 17.)

[127] T.R. England and B.F. Rider. Evaluation and compilation of fission product yields. LA-UR-94-3106 ENDF-349, 1993. (Cited on pages 17 and 28.)

[128] Patrick Huber. Erratum: Determination of antineutrino spectra from nuclear reactors [phys. rev. c **84** , 024617 (2011)]. *Phys. Rev. C*, 85:029901, Feb 2012. (Cited on pages 18, 20, 21, 28, 37, 41, 46, 55, 63, 65, 70, 71, 72, 73, 74, 77, 78, 80, 112, 113, 114, and 115.)

[129] M. Fallot, S. Cormon, M. Estienne, A. Algora, V. M. Bui, A. Cucoanes, M. Elnimr, L. Giot, D. Jordan, J. Martino, A. Onillon, A. Porta, G. Pronost, A. Remoto, J. L. Taín, F. Yermia, and A.-A. Zakari-Issoufou. New antineutrino energy spectra predictions from the summation of beta decay branches of the fission products. *Phys. Rev. Lett.*, 109:202504, Nov 2012. (Cited on page 18.)

[130] J.C. Hardy, L.C. Carraz, B. Jonson, and P.G. Hansen. The essential decay of pandemonium: A demonstration of errors in complex beta-decay schemes. *Physics Letters B*, 71(2):307 – 310, 1977. (Cited on page 18.)

[131] A. Algora, D. Jordan, J. L. Taín, B. Rubio, J. Agramunt, A. B. Perez-Cerdan, F. Molina, L. Caballero, E. Nácher, A. Krasznahorkay, M. D. Hunyadi, J. Gulyás, A. Vitéz, M. Csatlós, L. Csige, J. Äysto, H. Penttilä, I. D. Moore, T. Eronen, A. Jokinen, A. Nieminen, J. Hakala, P. Karvonen, A. Kankainen, A. Saastamoinen, J. Rissanen, T. Kessler, C. Weber, J. Ronkainen, S. Rahaman, V. Elomaa, S. Rinta-Antila, U. Hager, T. Sonoda, K. Burkard, W. Hüller, L. Batist, W. Gelletly, A. L. Nichols, T. Yoshida, A. A. Sonzogni, and K. Peräjärvi. Reactor decay heat in ^{239}Pu: Solving the γ discrepancy in the 4˘3000-s cooling period. *Phys. Rev. Lett.*, 105:202501, Nov 2010. (Cited on page 18.)

[132] R.C. Greenwood, R.G. Helmer, M.A. Lee, M.H. Putnam, M.A. Oates, D.A. Struttmann, and K.D. Watts. Total absorption gamma-ray spectrometer for measurement of beta-decay intensity distributions for fission product radionuclides. *Nuclear Instruments and Methods in Physics Research Section A: Accelerators, Spectrometers, Detectors and Associated Equipment*, 314(3):514 – 540, 1992. (Cited on page 18.)

[133] K. Schreckenbach, G. Colvin, W. Gelletly, and F. Von Feilitzsch. DETERMINATION OF THE ANTI-NEUTRINO SPECTRUM FROM U-235 THERMAL NEUTRON FISSION PRODUCTS UP TO 9.5-MEV. *Phys.Lett.*, B160:325–330, 1985. (Cited on pages 19, 63, 64, 68, 71, 73, 74, 77, and 113.)

[134] A.A. Hahn, K. Schreckenbach, G. Colvin, B. Krusche, W. Gelletly, et al. Antineutrino Spectra From ^{241}Pu and ^{239}Pu Thermal Neutron Fission Products. *Phys.Lett.*, B218:365–368, 1989. (Cited on pages 19, 63, 64, 68, 71, 73, 74, 77, 114, and 115.)

[135] N. Haag, A. Gütlein, M. Hofmann, L. Oberauer, W. Potzel, et al. Experimental Determination of the Antineutrino Spectrum of the Fission Products of ^{238}U. *Phys.Rev.Lett.*, 112(12):122501, 2014. (Cited on pages 19, 21, 63, 64, 71, 72, 73, 74, 77, 112, and 116.)

[136] K. Schreckenbach, H.R. Faust, F. von Feilitzsch, A.A. Hahn, K. Hawerkamp, and J.L. Vuilleumier. Absolute measurement of the beta spectrum from 235u fission as a basis for reactor antineutrino experiments. *Physics Letters B*, 99(3):251 – 256, 1981. (Cited on pages 19, 20, and 73.)

[137] J. Y. Mei. A note on the calculation of the fermi function in the theory of beta-decay. *Phys. Rev.*, 81:287–288, Jan 1951. (Cited on page 19.)

[138] A. C. Hayes, J. L. Friar, G. T. Garvey, Gerard Jungman, and Guy Jonkmans. Systematic Uncertainties in the Analysis of the Reactor Neutrino Anomaly. *Phys. Rev. Lett.*, 112:202501, 2014. (Cited on page 21.)

[139] D. G. Madland. Total prompt energy release in the neutron-induced fission of U-235, U-238, and Pu-239. *Nucl. Phys.*, A772:113–137, 2006. (Cited on page 21.)

[140] N. S. Bowden. Reactor monitoring using antineutrino detectors. *Nucl. Phys. Proc. Suppl.*, 217:134–136, 2011. (Cited on page 22.)

[141] C. L. Jones. Simulation of the SONGS Reactor Antineutrino Flux Using DRAGON. 2011. (Cited on page 22.)

[142] H. Bateman. The solution of a system of differential equations occurring in the theory of radioactive transformations. *Proc. Cambridge Philos. Soc.*, 15:423, 1910. (Cited on pages 23 and 117.)

[143] Jerzy Cetnar. General solution of bateman equations for nuclear transmutations. *Annals of Nuclear Energy*, 33(7):640 – 645, 2006. (Cited on pages 23 and 25.)

[144] L. Moral and A. F. Pacheco. Algebraic approach to the radioactive decay equations. *American Journal of Physics*, 71(7):684, 2003. (Cited on pages 23, 25, and 28.)

[145] ORNL. Standardized Computation and Licensing Evaluation. `http://scale.ornl.gov/`, 2011. (Cited on pages 24, 34, 36, 38, 58, 70, 74, 81, 89, 105, and 117.)

[146] Jag Tuli. Evaluated Nuclear Structure Data File. `http://www.nndc.bnl.gov/ensdf/`. (Cited on page 28.)

[147] P. Vogel and John F. Beacom. Angular distribution of neutron inverse beta decay, anti-neutrino(e) + p —¿ e+ + n. *Phys.Rev.*, D60:053003, 1999. (Cited on pages 29, 33, 47, and 80.)

[148] P. A. Cerenkov. Visible luminescence of pure fluids induced by gamma rays. *Dokl. Akad. Nauk Ser. Fiz.*, 2:451–454, 1934. (Cited on page 29.)

[149] P. A. Cerenkov. Visible radiation produced by electrons moving in a medium with velocities exceeding that of light. *Phys. Rev.*, 52:378–379, 1937. (Cited on page 29.)

[150] A. Achterberg et al. First Year Performance of The IceCube Neutrino Telescope. *Astropart. Phys.*, 26:155–173, 2006. (Cited on page 29.)

[151] J. Boger et al. The Sudbury neutrino observatory. *Nucl. Instrum. Meth.*, A449:172–207, 2000. (Cited on page 29.)

[152] D. Casper et al. Measurement of atmospheric neutrino composition with IMB-3. *Phys. Rev. Lett.*, 66:2561–2564, 1991. (Cited on page 29.)

[153] P. Anselmann et al. Solar neutrinos observed by GALLEX at Gran Sasso. *Phys. Lett.*, B285:376–389, 1992. (Cited on page 29.)

[154] Jingyi Yu, Zhe Wang, and Shaomin Chen. A Precise Analytic Delayed Coincidence Efficiency and Accidental Coincidence Rate Calculation. *Chin. Phys.*, 39:056102, 2015. (Cited on page 31.)

[155] MB Chadwick, M Herman, P Obložinskỳ, Michael E Dunn, Y Danon, AC Kahler, Donald L Smith, B Pritychenko, Goran Arbanas, R Arcilla, et al. Endf/b-vii. 1 nuclear data for science and technology: cross sections, covariances, fission product yields and decay data. *Nuclear Data Sheets*, 112(12):2887–2996, 2011. (Cited on page 31.)

[156] Shirley Weishi Li and John F. Beacom. Spallation Backgrounds in Super-Kamiokande Are Made in Muon-Induced Showers. *Phys. Rev.*, D91(10):105005, 2015. (Cited on page 31.)

[157] Dongming Mei and A. Hime. Muon-induced background study for underground laboratories. *Phys. Rev.*, D73:053004, 2006. (Cited on page 31.)

[158] F. P. An et al. A side-by-side comparison of Daya Bay antineutrino detectors. *Nucl. Instrum. Meth.*, A685:78–97, 2012. (Cited on pages 32 and 104.)

[159] J. K. Ahn et al. RENO: An Experiment for Neutrino Oscillation Parameter θ_{13} Using Reactor Neutrinos at Yonggwang. 2010. (Cited on page 32.)

[160] F. P. An et al. Independent measurement of the neutrino mixing angle θ_{13} via neutron capture on hydrogen at Daya Bay. *Phys. Rev.*, D90(7):071101, 2014. (Cited on page 32.)

[161] F. P. An et al. Improved Measurement of Electron Antineutrino Disappearance at Daya Bay. *Chin. Phys.*, C37:011001, 2013. (Cited on pages 32, 37, 46, and 50.)

[162] G. Boireau et al. Online Monitoring of the Osiris Reactor with the Nucifer Neutrino Detector. 2015. (Cited on pages 32, 75, 98, and 106.)

[163] H. Furuta et al. A Study of Reactor Neutrino Monitoring at Experimental Fast Reactor JOYO. *Nucl. Instrum. Meth.*, A662:90–100, 2012. (Cited on pages 32, 77, and 98.)

[164] M.L. Roush, M.A. Wilson, and W.F. Hornyak. Pulse shape discrimination. *Nuclear Instruments and Methods*, 31(1):112 – 124, 1964. (Cited on pages 32 and 98.)

[165] Gioacchino Ranucci, Augusto Goretti, and Paolo Lombardi. Pulse-shape discrimination of liquid scintillators. *Nuclear Instruments and Methods in Physics Research Section A: Accelerators, Spectrometers, Detectors and Associated Equipment*, 412(2–3):374 – 386, 1998. (Cited on pages 32 and 98.)

[166] J. Ashenfelter et al. Light Collection and Pulse-Shape Discrimination in Elongated Scintillator Cells for the PROSPECT Reactor Antineutrino Experiment. 2015. (Cited on pages 32 and 98.)

[167] W. H. Lippincott, K. J. Coakley, D. Gastler, A. Hime, E. Kearns, D. N. McKinsey, J. A. Nikkel, and L. C. Stonehill. Scintillation time dependence and pulse shape discrimination in liquid argon. *Phys. Rev.*, C78:035801, 2008. [Erratum: Phys. Rev.C81,039901(2010)]. (Cited on page 32.)

[168] Nicholas Tsoulfanidis. *The Nuclear Fuel Cycle*. American Nuclear Society, 2013. (Cited on page 35.)

[169] B.J. Ade and I.C. Gauld. Decay heat calculations for pwr and bwr assemblies fueled with uranium and plutonium mixed oxide fuel using scale. Technical report, Oak Ridge National Laboratory, 2011. (Cited on page 35.)

[170] F. P. An et al. Search for a Light Sterile Neutrino at Daya Bay. *Phys. Rev. Lett.*, 113:141802, 2014. (Cited on page 36.)

[171] Ivan Girardi, Davide Meloni, Tommy Ohlsson, He Zhang, and Shun Zhou. Constraining Sterile Neutrinos Using Reactor Neutrino Experiments. *JHEP*, 08:057, 2014. (Cited on page 36.)

[172] G. Domogatski, V. Kopeikin, L. Mikaelyan, and V. Sinev. Neutrino geophysics at Baksan I: Possible detection of georeactor anti-neutrinos. *Phys.Atom.Nucl.*, 68:69–72, 2005. (Cited on pages 36, 56, 72, and 75.)

[173] Ondrej Sramek, William F. McDonough, and John G. Learned. Geoneutrinos. *Adv.High Energy Phys.*, 2012:235686, 2012. (Cited on pages 36, 56, 72, and 75.)

[174] Mandula Jiri. Operating experience with nuclear power stations in member states. http://www.iaea.org/NuclearPower/Engineering/Publications/2012.html, 2005-2011. (Cited on pages 37, 39, 40, 55, and 71.)

[175] International atomic energy agency. `https://www.iaea.org`. (Cited on pages 37, 66, 82, and 101.)

[176] International Atomic Energy Agency. , 2015. (Cited on pages 39 and 40.)

[177] M. Pusa and J. Leppanen. Computing the Matrix Exponential in Burnup Calculations. *Nuclear Science and Engineering*, 164:140–150, 2010. (Cited on page 40.)

[178] Bin Zhou, Xi-Chao Ruan, Yang-Bo Nie, Zu-Ying Zhou, Feng-Peng An, et al. A study of antineutrino spectra from spent nuclear fuel at Daya Bay. *Chin.Phys.*, C36:1–5, 2012. (Cited on pages 42 and 44.)

[179] Patrick Huber, M. Lindner, and W. Winter. Simulation of long-baseline neutrino oscillation experiments with GLoBES (General Long Baseline Experiment Simulator). *Comput.Phys.Commun.*, 167:195, 2005. (Cited on page 45.)

[180] P. Huber, Joachim Kopp, M. Lindner, M. Rolinec, and W. Winter. From double chooz to triple chooz: Neutrino physics at the chooz reactor complex. *JHEP*, 05:072, 2006. (Cited on page 45.)

[181] Patrick Huber, Joachim Kopp, Manfred Lindner, Mark Rolinec, and Walter Winter. New features in the simulation of neutrino oscillation experiments with GLoBES 3.0: General Long Baseline Experiment Simulator. *Comput.Phys.Commun.*, 177:432–438, 2007. (Cited on page 45.)

[182] F. P. An et al. New Measurement of Antineutrino Oscillation with the Full Detector Configuration at Daya Bay. *Phys. Rev. Lett.*, 115(11):111802, 2015. (Cited on pages 45, 46, 48, 55, and 56.)

[183] Chao Zhang. Recent Results From The Daya Bay Experiment. 2015. (Cited on pages 45, 46, and 52.)

[184] Xinheng Guo et al. A Precision measurement of the neutrino mixing angle θ_{13} using reactor antineutrinos at Daya-Bay. 2007. (Cited on page 46.)

[185] T.R. England and B.F. Rider. La-ur-94-3106 evaluation and compilation of fission product yields. Technical report, Los Alamos National Laboratory, 1994. (Cited on pages 46 and 65.)

[186] W.B. Wilson, T.R. England, and M.C. Brady. CinderLibrary. `https://rsicc.ornl.gov/codes/ccc/ccc7/ccc-755.html`, 2000. (Cited on pages 60 and 66.)

[187] International Atomic Energy Agency. Research reactor database. `https://nucleus.iaea.org/RRDB/RR/ReactorSearch.aspx`, 2015. (Cited on page 60.)

[188] John F Ahearne. Nuclear power after chernobyl. *Science*, 236(4802):673–679, 1987. (Cited on page 61.)

[189] A. C. Hayes and Gerard Jungman. Determining Reactor Flux from Xenon-136 and Cesium-135 in Spent Fuel. *Nucl. Instrum. Meth.*, A690:68–74, 2012. (Cited on page 61.)

[190] C. O. Muehlhause and S. Oleksa. Antineutrino flux from a reactor. *Phys. Rev.*, 105:1332–1334, Feb 1957. (Cited on page 62.)

[191] R. E. Carter, F. Reines, J. J. Wagner, and M. E. Wyman. Free antineutrino absorption cross section. ii. expected cross section from measurements of fission fragment electron spectrum. *Phys. Rev.*, 113:280–286, Jan 1959. (Cited on page 62.)

[192] P. Vogel, G. K. Schenter, F. M. Mann, and R. E. Schenter. Reactor antineutrino spectra and their application to antineutrino-induced reactions. ii. *Phys. Rev. C*, 24:1543–1553, Oct 1981. (Cited on page 62.)

[193] Department of Energy. *Nuclear Physics and Reactor Theory Module 2: Reactor Theory (Neutron Characteristics)*. National Technical Information Services, 1993. (Cited on page 66.)

[194] Dan Ilas. Development of a scale model for high flux isotope reactor cycle 400. Technical report, Oak Ridge National Laboratory, 2012. (Cited on pages 68 and 71.)

[195] David Albright and Kevin O'Neill, editors. *Solving the North Korean Nuclear Puzzle*. ISIS Press, 2000. (Cited on pages 71, 85, 87, 88, 89, 90, 91, and 96.)

[196] David Albright and Christina Walrond. Update on the Arak reactor. Technical report, Institute for Science and International Security (ISIS), July 2013. (Cited on page 71.)

[197] L.A. Mikaelyan. Investigation of neutrino properties in experiments at nuclear reactors: Present status and prospects. *Phys.Atom.Nucl.*, 65:1173–1187, 2002. (Cited on page 72.)

[198] V.I. Kopeikin. On search for new physics in nonequilibrium reactor anti-neutrino energy spectrum. *Phys.Atom.Nucl.*, 66:472–475, 2003. (Cited on page 72.)

[199] F. Von Feilitzsch, A.A. Hahn, and K. Schreckenbach. EXPERIMENTAL BETA SPECTRA FROM PU-239 AND U-235 THERMAL NEUTRON FISSION PRODUCTS AND THEIR CORRELATED ANTI-NEUTRINOS SPECTRA. *Phys.Lett.*, B118:162–166, 1982. (Cited on page 73.)

[200] F. Yermia. Status of the Solid experiment. 2014. (Cited on page 75.)

[201] Adam Bernstein, Yi-fang Wang, Giorgio Gratta, and Todd West. Nuclear reactor safeguards and monitoring with anti-neutrino detectors. *J. Appl. Phys.*, 91:4672, 2002. (Cited on page 77.)

[202] Michael Martin Nieto, A. C. Hayes, Corinne M. Teeter, William B. Wilson, and William D. Stanbro. Detection of anti-neutrinos for nonproliferation. 2003. (Cited on page 77.)

[203] Patrick Huber and Thomas Schwetz. Precision spectroscopy with reactor anti-neutrinos. *Phys. Rev.*, D70:053011, 2004. (Cited on page 77.)

[204] N. S. Bowden, A. Bernstein, S. Dazeley, R. Svoboda, A. Misner, and T. Palmer. Observation of the Isotopic Evolution of PWR Fuel Using an Antineutrino Detector. *J. Appl. Phys.*, 105:064902, 2009. (Cited on page 77.)

[205] International Atomic Energy Agency, editor. *Treaty on the Non-proliferation of Nuclear Weapons*, number INFCIRC/140, April 1970. (Cited on pages 77 and 85.)

[206] M. Fallot et al. New antineutrino energy spectra predictions from the summation of beta decay branches of the fission products. *Phys. Rev. Lett.*, 109:202504, 2012. (Cited on page 77.)

[207] David Albright. How much plutonium does North Korea have? *Bulletin of the Atomic Scientists*, 50(5):46, 1994. (Cited on page 85.)

[208] Don Oberdorfer. *The two Koreas: a contemporary history*. Basic Books, 2001. (Cited on page 85.)

[209] David Albright, Frans Berkhout, and William Walker. *Plutonium and highly enriched uranium 1996: world inventories, capabilities and policies*. Oxford University Press, 1997. (Cited on pages 87 and 88.)

[210] IAEA. *Directory of Nuclear Reactors*, volume V - Research, Test and Experimental Reactors. Vienna, Austria: International Atomic Energy Agency, July 1964. (Cited on pages 89 and 90.)

[211] Glenn R. Jocher, Daniel A. Bondy, Brian M. Dobbs, Stephen T. Dye, James A. Georges, John G. Learned, Christopher L. Mulliss, and Shawn Usman. Theoretical antineutrino detection, direction and ranging at long distances. *Phys. Rept.*, 527:131–204, 2013. (Cited on page 96.)

[212] Y. Abe et al. Direct Measurement of Backgrounds using Reactor-Off Data in Double Chooz. *Phys. Rev.*, D87(1):011102, 2013. (Cited on page 97.)

[213] J. Beringer et al. Review of Particle Physics (RPP). *Phys.Rev.*, D86:010001, 2012. (Cited on page 97.)

[214] I. Alekseev et al. DANSSino: a pilot version of the DANSS neutrino detector. *Phys. Part. Nucl. Lett.*, 11:473–482, 2014. (Cited on pages 98 and 106.)

[215] Olli Heinonen. Can the nuclear talks with iran be saved? *Foreign Policy*, 1, January 2011. (Cited on page 99.)

[216] Thomas Mo Willig, Cecilia Futsaether, and Halvor Kippe. Converting the iranian heavy water reactor ir-40 to a more proliferation-resistant reactor. *Science and Global Security*, 20:97–116, 2012. (Cited on pages 99, 101, and 103.)

[217] International Atomic Energy Agency. Joint Comprehensive Plan of Action. `http://www.eeas.europa.eu/statements-eeas/docs/iran_agreement/iran_joint-comprehensive-plan-of-action_en.pdf`, July 2015. (Cited on pages 99 and 103.)

[218] John G. Learned, Stephen T. Dye, and Sandip Pakvasa. Hanohano: A Deep ocean anti-neutrino detector for unique neutrino physics and geophysics studies. In *Neutrino telescopes. Proceedings, 12th International Workshop, Venice, Italy, March 6-9, 2007*, pages 235–269, 2007. (Cited on page 105.)

[219] A Porta and the Nucifer collaboration. Reactor neutrino detection for non proliferation with the nucifer experiment. *Journal of Physics: Conference Series*, 203(1):012092, 2010. (Cited on page 106.)

[220] A. P. Serebrov et al. NEUTRINO4 experiment: preparations for search for sterile neutrino at 100 MW Reactor SM-3 at 6-12 Meters. 2012. (Cited on page 106.)

[221] Thierry Lasserre. Light Sterile Neutrinos in Particle Physics: Experimental Status. *Phys. Dark Univ.*, 4:81–85, 2014. (Cited on page 106.)

[222] Cross Section Evaluation Working Group. Evaluated Nuclear Data File/B-VII.1. `https://t2.lanl.gov/nis/data/endf/endfvii.1-n.html`, 2011. (Cited on page 118.)

[223] Oak Ridge National Laboratory. *Scale: A Comprehensive Modeling and Simulation Suite for Nuclear Safety Analysis and Design.* Oak Ridge National Laboratory, 6.1 edition, June 2011. (Cited on page 120.)